

Survival analysis of GRID irradiated A549 cells *in vitro*

Jacob Larsen Lie



Biological and Medical Physics

60 credits

Institute of Physics

Faculty of Mathematics and Natural Sciences

University of Oslo

June 2022

Acknowledgements

I would like to thank all my supervisors. Thank you to PhD student *Delmon Arous*, for generating the segmentation algorithm that enables me to study survival in 2D, and for helping me through the dosimetry experiments. Thank you Prof. *Eirik Malinen* for great academic conversations, your knowledge in field of everything related to medical physics is undisputed. Thank you to Prof. *Nina Edin* for her professional input on radiobiology and especially uncertainty analysis. Thank you to former MSc. student *Bjørg Vårli Håland* for laying the groundwork for the EBT3 dosimetry and the 1D band analysis. Thank you to former MsC. student *Magnus Børsting* for performing every cell experiment.

Thanks to everyone in the Master student office for their help with expressing my thoughts in writing and help in finding and killing “bugs”. Thanks to my family for great support throughout this whole period, and a special thanks to my significant other for always being there and for being my emotional punching bag when I needed to rant about never finishing my goddamn thesis.

Abstract

Spatially Fractionated Radiation Therapy (SFRT), also known as GRID therapy, spatially modulates the radiation field used to eradicate cancer cells. This generates a heterogeneous dose distribution in the treatment volume with high (peak) and low (valley) dose areas, deviating from conformal radiation therapy mostly used today. Departing from a conventional homogeneous tumor dose distribution can reduce toxicity as low dose areas allow healthy tissue close to the tumor to repair. In addition, it may provide high tumor control for selected cases. Traditionally, radiation dose has been used as the only explanatory variable for predicting the biological effect of ionizing radiation *in vitro*. The most commonly used model for such a prediction is the linear quadratic (LQ) survival model, which basically links cell kill to radiation-induced DNA damage. However, the radiation dose as a single predictor will fail to describe the effects following SFRT with highly heterogeneous dose distributions.

This thesis presents a novel 2D approach to cell survival modelling using Poisson regression and introduces new explanatory variables to potentially explain the SFRT effects. Survival data were acquired from T25 cell culture flasks containing A549 lung carcinoma cells irradiated with either an OPEN (conventional) radiation field or through a striped (5 mm slits) or dotted (5 mm diameter holes) GRID pattern. Surviving colonies (SC) were identified using a machine-learning algorithm developed in house. 2D dosimetry was established to provide dose distribution maps of same dimension as the colony maps. Gafchromic™ EBT3 dosimetry films that darken following radiation exposure were used. The films' dose response was established in a known radiation field calibrated with an ionization chamber. New films were cut to match the shape of the T25 cell flask before being irradiated with or without the GRID collimators.

Dose profiles were generated along the long axis of the cell flasks. From these profiles OPEN field and GRID doses were estimated. For a nominal dose of 5 Gy, OPEN field dose was 4.98(4.93,5.03) Gy, while striped and dotted GRID dose in peak/valley were 4.04(3.98,4.16) / 0.86(0.80,0.87) and 3.37(3.28,3.45) / 0.44(0.41,0.45), respectively. The dose distribution of striped GRID irradiated films was evaluated with data from Monte Carlo simulations, showing high correspondence with measurements.

Colony maps curated from scanned and segmented cell flasks were divided into quadrats of equal size and the number of colonies within each quadrat was summed for further analysis with Poisson regression. The mean dose (D) in each quadrat was estimated by the film dosimetry. D and D^2 were first used as explanatory variables. Then we introduced peak area ratio (PAR), defined as the area fraction of cells positioned within the peak regions, and peak distance, defined as the distance between a quadrats' center to the nearest peak as explanatory variables. They were introduced either as the third or fourth variable in the regression pipeline. Using data for OPEN field and the two GRID configurations jointly, the Poisson regression for 2, 3 or 4 explanatory variables yielded the highest significance for $1 \times 1 \text{ mm}^2$ quadrats. Using peak distance as the third variable resulted in the lowest Akaike information criterion (AIC) score. Striped GRID survival in peak areas was observed to be lower than the predicted survival from a Poisson regression model fitted with OPEN field survival data only with D and D^2 , while the survival in valley areas was equal to the predicted survival. This result was confirmed using a previously established 1D survival analysis. However, some potential systematic errors may impact the validity of the results, and it may be difficult to draw decisive conclusions. This thesis has established a methodology for 2D analysis of cells irradiated using SFRT, with reliable 2D dosimetry. The results indicate that inclusion of additional explanatory variables besides dose is reasonable, and that further development is required to better explain the SFRT effects.

Abbreviations and explanations

AIC_c – Corrected Akaike Information Criterion

ANOVA – Analysis of Variances

Apoptosis – A mechanism allowing damaged cells to initiate self-destruction (*Apoptosis / Cytology / Britannica*, 2013).

ATM – A protein activated by DNA damage. Its purpose is to phosphorylate (activate) numerous proteins related to cellular response after exposure to ionizing radiation (Samuel et al., 2002).

ATP – Adenosine triphosphate a molecule, which provides cells with energy for the cell and phosphate groups for protein activation. Through the process of hydrolysis, ATP is converted to ADP (adenosine diphosphate) (*Adenosine Triphosphate / Definition, Structure, Function, & Facts / Britannica*, 2020).

BM – Biomolecule. There are four types of biomolecules: carbohydrates, lipids, nucleic acids and proteins (*Biomolecule / Definition, Structure, Functions, Examples, & Facts / Britannica*, 2020). These are molecules important for normal cell functioning, and damage to them can have harmful consequences.

CDK – Cyclin dependent kinase

Cytokines – A category of signaling molecules that mediate immune responses by enabling cell to cell communication (Mandal Ananya, 2019). The cytokines relevant to this thesis are different variants of IL (interleukin) cytokine, TNF- α and TGF- β . They are all important in regulating cell division (Najafi et al., 2014).

DNA – Deoxyribose nucleic acid

DNA transcription – A process of creating a messenger ribonucleic acid (mRNA), which is used to create specific proteins. A transcription factor binds to the DNA, telling the enzyme RNA-polymerase to read a gene sequence of interest. As each base (Adenine, Cytosine, Thymine and Guanine) in the sequence is read, a complementary nucleotide is attached to form the mRNA strand (*Transcription / Definition, Steps, & Biology / Britannica*, 2019). In the DNA Adenine binds to Thymine, but during transcription, Thymine is replaced with Uracil (Mason et al., 2020, p.48).

EBT – External Beam Therapy

GD – Gradient Descent

GLCM – Grey-level co-occurrence matrix

GLM – Generalized Linear Models

GN – Gaussian-Newton

HR – Homologous recombination

IAEA – International Atomic Energy Agency

IQR – Interquartile Range

KDE – Kernel Density Estimation

LET – Linear energy transfer

LINAC – Linear accelerator is a device that accelerates charged particles using an alternating electric field. They are used in radiation treatment to accelerate electrons into a high atomic-number target, creating high energy (MV) bremsstrahlung (Philip Mayes et al., 2007).

LM – Levenberg-Marquardt algorithm

MC – Monte Carlo

MN – Micronuclei are chromosome fragments not included in either daughter cells following cell division. They are a result of DNA damage, and might lead to immune responses (Harding et al., 2017).

MLC – Multileaf collimators are individual metal (often Tungsten) blocks used to shape a radiation beam coming from an external radiation therapy machine (Galvin et al., 1993).

MLE – Maximum likelihood estimator

NHEJ – Nonhomologous End-Joining

OAR – Organ at Risk

OD – Optical density

P53 – A protein that is bound to another protein called mdm2. When DNA damage occur, it is released from mdm2, and will bind to a gene for transcription of the p21 protein. This protein will in turn inactivate a protein complex responsible for promoting cell division (Alberts et al., 2014, p.1014).

PCA – Principal Component Analysis

Phosphorylation – Is the process of transferring a phosphate group (PO_3) to a molecule. Proteins are activated by phosphorylation, and the addition of a phosphate group might change the proteins in different ways: Extra charge from PO_3 can attract amino acid chains that connect to the existing protein, or the structure of the binding cite can change (Alberts et al., 2014, p.153-154). Both processes regulate the activity level of the protein.

PAR – Peak Area Ratio

PMF – Probability Mass Function

PreRC – Prereplicative complex

Proteins – Chains of amino acids with different shapes, sizes and functions. One main function is catalyzing certain chemical reactions. These proteins are called enzymes and have binding cites where specific molecules fit. The enzymes can both break and form chemical bonds (Mason et al., 2020, p.38).

RNA-primer – Ribonucleic acid primers are short nucleotide sequences generated by RNA-polymerase. They exist as a starting point for DNA-polymerase, because they are only able to continue an existing strand (Mason et al., 2020, p.292). The RNA-polymerase will attach Uracil instead of Thymine (see 1.7.1), and they must be removed and replaced by a different DNA-polymerase (Cooper, 2000b).

ROS – Reactive Oxygen Species is a collective term for highly reactive molecules based on oxygen. It has been shown an increase in ROS after exposure to radiation, and it has been hypothesized that they mediate DNA damage (Narayanan et al., 1997).

RPD – Relative Percentage Difference

SC – Surviving Colonies

SCE – Sister Chromatid Exchange is the process of sister chromatids exchanging genetic material. Increased SCE reflect the activity of homologous recombination (see 1.7.3), which again reflect the degree of DNA double strand breaks occurrences (see 1.7.3).

SDD – Source to Detector Distance, analog to SSD – Source to Skin Distance.

SF – Survival Fraction

SVD – Singular Value Decomposition

Contents

Abbreviations and explanations	VII
1 Introduction.....	1
1. Theory	2
1.1 Ionizing Radiation	2
1.1.1 Photon interaction in matter	3
1.1.2 Charged Particle interaction in matter	7
1.2 Radiation beam generation	11
1.2.1 X-ray tube.....	11
1.2.2 X-ray filtering.....	12
1.3 Dosimetry.....	13
1.3.1 Quantities.....	14
1.4 Cavity Theory	19
1.4.1 Bragg-Gray cavity.....	19
1.4.2 Bragg-Gray-Laurence.....	20
1.5 Dosimetry methods.....	21
1.5.1 Parallel- Plate Ionization Chamber	21
1.5.2 Thimble Ionization Chamber	22
1.5.3 Radiochromic film	24
1.6 Statistics	25
1.6.1 Non-linear curve fit.....	25
1.6.2 Poisson Regression	28
1.6.3 Confidence interval.....	29
1.7 Radiobiology.....	30
1.7.1 DNA basics	30
1.7.2 Cell Cycle and Checkpoint.....	32
1.7.3 DNA damage and repair.....	35
1.7.4 Cell Survival Curves.....	38
1.7.5 LQ-model	39

1.7.6	Radiation Induced Bystander Effect.....	42
1.7.7	Spatially Fractionated Radiation Therapy	43
2	Materials and Methods.....	44
2.1	Dosimetry.....	45
2.1.1	X-ray dosimetry	45
2.1.2	Gafchromic™ film dosimetry	51
2.2	Cell Experiments	64
2.3	Segmentation	66
2.4	Cell Survival Analysis.....	68
2.4.1	Data acquisition and image registration	69
2.4.2	1D survival analysis.....	71
2.4.3	2D survival analysis.....	72
3	Results.....	80
3.1	X-ray dosimetry	80
3.2	Gafchromic™ film dosimetry.....	82
3.3	Cell survival	91
3.3.1	1D survival analysis.....	93
3.3.2	2D analysis	96
4	Discussion.....	105
4.1	X-ray Dosimetry	105
4.2	Gafchromic™ film dosimetry.....	106
4.3	Cell Survival	109
4.4	1D survival analysis	110
4.5	2D survival analysis	112
5	Conclusion	115
6	References.....	117
7	Appendix.....	130
7.1	Compton Scattering.....	130
7.2	Mean free path	133
7.3	Nearest Peak Code.....	135
7.4	Reference conditions of FC65-G ionization chamber.....	136

7.5	X-ray dosimetry	137
7.5.1	Gafchromic™ film fitting	138
7.5.2	Random initialization of the nonlinear regression.....	141
7.6	Cell Segmentation	142
7.7	Cell flask registration	143
7.8	Poisson evaluation.....	145
7.9	4 x 4 mm ² 2D analysis results.....	147
7.10	Average distance.....	149

1 Introduction

Cancer is a state of uncontrolled cell division where cancerous cells proliferate and invade surrounding tissues. This may cause organ failure and subsequent death if left untreated. Around 10 million deaths were cancer related in 2018, worldwide (WHO). This makes cancer the second leading cause of death. As life expectancy increases, the probability of developing cancer during our lifetime increases (*Risk Factors*, 2015). At the same time, numerous methods have been developed and improved for combating the disease, with surgery, chemotherapy, radiotherapy and combinations of these being the most common. This has resulted in a steadily declining cancer death rate since the 1990's (Sandy McDowell, 2019).

Radiotherapy of cancer utilizes ionizing radiation such as high-energy X-rays (photons). In its most basic form, a beam of photons is directed towards the patient at different angles achieving a near homogeneous dose distribution in the tumor (L. Yan et al., 2019). When the tissue is exposed to radiation, the most important radiochemical effects are damages to the cell's DNA. In the case of cancer, this may inactivate ('kill') the cells and prevent them from further invasion of tissue. However, because photons distribute their energy non-selectively in the medium (*Photon Dose Distributions / Oncology Medical Physics*, n.d.), they also deposit radiation dose in healthy tissue positioned in front and behind the tumor. This may cause damages, potentially causing critical side effects such as organ dysfunction. Thus, it is important to consider new radiotherapy strategies to improve patient outcomes.

One alternative radiotherapy strategy is spatially fractionated radiation therapy (SFRT or GRID therapy), which departs from the conventional approach of delivering a homogeneous tumor dose. Irradiating the patient with high doses through a GRID collimator generates low dose areas wherein tissue sparing can occur (Mohiuddin et al., 1999), while the high-dose peaks in the tumor have been shown to retain high tumor control (R. Asur et al., 2015). The radiobiological effects of spatially fractionating the radiation field includes bystander and abscopal effects, referring to local and distant 'radiation-like' effects in unirradiated cells. However, the physical and biological parameters that determine these SFRT effects are yet to be clearly identified (Blyth & Sykes, 2011; Grass et al., 2016).

Cell survival following irradiation *in vitro* is often analyzed using the linear quadratic (LQ) model. This condenses the cellular radiosensitivity into two principal parameters, α and β . However, a prerequisite for this analysis is that all cells within a culture flask receive the same dose. Thus, cell survival from heterogeneous GRID irradiation cannot be analyzed with this conventional modelling approach, and new methods are required. We will therefore propose a novel 2D approach to Cell survival where irradiated cell flasks and the colonies within are not treated as a whole, but rather dividing the cell flask into smaller quadrats with different doses and different survival. The goal is then to predict the survival within individual quadrats and make a model suitable for all methods of irradiation *in vitro*. However, this demands new explanatory variables other than dose (D) and D^2 to explain the SFRT effects. Thus, an area fractionation and a peak distance parameter will be introduced. Gafchromic™ film dosimetry will be performed to generate 2D dose maps for accurate depiction of dose received by the cells.

1. Theory

1.1 Ionizing Radiation

Radiation is transfer of energy to matter through electromagnetic waves. The main categories are ionizing and non-ionizing radiation, where the former has enough energy to liberate an electron from the atom, or it does not. Non-ionizing radiation consists of low-frequency electromagnetic (EM) waves such as UV-light and microwaves. Because energy is $E = h\nu$, with h being the Planck constant and ν being the frequency, the energy increases with frequency and the radiation becomes ionizing for X-ray and γ -rays. Together with neutrons, they make up a group called uncharged radiation. These radiation types are often highly penetrating because they need to interact directly with a target, thus decreasing interaction probability.

Charged particles are different, they consist of particles with either positive or negative charge. Some examples are protons (+), electrons (-), and α -particles (+2). Their interaction probability is greater compared to uncharged. A charged particle may interact at a distance, where its Coulomb field interacts with the Coulomb fields of other nuclei or electrons, causing a “Continuous Slowing Down” (Attix, 1986, p. 160).

1.1.1 Photon interaction in matter

Photons are energy-carrying waves or massless particles traveling at the speed of light. They interact with the surrounding medium in several ways. The main interactions are Rayleigh Scattering, Photoelectric effect, Compton Scattering, pair/triplet production, and photonuclear interactions (Attix, 1986, p.124-125). Which interaction the photon experiences is highly dependent on the atomic number Z of the absorber and the energy of the incoming photon. The probability of interaction is derived from the interaction cross-section, with the unit cm^2 . In Figure 1-1 we see which interaction type dominates for specific photon energies ($h\nu$) and atomic number Z . Pair production is the annihilation of photons in the presence of a nucleus's Coulomb field, producing a positron (e^+) electron (e^-) pair. The interaction demands, at minimum, the rest energy of two electrons ($2m_0c^2 = 1.02 \text{ MeV}$) (Attix, 1986, p.146-148). In this work we will use photons with energies in the keV region, where the photoelectric effect and Compton scattering dominate, and these interaction types will naturally be our focus.

Rayleigh scattering is a relevant interaction type for low energy photons. The photons are deflected from their path, but no energy transfers occur. Hence, Rayleigh scattering does not contribute to the absorbed dose in the medium. Nevertheless, it is still an important interaction type because it gives a complete picture of the photon's path, and the scattered photon may deflect and deposit its energy elsewhere in the medium.

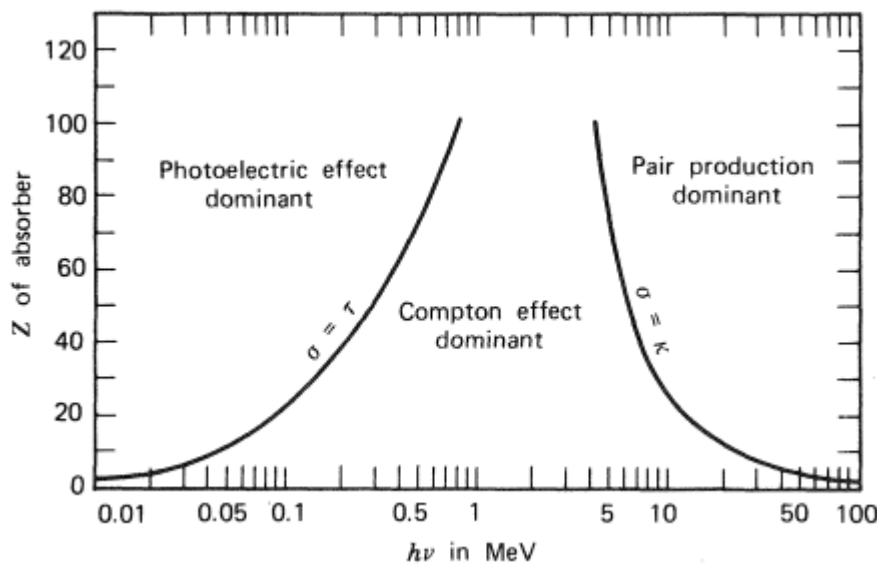


Figure 1-1. Photon interaction probability (defined as interaction cross-section $\sigma [\text{cm}^2]$) as a function of atomic number Z and photon energy $h\nu [\text{MeV}]$. The curves represent the area where two interactions have the same probability (Attix, 1986, p.125).

1.1.1.1 Photoelectric effect

The photoelectric effect is when an incident photon's energy is equal to or larger than the binding energy E_b of an electron, and this energy is completely absorbed by the atom of which the electron is bound to, resulting in liberation of the electron. The kinetics are illustrated in Figure 1-2. The energy transferred from the photon to the electron depends on its initial energy and the electron's binding energy (Attix, 1986, p. 139).

$$T = h\nu - E_b. \quad 1-1$$

The photon might liberate an inner shell electron with higher binding energy (K- or L-shell electron). A looser bound electron will then fill the vacancy. The difference in binding energy is either emitted as characteristic X-rays or by ionization of a valence electron (outer shell electron). The latter is called the Auger effect, and the ionized electrons are called Auger electrons (Attix, 1986, p.143).

The cross-section per atom for the photo-electric effect is proportional to atomic number and incident energy of the photon

$$\tau \propto \frac{Z^n}{(h\nu)^m} \left[\frac{cm^2}{atom} \right], \quad 4 < n < 5, \quad 1 < m < 3,$$

The expression confirms Figure 1-1, as the probability of photoelectric effect increases with atomic number and decreases with energy.

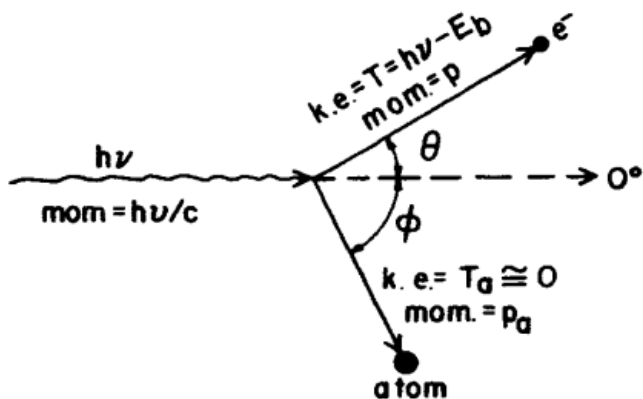


Figure 1-2. Illustration of the photoelectric effect. A bound electron absorbs all the energy of incoming a photon. If the energy is high enough, it will ionize the electron (Attix, 1986, p.138). The kinetic energy of the electron T is dependent on the initial energy of the photon $h\nu$ and the binding energy of the electron E_b . Negligible recoil energy is given to the atom.

1.1.1.2 Compton Scattering

In the Compton scattering process, the photon is scattered against an electron orbiting the nucleus, where the electron is assumed free (Figure 1-3). The errors from this assumption have proved negligible, as they don't become substantial until we have a high atomic number Z and/or low initial energy $h\nu$. When these conditions are met, the photoelectric becomes the dominating interaction type (Attix, 1986,p. 125).

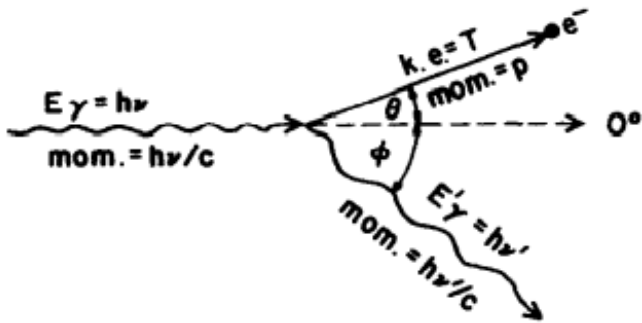


Figure 1-3. Illustration of Compton scattering, where the electron is assumed free. Only part of the incident photon's energy $h\nu$ is transferred to the electron.

In the Compton process, the photon only transfers part of its energy to the electron. The energy of the scattered photon follows this expression

$$h\nu' = \frac{h\nu}{1 + \frac{h\nu}{(m_e c^2)(1 - \cos\phi)}}, \quad 1-2$$

where $m_e c^2$ is the rest energy of the electron. The expression is derived in section 7.1 and shows strong correlation between the energy and the angle of the scattered photon. The maximum energy transfer to the electron is found when the photon is scattered 180° , known as backscatter. The Compton cross section σ per electron was derived by Klein and Nishina. They improved on the existing theory of Thomson scattering. Thomson's cross section was independent of incident photon energy, and assumed $h\nu = h\nu'$ (Attix, 1986, p.130). This is correct for low energies. However, in Figure 1-4 we see the energy of the scattered photon starts decreasing for increasing energy and scattering angle around 0.01 MeV , and reaches its minimum for 180° around 54 MeV .

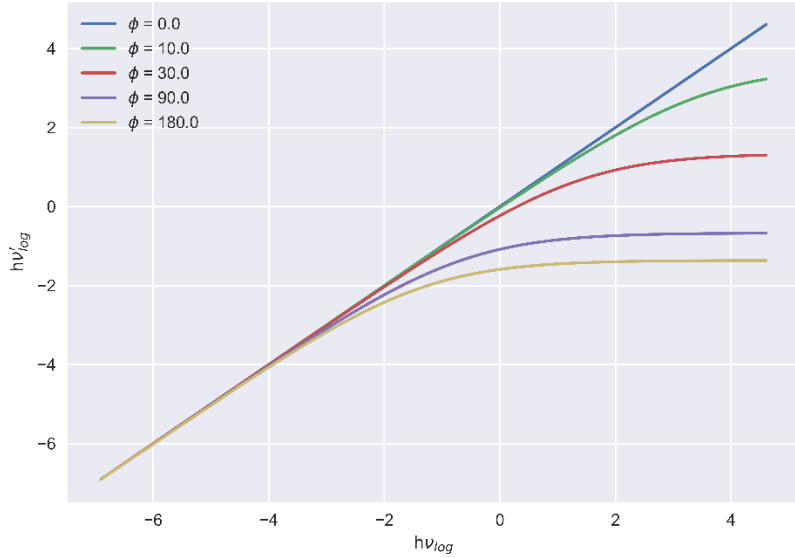


Figure 1-4. Compton scatter energies in log MeV for different scattering angles ϕ . $h\nu$ is the energy of incident photon, $h\nu'$ is the energy of the scattered photon.

1.1.1.3 Attenuation coefficient and derived quantities

Each photon interaction has a probability of occurring known as a cross section. The cross section for the photo-electric effect is denoted τ , Compton scatter has σ , pair production has κ and Rayleigh scattering has σ_R . It is practical to sum each cross section to generate a combined interaction parameter. It is defined as the attenuation coefficient:

$$\mu = \sigma + \tau + \kappa + \sigma_R \text{ [cm}^2/\text{atom]}. \quad 1-3$$

However, it is more insightful to normalize it with density ρ . In this way, we get $\mu/\rho \left[\frac{\text{cm}^2}{\text{g}} \right]$,

which represents the attenuation of photons per unit density. This is called the **mass attenuation coefficient**.

For polyenergetic photons, the coefficient must be averaged over the full energy spectrum of the photons, but for simplicity we will assume monoenergetic photons.

We can now define a new quantity, which is the attenuation coefficient weighted with the fraction of kinetic energy transferred from the incident photon to the secondary electron. This is called the **mass energy-transfer coefficient**

$$\frac{\mu_{tr}}{\rho} = \frac{\sigma}{\rho} \cdot \frac{\bar{T}}{h\nu}, \quad 1-4$$

Where \bar{T} is the mean energy of the liberated electron after any of the photon interaction processes. \bar{T} depends on the given interaction, and will e.g., be close to $h\nu$ for the photoelectric effect. The last quantity we want is the **mass energy-absorption coefficient** μ_{en}/ρ . It reflects the energy absorbed by the volume in terms of collision losses by the secondary electrons (see below). It relates to the mass energy-transfer coefficient by

$$\frac{\mu_{en}}{\rho} = \frac{\mu_{tr}}{\rho} (1 - g), \quad 1-5$$

Where g is the fraction of energy lost by secondary electrons to so-called radiative loss (Attix, 1986, p.155-156).

1.1.1.4 Photon range

Mean free path is the expected distance a photon will travel before interacting with the medium (*Mean Free Path / Physics / Britannica*, 2007). In section 7.2 we derive an expression for mean free path for a photon traversing a slab of material:

$$\langle x \rangle = \frac{1}{\mu}. \quad 1-6$$

The pathlength of the photon decreases with increasing attenuation coefficient. This is an important result because it allows for prediction a photons' path. It is especially useful when performing Monte Carlo (MC) simulations, which we will return to in 2.1.2.4.

1.1.2 Charged Particle interaction in matter

A charged particle has either positive or negative net electrical charge, such as electrons (e^-), protons (e^+) and ions (an atom with a surplus of electrons or protons). Because of their charge, the particles will interact with other charged particles through their Coulomb fields. Two equal charges will repel, and two opposite charges will attract. A charged particle traversing a medium is surrounded by a Coulomb electric field, enabling the charged particles to interact at a distance. This distance is known as the impact parameter and is defined as the closest distance from the charged particle trajectory to the target atom. There are three main categories of interactions: Soft collisions, hard collisions, and interactions with the nucleus.

1.1.2.1 Soft collisions

Soft collisions are weak Coulomb interactions between the Coulomb fields of an atom and a charged particle. The impact parameter is much larger than the atomic radius (distance from valence electrons to nuclei), and small amounts of energy are transferred to orbiting electrons, mainly causing excitations. Even though the energy transfers are very small, the interaction is highly probable, therefore contributing to half of the energy loss of the charge particle (Attix, 1986, p.161).

1.1.2.2 Hard collision

Hard collisions happen when the impact parameter has the same order of magnitude as the atomic radius. The result is a significant kinetic energy transfer to an assumed free and stationary electron. These electrons are called δ -rays, which undergo the same charge particle interactions. The hard collisions might also result in liberation of an inner shell electron as described in 1.1.1.1, resulting in emission of characteristic X-rays (Attix, 1986, p.162).

1.1.2.3 Radiative transfer

Radiative transfer, also known as bremsstrahlung, is a process where a charged particle interacts with the nucleus's Coulomb field (Figure 1-5). The impact parameter must be much lower than the atomic radius for this to happen. The interaction mainly occurs for electrons (Attix, 1986, p.163). The electron with its negative charge is attracted to the nucleus's positive charge, causing a deacceleration and deflection of the electron from its incident path. The decrease in kinetic energy ΔE_e is converted to a photon, thus conserving energy.

The probability of radiative transfer is much lower to that of elastic scattering (2-3%) and is proportional to $q^2 Z^2 T / M_e^2$ (Grieken & Markowicz, 1993, p.3), where q is the charge, Z the atomic number of the atom, T the kinetic energy of the electron and M_e the rest mass of the electron. With a larger Z , the atom has a higher proton count, resulting in the nucleus having a larger Coulomb field attracting the electron. The kinetic energy of the electron is important because the electron needs to penetrate the electron cloud surrounding the nucleus.

Radiative transfer is used when generating X-rays inside an X-ray tube, but we will come back to this in section (1.2.1).

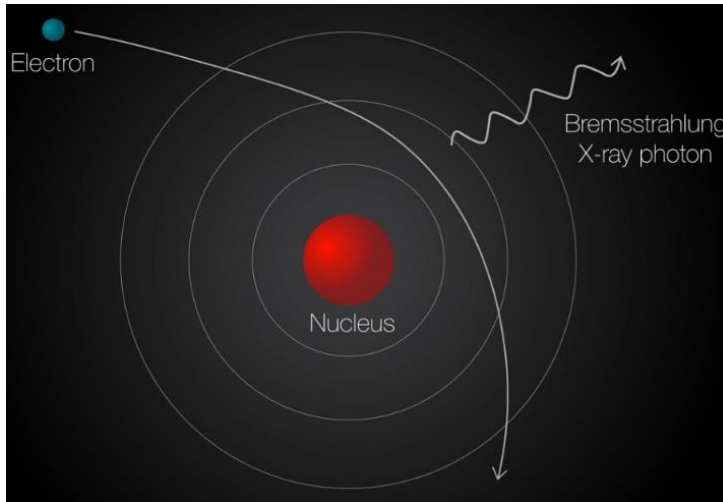


Figure 1-5. Illustration of radiative transfer, where an electron inelastically collides with an atom's nucleus deflecting it from its path. The result is an emitted photon with energy equal to the energy loss of the electron (Hapugoda, 2017).

1.1.2.4 Stopping Power

Stopping power is how much energy the charged particle is expected to lose per unit length. It can be found by integrating the differential energy loss over all possible energy transfers for a given particle and absorber combination.

As discussed, the charged particle might lose its energy by colliding or by radiative transfer; we therefore separate these contributions (Attix, 1986, .165)

$$S = S_c + S_r$$

Energy lost to radiative transfer does not contribute to local dose, because of the longer range of the bremsstrahlung. Radiative stopping power is still important to accurately describe the range of the charged particle.

Collision stopping power may be split into two parts: S_{soft} and S_{hard} . Energy loss is dependent on the material it penetrates, and we therefore introduce **mass stopping power** by dividing the stopping power by the material density S/ρ .

The total collision mass stopping power, including soft and hard collisions, is

$$\frac{4\pi N_A Z}{A} \frac{r_e^2 m_e c^2}{\beta^2} z^2 \left[\ln \frac{2m_e v^2}{I} - \ln(1 - \beta^2) - \beta^2 - \frac{C}{Z} \right] \left[MeV \frac{cm^2}{g} \right]. \quad 1-7$$

Where $N_A Z/A$ is the number of electrons per gram, r_e the classical electron radius, $\beta = v/c$, I the mean excitation potential in the medium, z the electron charge, and C/Z the shell correction. The collision stopping power assumes the electron's velocity to be much greater than that of the orbiting electrons in atoms. As the particle slows down the assumption becomes less true, and the shell correction handles this. Stopping power is inversely dependent on the square of the velocity and electrons with high kinetic energy will thus have relatively low stopping power.

Mass collision stopping power is closely related to absorbed dose (energy absorbed per mass). If the energy deposition is solely due to charged particles, the absorbed dose (1.3.1.3) is expressed as

$$D = \phi \frac{S_c}{\rho} [Gy],$$

ϕ is electron fluence for a radiation field (1.3.1) (Seuntjens et al., 2005).

Stopping power is useful because we can estimate the range of the charged particle but is also needed to calculate how much energy is absorbed locally by the medium. Linear Energy Transfer (LET) represents this quantity in units of $keV/\mu m$. It is also known as restricted stopping power (Attix, 1986, p.179). When high energy electrons experience hard collisions, they liberate secondary electrons. A cutoff energy Δ is introduced, because some electrons might have sufficient energy to escape the “local” volume of interest. If none of the secondary electrons escape (i.e., the volume is large or the energy transfer is low), we have:

$$LET = S_c.$$

LET is especially important in radiobiology because it estimates the rate of energy depositions, i.e., the ionization density. A high ionization density may result in more damage per absorbed dose.

1.1.2.5 Continuous slowing down approximation - CSDA

If we assume that the electrons are continuously slowing down (i.e., neglecting fluctuations in energy loss) as they interact, we can integrate total mass stopping power to get an approximate range called the continuously slowing down approximation (CSDA) range

$$R_{CSDA} = \int_0^{T_{max}} \frac{dT_{c+r}}{\rho dx} \left[\frac{g}{cm^2} \right].$$

This enables the description of the expected path of charged particles. As it describes the total range of the particle including all twists and turns, it is different to **projected range**, which measures how deep into the medium the particle penetrates (Attix, 1986, p.181). Because the charged particles transfer their energy continuously, the CSDA range is important to give an insight into the damaging capabilities of the charged particles following an ionization event (Saxena et al., 2011).

1.2 Radiation beam generation

When treating or diagnosing patients using radiation, you need a stable and reliable beam. Various techniques are used for this purpose, but we will focus on the X-ray tube.

1.2.1 X-ray tube

The X-ray tube's purpose is to convert electron energy into X-rays. As mentioned in 1.1.2 we have two interaction types generating X-rays from electrons interacting with matter. The first is characteristic X-rays generated after ionization of an inner-shell electron and the second is generation of bremsstrahlung from deacceleration of electrons traversing close to the atomic nucleus. In Figure 1-6 we see an illustration of an X-ray tube. The first component of the X-ray tube is the cathode, which is a spiraled wire called the filament. The filament is often placed inside a glass chamber called the envelope (Nadrljanski, 2021b). The filament is heated through resistance heating of a wire running through the cathode (Goel, 2021). When the cathode reaches the right temperature, it will emit electrons through thermionic emission. This is a process where the heating energy surpasses the binding energy of electrons, and they are emitted from the metallic structure (*Thermionic Emission / Physics / Britannica*, 2021). The electrons are released into an evacuated tube with a high voltage. The potential difference accelerates the electrons toward a positively charged anode/target. Most anodes in x-ray tube targets are made of tungsten, because of their high atomic number and high melting point (Nadrljanski, 2021a).

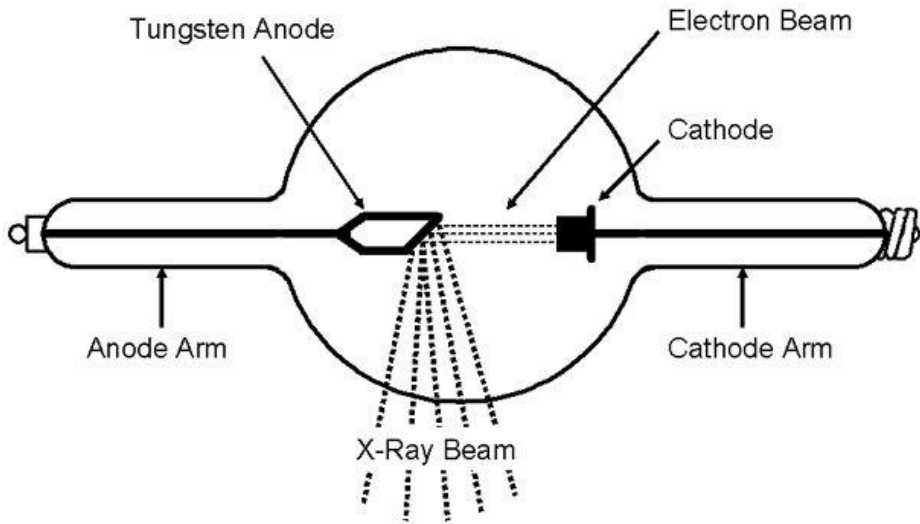


Figure 1-6. X-ray tube with heated cathode, that releases electrons into the vacuum sealed tube with potential difference kV causing acceleration of the electrons. The electrons strike a target of high density material generating bremsstrahlung. Image reference (Aksnes, 2020).

The electrons generate bremsstrahlung at different impact parameters (section 1.1.2.3), generating a spectrum of possible X-ray energies, which is decided by Kramer's rule. The essence of this rule is that when electrons strike a thick target the probability of direct impact with the nucleus, i.e., when the impact parameter is 0, is minute. It is more probable that the electron experiences many smaller energy transfers, gradually deaccelerating generating X-rays with less energy (Attix, 1986, p.211-214). Still the maximum X-ray energy equates the kinetic energy of the electrons hitting the target. X-ray tubes typically have voltages up to 200 kV, with corresponding maximum photon energy of 200 keV. The intensity of the beam follows the inverse square law where intensity decreases with the square of the distance away from the source following the equation (Attix, 1986, p.44)

$$I = \alpha/r^2 ,$$

where α is a proportionality constant.

1.2.2 X-ray filtering

It is often desirable to remove the lower energy X-rays from the X-ray beam. As seen in Figure 1-1 photons within a lower energy range have an increased probability of experiencing the

photoelectric effect, where all energy is lost to an atom. If a person were to be treated with X-rays, and the tumor was positioned deep inside the body, the low energy photons would only contribute to a higher skin dose. X-ray filtering (a.k.a. beam hardening) is done by inserting a filter in front of the X-ray beam. The filter attenuates lower energy X-rays and creates a more homogeneous energy spectrum shifted towards higher energies. In Figure 1-7 we observe the difference between an unfiltered (red) and filtered (blue) X-ray beam generated in an X-ray tube with a tungsten as target. The first peak are photons emitted following ionization of L-shell electrons. While the second and third peak are X-rays emitted after ionization of K-shell electrons (Amiri et al., 2021).

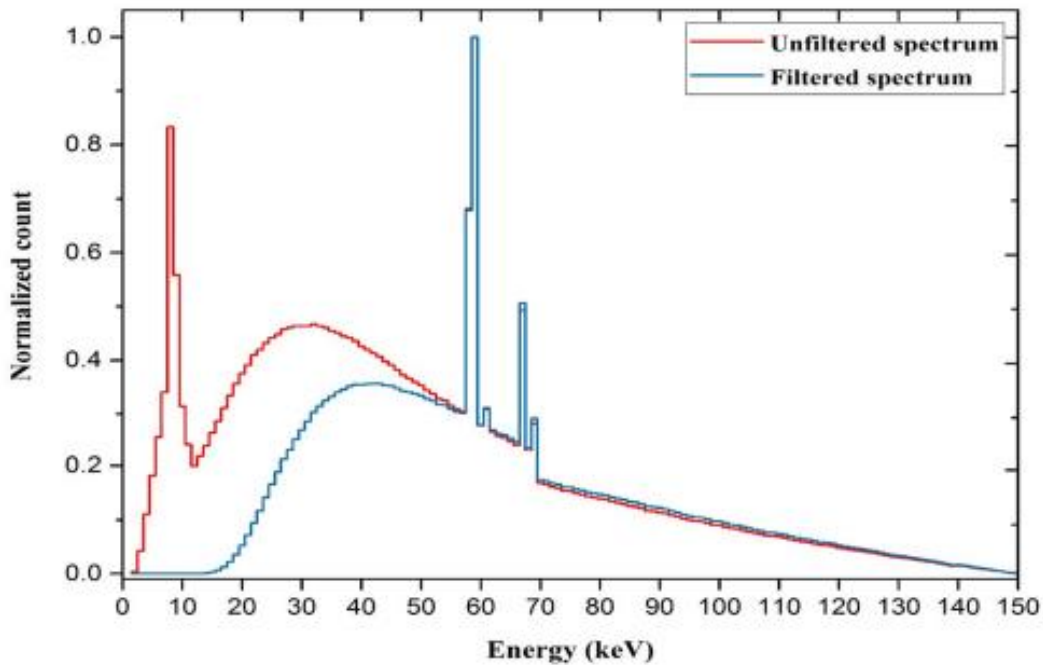


Figure 1-7. Unfiltered (red) vs filtered (blue) X-ray energy spectrum generated from a Tungsten anode where filtering is obtained with 2.5 mm aluminum (Amiri et al., 2021).

1.3 Dosimetry

Radiation dose is dependent on the energy, exposure time, distance from source, material of the absorber and quality (e.g., photons, protons or neutrons) of the radiation. To measure the dose, the solution has been to use the effects of radiation on different substances such as discoloring

(film dosimeter), temperature change (calorimeter) and light emission (thermoluminescence). To understand dosimetry, it is necessary to define some important quantities.

1.3.1 Quantities

1.3.1.1 Ionizing radiation field

Assume that the number of rays or particles traversing a point P, defined by a sphere with infinitesimal volume dV , mass dm and cross-sectional area da , inside a field of ionizing radiation (Attix, 1986, p.5-6) (Figure 1-8) The number of traversing rays per cross sectional area da is defined as **fluence Φ** .

$$\Phi = \frac{dN}{da}$$

If the number of rays differs over time, a quantity called the fluence rate (rays per area per time), needs to be integrated over time to get the fluence. The radiant energy of the rays is equally important as the number of rays. For a polyenergetic beam with energies E, we define **energy fluence Ψ**

$$\Psi = \frac{d^2N(E)}{dadE} = \frac{d\Phi(E)}{dE}$$

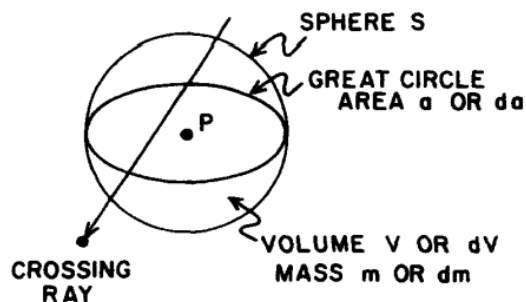


Figure 1-8. Ionizing radiation field defined at a point P defined by an infinitesimal volume dV , mass dm and cross sectional area da (Attix, 1986, p.6).

1.3.1.2 KERMA

With the energy fluence we have the energy spectrum of the rays traversing the sphere, but to get a dose we need the rays to interact and release energy. This is where KERMA, Kinetic Energy Release per Mass, comes in. It describes the process where uncharged particles (photons or

neutrons) enter a defined volume and transfers some or all their energy to electrons in the volume. The energy transfer is expressed as

$$\epsilon_{tr} = R_{\gamma,in} - R_{\gamma-rl,out} + \Sigma Q , \quad 1-8$$

Where ϵ_{tr} is the expected energy transferred from uncharged radiation with energy $R_{\gamma,in}$ into the volume minus the energy of the uncharged radiation $R_{\gamma-rl,out}$ leaving the volume without interacting.

RL stands for radiative losses and represents interactions where charged particles generate photon energy after the initial ionization. If these photons leave the volume, it does not matter because we are only interested in the energy transferred by the incident particles entering the volume.

The final term is conversion of rest mass to energy or energy to rest mass. For instance, pair production (section 1.1.1) where a photon annihilates in the presence of a nucleus generating an electron positron pair, which equates two times the rest mass of an electron (1.022 MeV).

With ϵ_{tr} we can define KERMA

$$K = \frac{d\epsilon_{tr}}{dm} \left[\frac{J}{kg} \right] \quad 1-9$$

For monoenergetic photons, KERMA is related to energy fluence using the expression

$$K = \Psi \frac{\mu_{tr}}{\rho} ,$$

Where μ_{tr}/ρ is the mass energy transfer coefficient (section 1.1.1.3) which represents the probability of the photons transferring a fractional energy to the volume (Attix, 1986, p. 21-22).

Until now, we have neglected how the electrons have spent their energy after they have received it from the incident photons. Accounting for radiative loss gives net energy transfer ϵ_{tr}^n represented by the expression

$$\epsilon_{tr}^n = R_{\gamma,in} - R_{\gamma,out} + \Sigma Q .$$

ϵ_{tr}^n represents the energy of the electrons, not lost to radiative transfer. We can now separate KERMA into two parts: collision KERMA K_c and radiative KERMA K_r , where K_c for monoenergetic photons is expressed as

$$K_c = \frac{d\epsilon_{tr}^n}{dm} .$$

We can relate K_c and energy fluence to another quantity: mass energy-absorption coefficient μ_{en}/ρ (1.1.1.3) (Attix, 1986, p.24-25)

$$K_c = \Psi \frac{\mu_{en}}{\rho} .$$

1.3.1.3 Absorbed dose

When describing KERMA, we are interested in how energy is transferred from the photon to the medium. But photons are not the only contributors to dose. As mentioned, charged particles transfer additional energy to the volume. We therefore define total energy transfer as

$$\epsilon = R_{e,in} + R_{\gamma,in} - R_{e,out} - R_{\gamma,out} + \Sigma Q$$

Where we include the energy transferred by charged particles R_e entering and exiting the volume. It is now possible to define absorbed dose as (Attix, 1986, p.26-27)

$$D = \frac{d\epsilon}{dm} [J/kg].$$

The unit is the same as KERMA, but it is called Gray or Gy. The unit is especially important in radiobiology because the amount of absorbed energy affect an organism's chance of repairing the damage caused by the radiation (see 1.7.3).

1.3.1.4 Photon dose deposition

Dose distribution from a photon beam is dependent on the energy of the photons and the atomic composition of the absorber. A typical percentage depth dose (PDD) curve from photon beams of varying energies is shown in

Figure 1-9. A PDD represent the relative dose at a depth in a medium (often water). As photons attenuate through the medium, they dissipate their energy by interactions mentioned in 1.1.1. For high-energy photons we see a buildup of dose. High energy photons generate charged particles with high kinetic energies and low stopping power (equation 1-7). The charged particles will

therefore travel some distance into the medium before transferring their energy as absorbed dose. For keV photons the buildup is small but not negligible.

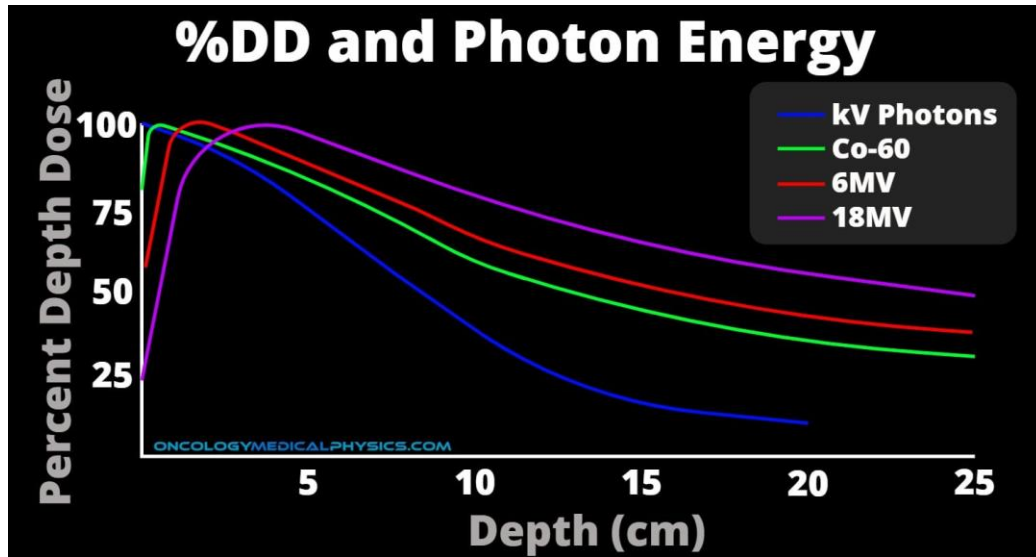


Figure 1-9. Percent Depth Dose curve for photon beams of different energies. As the photons attenuate through the medium they lose energy to electrons, which in turn lose energy through various interactions. A buildup region is seen for high energy photons before the maximum relative dose is reached. The same effect is low, but not negligible for photons in the kV energy range (Photon Dose Distributions | Oncology Medical Physics, n.d.).

1.3.1.5 Exposure

Exposure is defined as total charge Q of ions of one sign (+ or -) produced by X-rays or γ -rays per mass m of air when all secondary electrons are stopped in the air and charged particle equilibrium (see next paragraph) is achieved (Attix, 1986, p.29-30). The expression for exposure in an infinitesimal air volume is

$$X = \frac{dQ}{dm} \quad [C/kg]. \quad 1-10$$

We can relate exposure to mass energy absorption coefficient (μ_{en}/ρ) and energy fluence Ψ by introducing the variable \bar{W} . \bar{W} is the mean energy required to create an ion pair (Podgorsak, 2016, p. 744). The resulting expression for monoenergetic photons is

$$X = \Psi \left(\frac{\mu_{en}}{\rho} \right)_{air} \left(\frac{e}{\bar{W}} \right)_{air} = K_c \left(\frac{e}{\bar{W}} \right)_{air}. \quad 1-11$$

e is the elementary charge.

1.3.1.6 Charged Particle Equilibrium (CPE)

If $R_{e,in} = R_{e,out}$ the energy distribution of charged particles entering the volume is equal to the energy distribution of charged particles leaving the volume (visualized in Figure 1-10) (Attix, 1986, p.65), we have **charged particle equilibrium** (CPE), and reduces absorbed dose to K_c (Attix, 1986, p.69).

$$D = K_c = \Psi \frac{\mu_{en}}{\rho}. \quad 1-12$$

CPE essentially demands constant photon fluence everywhere around and within the smaller volume v in Figure 1-10. If the fluence dropped significantly when entering the large volume V , more secondary electrons would be generated at the entrance of v , compared to the exit and we do not have CPE (Attix, 1986, p.67). When CPE is achieved, we can easily find the dose ratio between two volumes. This is a practical metric because we often need to relate dose to mediums of different atomic compositions. CPE is not necessarily easy to achieve. If the volumes are near the source, we will have much higher fluence on the side closest to the source (Attix, 1986, p.72). This causes more ionizations closer to the surface of V , compared to the surface of v and CPE fails. For larger photon energies, the range of the liberated charged particles will increase compared to the range of the photons, because of decreased stopping power (equation 1-7). Thus, there will be more charged particles generated near the surface of V that reaches v , compared to charged particles generated at the entrance of v and CPE fails.

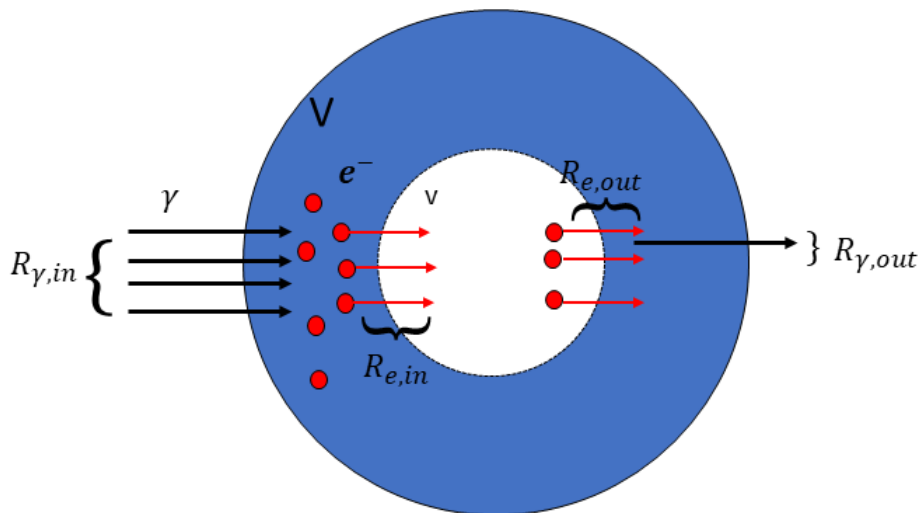


Figure 1-10. Charged particle equilibrium visualized, where photon energy enters a volume V transferring energy to charged particles (electrons in this case), that traverses a smaller volume v . The electrons exiting v are of same type and energy distribution as the electrons entering, and we have CPE.

1.4 Cavity Theory

When measuring dose, a dosimeter is used. A very popular dosimeter is the ionization chamber, which we will discuss in detail (1.5). A simple description of an ion chamber is a gas filled chamber connected to an electrometer. Radiation ionizes the gas, and the electrometer measures a charge proportional to absorbed dose. However, dose (a.k.a., energy absorbed in the medium) is not equal between mediums of different atomic composition. We therefore need to relate the dose absorbed measured in the gas to the medium we are interested in. The situation is visualized in Figure 1-11.

1.4.1 Bragg-Gray cavity

In Bragg-Gray cavity theory, dose to water is related to dose to air by

$$D_W = D_{Air} \cdot \left(\frac{S}{\rho}\right)^w_{air},$$

where $\left(\frac{S}{\rho}\right)^{air}_w$ is the mass stopping power ratio between water and air. Dose to water is often used because radiation beams in the clinic are calibrated with the assumption that all tissues in the human body are “water-like” (Andreo, 2015). We see that the electron fluence is assumed constant, but for this to be true two conditions needs to be fulfilled (Attix, 1986, p. 232):

1. The fluence of charged particles should not be perturbed in the cavity
2. Only charged particles crossing the cavity contributes to the dose.

The second condition requires no significant attenuation of photons inside the cavity, which in turn requires an infinitesimally dimensioned cavity. Gray calculated the size that satisfies these conditions and found that for unfiltered γ -radiation you would need a 3 cm^3 air volume, while 100 kV X-rays require 0.1 cm^3 for air filled cavity with graphite walls (Alm Carlsson, 2001).

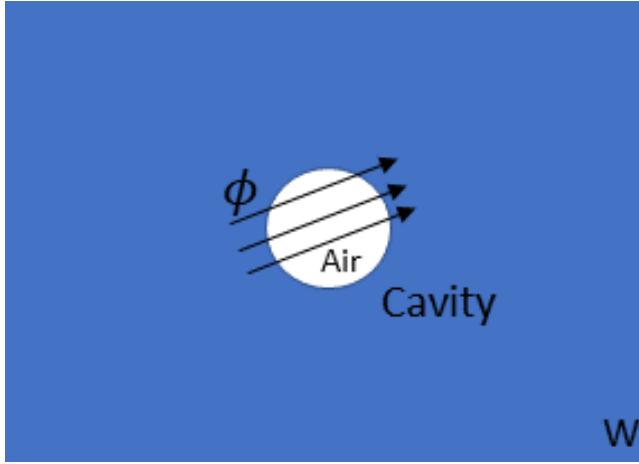


Figure 1-11. A volume with material w (e.g., water), with an air-filled cavity inside. Energy Ψ traverses the volume releasing electrons contributing to dose inside the cavity.

1.4.2 Bragg-Gray-Laurence

The ideal Bragg-Gray scenario is not possible, as it would require an infinitesimally dimensioned dosimeter not to alter the charged particle fluence. It also demands the stopping power ratio

$\left(\frac{S}{\rho}\right)_W^{Air}$ to be independent of energy, which is not the case for increasingly different mediums

(Alm Carlsson, 2002). The theory was improved by introducing CSDA of the charged particles. This allows the charged particles to slow down inside the cavity, and we need to integrate over the stopping power ratio

$$\frac{D_w}{D_{air}} = \int_0^{T_{max}} \frac{\phi(T) \left(\frac{S}{\rho}\right)_w}{\phi(T) \left(\frac{S}{\rho}\right)_{air}} dT.$$

Bragg-Gray-Laurence in its simplest form requires CPE to accurately calculate the energy distribution of the electrons (Alm Carlsson, 2001). It might seem like a contradiction to incorporate CSDA, because CPE requires the energy of entering charged particles to be equal to the energy of the exiting charged particles. However, the cavity is still assumed to be small compared to the charged particle range and the energy loss inside the cavity is negligible. And because of the small size of the cavity, even small energy transfers will result in a significant dose.

The Bragg-Gray-Laurence cavity theory does not account for secondary electrons (δ -rays) generated inside the cavity. The **Spencer-Attix** cavity theory accounts for these electrons, and

sets a cutoff energy Δ , where all δ -rays with energy higher than Δ escapes the cavity. As a result, more low energy electrons are added to the fluence.

1.5 Dosimetry methods

As mentioned in 1.3 different techniques are used for dose measurements. However, this thesis will focus on two different dosimeters: Ionization chamber and Radiochromic film dosimeter. These dosimeters fall into one of two categories: Absolute and relative dosimeters. An absolute dosimeter responds to radiation in such a way that we are able to directly measure the received dose and does not require calibration in a known radiation field (Attix, 1986, p. 277). For instance, a free-air ionization chamber is an ionization chamber without walls, where the goal is to measure exposure 1.3.1.5 in a known mass of air. However, for photon energies surpassing 1.5 MeV the secondary electrons have such a large range that the free-air ionization chamber cannot fulfill CPE without becoming unpractically large (Podgorsak, 2016, p. 737). The ionization chambers we will discuss here are relative dosimeters.

1.5.1 Parallel- Plate Ionization Chamber

The purpose of an ionization chamber is measuring ionizations inside a gas-filled cavity. A fundamental type of ionization chamber is the parallel plate chamber illustrated in Figure 1-12. The chamber is connected to a polarizing (negative cathode) and measuring electrode (positive anode). The polarizing electrode is directly connected to the power supply and creates the voltage difference, which in turn generates an electric field. Adjacent to the measuring electrode you have the guarding ring/electrode with the purpose of preventing leaking current from being measured by the electrometer (Podgorsak, 2016, p. 702). Looking at Figure 1-12 you see that the electrometer is connected to the power supply. Ideally the impedance (a circuit's opposition to charge) inside the electrometer is sufficiently high (typically $10^{14} \Omega$) and no charge moves through it (*High Accuracy Electrometers for Low Current/High Resistance Applications / Tektronix, n.d.*). However, some leakage will occur, and the guard rings are there to prevent this from being measured. The second purpose is to help define the effective collection volume of the chamber (see 1.5.2), by ensuring straight electric field lines (Podgorsak, 2016, p.703).

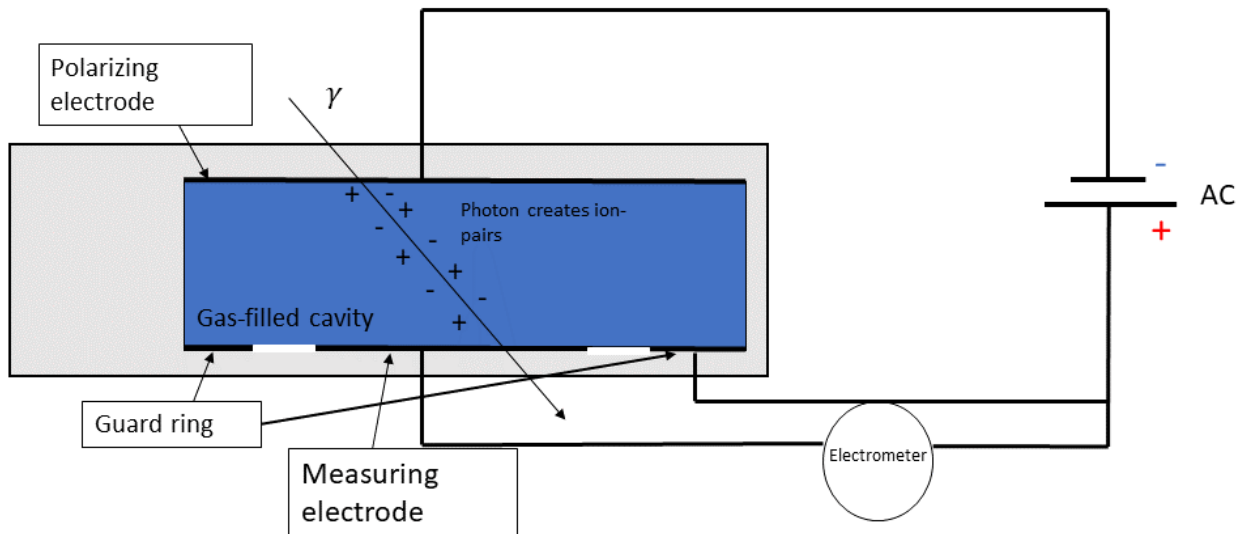


Figure 1-12. The schematics of a parallel plate ionization chambers. An electric field is established on the gas-filled cavity, so when the gas is ionized electrons will move toward the positively charged side, where they are collected by a measuring electrode connected to an electrometer.

When the electrons are ionized the charge is “collected” by a measuring electrode connected to the electrometer (Podgorsak, 2016, p.705). The electrometer measures the accumulated charge, which is converted to dose using a calibration factor. If the applied voltage is too low negative ions will tend to recombine with positive ions. The solution is increasing the voltage until the measured current is no longer dependent on voltage, which is called the saturation region (Attix, 1986, p.330-331). The measured output in this region is known as the saturation charge, or Q_{sat} .

1.5.2 Thimble Ionization Chamber

In Figure 1-13 we see a thimble (a.k.a. farmer type) ionization chamber. The chamber differs from the parallel-plate type by having a graphite thimble surrounding the gas-filled cavity. The graphite is chosen because it protects the sensitive volume and is air equivalent, therefore minimizing the density difference between cavity and wall. This achieves charged particle equilibrium (Shortt et al., 2002). The protection cap is not shown in Figure 1-13 but it surrounds the wall and acts as a buildup material that ensures CPE within the sensitive volume of the ionization chamber (1.1.2.4). The chamber has a central electrode connected to the electrometer.

In a thimble ionization chamber, exposure is the quantity of interest (1.3.1.5) to measure absorbed dose in the sensitive volume. Rearranging equation 1-11 we see that collision KERMA can be written as

$$K_c = X \left(\frac{\bar{W}}{e} \right).$$

From equation 1-10 we have the expression for exposure. Replacing the infinitesimal dQ/dm with the saturated charge Q_{sat} and total air mass m_{air} , we get collision KERMA for air

$$K_{air} = \frac{Q_{sat}}{m_{air}} \left(\frac{\bar{W}}{e} \right).$$

CPE is achieved in a thimble ionization chamber, so absorbed dose can be found using equation 1-12. But the challenge arises when finding m_{air} . m_{air} is found using the effective volume, which is not necessarily the same as the geometrical volume of the chamber. The effective volume is defined by the electric field lines running from polarizing electrode to measuring electrode (Podgorsak, 2016, p.745). The field lines tend to bend outward away from the center, and this affects the fate of the ionized electron, thereby affecting the effective volume where electrons can be collected. To ensure most accurate dose measurement, a primary standards laboratory is given the job of calibrating the ionization chamber and finding its effective volume. The calibration of a thimble ionization chamber is performed by measuring exposure X using a free-air chamber, then replacing it with a thimble chamber and measure the air KERMA K_{air} . The measurements are performed under specific reference conditions such as temperature, air pressure and humidity, using a reference beam energy and quality (typically ^{60}Co photons). From this a calibration factor N_k is found that relates output in nC to dose Gy (Podgorsak, 2016, p.744). The thimble chamber is then inserted into a water phantom, still in the known radiation field, where the K_{air} is measured again and converted to dose to unperturbed water (as if the ionization chamber was not present) using a conversion factor and correction factors (P.Andreo et al., 1996, p.48).

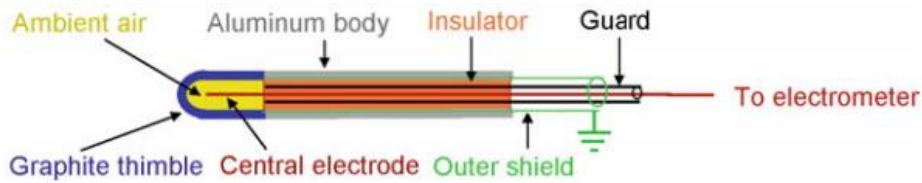


Figure 1-13. Schematic of thimble ionization chamber, where the sensitive air-filled volume is encapsulated in a thimble (Podgorsak, 2016, p. 741).

1.5.3 Radiochromic film

Radiochromic film is a self-developing film, that reacts when exposed to radiation (McLaughlin & Chalkley, 1965). The films are typically made up of a protective layer and an active layer (Figure 1-14) The active layer consists of one or two layers of monomers called diacetylene. Monomers are molecules that interact with other monomer molecules to create polymer chains (Monomer / Definition & Facts / Britannica, 2022). When diacetylene is exposed to radiation it polymerizes to create polydiacetylene, changing both the chemical and optical characteristic of the active layer (McLaughlin et al., 1996). The color of the film darkens and the optical density (OD) can be measured either by measuring light transmitted through the film, or light reflected by the film (Andreou et al., 2017, 562). Extracting absolute dose from the films requires an



Figure 1-14. Different radiochromic film structures used for external beam therapy (EBT) (Devic et al., 2016). The active layer is made from monomers that polymerize when exposed to radiation, causing a darkening of the film. The optical density (OD) is measured and related to dose.

established relationship between the film response and absorbed dose, which demands calibration of the films and accounting for factors that might change the response, such as time

waited after irradiation before scanning the films, temperature and light exposure (Girard et al., 2012; Park et al., 2012). New calibrations are necessary for every new batch, because of batch to-batch variation caused by e.g., variation in the thickness of the sensitive layer or different scanner sensitivities (Devic et al., 2016).

1.6 Statistics

1.6.1 Non-linear curve fit

Regression is a tool used for analyzing data and making predictions. In traditional linear regression there is a dataset containing m response/dependent variables \mathbf{y} and n explanatory/independent variables \mathbf{x} . Linear regression tries to find the optimal coefficients/parameters $\hat{\boldsymbol{\beta}}$, that fits the equation

$$y_i = \beta_0 + \beta_1 x_0 + \beta_2 x_1 + \cdots + \beta_n x_n, \quad 1-13$$

using the method of least squares. An example would be to find the line (or plane) that minimizes the deviation between the true response variables y_i and the estimated values \hat{y}_i . $\boldsymbol{\beta}^T = [\beta_0, \beta_1 \dots, \beta_n]$ represents the coefficients that links the dependence of \mathbf{y} to \mathbf{x} , while $\hat{\boldsymbol{\beta}}$ is the estimated coefficients. The linear regression does not account for measurement error in \mathbf{x} itself, which might lead to the coefficients being biased towards zero (Griliches & Ringstad, 1970). However, accounting for this is beyond the scope of this thesis. The deviation is defined as the cost function, and both linear and nonlinear regression uses the sum of squared residuals (RSS)

$$RSS = \sum_{i=0}^m \left(\frac{y_i - \hat{y}_i(\mathbf{x}_i)}{\sigma_{y,i}} \right)^2, \quad 1-14$$

where $\sigma_{y,i}$ is the individual weight of the i^{th} residual, which is used when the assumption of approximately equal residual for every \hat{y}_i (homoscedasticity) is not satisfied (Kirkup, 2012, p.264). RSS is otherwise $\sum_{i=0}^m (y_i - \hat{y}_i(\mathbf{x}_i))^2$. For a first order linear regression, one can differentiate the RSS with relation to both coefficients β_0 and β_1 and find a closed form expression for both coefficients (Bingham & Fry, 2010, p.3-5).

However, not all response variables are linearly dependent on the explanatory variables, which might lead to the RSS not having a closed form solution when differentiated. The solution is to

guess the values of the unknown coefficients, and then iteratively tune them to find the minimum RSS (Kirkup, 2012, p.335-337).

1.6.1.1 Levenberg-Marquardt algorithm

This section is based on (Gavin, 2020).

Levenberg-Marquardt algorithm (LM) combines two minimization methods known as the Gradient descent (GD) and the Gaussian-Newton (GN) method. **GD** uses the derivative of the RSS to update the parameters towards the steepest descent towards the minimum of RSS. For all n parameters $\mathbf{p}^T = [p_0, p_1, \dots, p_n]$ we have a weighted RSS of

$$(\mathbf{y}(\mathbf{x}) - \hat{\mathbf{y}}(\mathbf{x}; \mathbf{p}))^T \mathbf{W} (\mathbf{y}(\mathbf{x}) - \hat{\mathbf{y}}(\mathbf{x}; \mathbf{p})), \quad 1-15$$

\mathbf{W} is a diagonal matrix with shape m x m for m datapoints, with all the weights on the diagonal. Using the second binomial formula we remove the parentheses and get

$$\mathbf{y}^T \mathbf{W} \mathbf{y} - 2\mathbf{y}^T \mathbf{W} \hat{\mathbf{y}} + \hat{\mathbf{y}}^T \mathbf{W} \hat{\mathbf{y}} \quad 1-16$$

Differentiating the RSS w.r.t. all parameters we get

$$-2 (\mathbf{y} - \hat{\mathbf{y}})^T \mathbf{W} \mathbf{J},$$

where \mathbf{J} is the m x n Jacobian matrix containing the partial derivatives of $\partial \hat{\mathbf{y}} / \partial \mathbf{p}$. The two factor comes from the fact that RSS is squared, and the minus sign is from $-\hat{\mathbf{y}}(\mathbf{x}; \mathbf{p})$. The partial derivatives $\partial \mathbf{y} / \partial \mathbf{p}$ becomes 0 because \mathbf{y} does not vary with changing parameters.

Rearranging the expression using the fact that \mathbf{W} is symmetrical, the theorem $(\mathbf{AB})^T = \mathbf{B}^T \mathbf{A}^T$ and introducing a constant α we get the value \mathbf{h} that updates the parameters in the direction of steepest descent

$$\mathbf{h}_{GD} = \alpha \mathbf{J}^T \mathbf{W} (\mathbf{y} - \hat{\mathbf{y}}).$$

α is chosen and decides how fast the algorithm is moving in the direction of steepest descent. Setting α too high you risk overshooting the minimum and each iteration the algorithm will oscillate around the minimum. Choosing an α too small might result in the algorithm becoming stuck because of too small updates slowing down the algorithm and possible causing it to never reach the minimum.

GN is an expansion of the Newton's method (Cavazzuti, 2013, p.85). Newton's method assumes that the RSS function is quadratic near the minimum. This is reasonable because if the RSS function has a minimum, the value will drop to the minimum and then increase when passing the minimum like a quadratic function. The quadratic function around the minimum is Taylor expanded and becomes

$$\hat{\mathbf{y}}(\mathbf{p} + \mathbf{h}) \approx \hat{\mathbf{y}} + \mathbf{J}\mathbf{h}.$$

Inserting the approximation for $\hat{\mathbf{y}}$ into the RSS in equation 1-16, we get

$$\mathbf{y}^T \mathbf{W} \mathbf{y} - 2\mathbf{y}^T \mathbf{W}(\hat{\mathbf{y}} + \mathbf{J}\mathbf{h}) + (\hat{\mathbf{y}} + \mathbf{J}\mathbf{h})^T \mathbf{W}(\hat{\mathbf{y}} + \mathbf{J}\mathbf{h}).$$

Again, using the second binomial formula and the theorem $(\mathbf{AB})^T = \mathbf{B}^T \mathbf{A}^T$ we get

$$\mathbf{y}^T \mathbf{W} \mathbf{y} + \hat{\mathbf{y}}^T \mathbf{W} \hat{\mathbf{y}} - 2\mathbf{y}^T \mathbf{W} \hat{\mathbf{y}} - 2(\mathbf{y} - \hat{\mathbf{y}})^T \mathbf{W} \mathbf{J} \mathbf{h} + \mathbf{h}^T \mathbf{J}^T \mathbf{W} \mathbf{J} \mathbf{h}. \quad 1-17$$

Newton's method differs compared to GD, because it also accounts for the curvature of the RSS function. We therefore differentiate equation 1-17 w.r.t. \mathbf{h} to find the one that minimizes RSS. As mentioned, \mathbf{J} is the Jacobian and differentiating \mathbf{J} w.r.t. \mathbf{h} we get a matrix called the Hessian matrix. It can be written as the sum (Chen, 2011)

$$\sum_{i=0}^m \left(\frac{\partial \text{RSS}_i}{\partial p_j} \frac{\partial \text{RSS}_i}{\partial h_k} + \hat{y}_i \frac{\partial^2 \text{RSS}_i}{\partial p_j \partial h_k} \right) 1/\sigma_{y,i}.$$

In the GN method the second derivative term is assumed to be 0. Going back to matrix notation the expression becomes

$$\mathbf{J}^T \mathbf{W} \mathbf{J}. \quad 1-18$$

This results in the derivative becoming

$$-2(\mathbf{y} - \hat{\mathbf{y}})^T \mathbf{W} \mathbf{J} + 2\mathbf{h}^T \mathbf{J}^T \mathbf{W} \mathbf{J}. \quad 1-19$$

Setting equation 1-19 equal to 0 and rearranging using the same theorem from before we get

$$\mathbf{J}^T \mathbf{W} \mathbf{J} \mathbf{h}_{GN} = \mathbf{J}^T \mathbf{W}(\mathbf{y} - \hat{\mathbf{y}})$$

The **LM** method introduces a dampening link λ , which is scaled according to the diagonal elements of the Hessian matrix

$$(J^T W J + \lambda \operatorname{diag}(J^T W J)) h_{LM} = J^T W (\mathbf{y} - \hat{\mathbf{y}}).$$

The dampening factor punishes updated parameters that does not contribute to reduced RSS by increasing λ , and encourage updated parameters that reduce RSS by decreasing λ . The result is a method that acts as GD far from the minimum but becomes GN when approaching the minimum.

1.6.2 Poisson Regression

Poisson regression is a way of analyzing and predicting discrete count data. It is like linear regression (section 1.6.1) in that it tries to fit a model to data, but the method is different.

In Poisson regression we assume that the response variable in $\mathbf{y}^T = [y_0, y_1, \dots, y_m]$ is Poisson distributed. That is, it follows the probability mass function (PMF) (Cameron & Trivedi, 2013a, p.3)

$$P(y_i) = \frac{e^{-\lambda} \lambda^{y_i}}{y_i!},$$

giving the probability of getting y_i counts when mean and variance are both equal to λ . Poisson regression treats each count as an independent Poisson random variable, where it estimates λ_i for every y_i using the linear model with a set of $m \times n$ explanatory variables in \mathbf{X} and estimates $n \times 1$ coefficients in $\boldsymbol{\beta}$ (Cameron & Trivedi, 2013a, p.10)

$$\operatorname{E}[y_i | \mathbf{x}_i] = \lambda_i = \mathbf{x}_i^T \boldsymbol{\beta} = \sum_{j=0}^n x_{j,i} \beta_{j,i}, \quad 1-20$$

where $x_{i,j}$ is the j^{th} of a total of n explanatory variables for the i^{th} datapoint. However, a problem arises if the combination of explanatory variables and coefficients sums to a negative number. The mean counts cannot be negative; thus, we instead consider the natural log of λ_i

$$\log \lambda_i = \sum_{j=0}^n x_{j,i} \beta_{j,i} \rightarrow \lambda_i = \exp \sum_{j=0}^n x_{j,i} \beta_{j,i} = e^{\mathbf{x}_i^T \boldsymbol{\beta}}. \quad 1-21$$

The estimation of coefficients is done using the maximum likelihood estimator (MLE). The likelihood function describes the joint probability of observing all the data \mathbf{y} given a set of parameters $\boldsymbol{\beta}$ represented by

$$\mathcal{L}(\boldsymbol{\beta}) = \prod_{j=0}^n P(y_i|\boldsymbol{\beta}) = \prod_{j=0}^n \frac{\exp(-\lambda_i) \lambda_i^{y_i}}{y_i!},$$

now inserting the expression for $\log \lambda_i$ from equation 1-22 we get

$$\prod_{j=0}^n \frac{\exp(-e^{x_i^T \boldsymbol{\beta}}) e^{x_i^T \boldsymbol{\beta}^{y_i}}}{y_i!}$$

It is important to note that the datapoints are assumed independent, which allows us to use that $P(A \cap B) = P(A) \cdot P(B)$. Using the log-likelihood allows us to compute the sum instead (Cameron & Trivedi, 2013b, p.23)

$$\log \mathcal{L}(\boldsymbol{\beta}) = \sum_{j=0}^n -e^{x_i^T \boldsymbol{\beta}} + y_i x_i^T \boldsymbol{\beta} - \log y_i! .$$

Differentiating w.r.t. $\boldsymbol{\beta}$ and setting the expression equal to zero we get

$$\sum_{j=0}^n (y_i - e^{x_i^T \boldsymbol{\beta}}) x_i = 0 .$$

Thus, we want to minimize the difference between y_i and $e^{x_i^T \boldsymbol{\beta}}$ to maximize the log-likelihood $\log \mathcal{L}(\boldsymbol{\beta})$. The equation does not have a closed form solution and an iterative method is needed to find the best fitting set of parameters $\hat{\boldsymbol{\beta}}$. Methods such as the ones described in 1.6.1 can be used.

1.6.3 Confidence interval

A confidence interval for e.g., 95% confidence claims that the true population mean will be within the limits of the confidence interval 95% of the times a sample mean is measured (James et al., 2013, p.66). For a general mean value \bar{X} with unknown population mean, the confidence interval is found using the formula

$$\bar{X} \pm t_{crit}\sigma_{\bar{X}} = t_{crit}\frac{\sigma}{\sqrt{n}},$$

if the t distribution has a mean of μ , then t_{crit} is the number of standard deviations \pm from μ that encapsulates the allowed variations of μ . $\sigma_{\bar{X}}$ is the standard deviation of the mean \bar{X} , and is found by s/\sqrt{n} where s is the standard deviation of the sample and n is the number of measurements.

1.7 Radiobiology

Note: There are many biology terms mentioned here that are not explained in this section, but they have been briefly explained in Abbreviations and explanations. These terms will be highlighted in ***bold italics***.

Cells are the building blocks of all living things. Animals are made from eukaryotic cells, which contain a nucleus. The purpose of a cell is converting consumed nutrients into energy needed to perform a task. Such tasks might be to provide structure (bone cells, muscle cells), sensory signaling (nerve cells) or transportation (blood cells). These cells are highly specialized and stem from an unspecialized cell (stem cell) that have finished their chain of cell divisions and differentiation. The process of cell division (proliferation) is sensitive and damaged DNA (deoxyribose nucleic acid) might lead to cell death or cancer if not repaired.

1.7.1 DNA basics

DNA or deoxyribose nucleic acid contains the complete genetic information needed to produce necessary proteins. DNA is made up of two antiparallel strands (3 to 5 and 5 to 3, see further down for explanation) with nitrogenous base pairs connecting the strands (Figure 1-15). The strands consist of nucleotides, which may be separated into a sugar-phosphate backbone and the DNA base (*Nucleotide / Biochemistry / Britannica*, 2008). There are five bases: Adenine, Guanine, Cytosine, Thymine and Uracil. The first four are in our DNA, and Uracil replaces Thymine in the **mRNA**. The bases are divided into two categories: Adenine and Guanine are known as pyrimidines, while Cytosine, Thymine and Uracil are purines. If three adjacent bases (not base pairs) code for an ***amino acid***, the triplet is known as a codon. Gene sequences, which includes codons are called exons, but if they do not include codons, they are called introns. The bases form hydrogen bonds across the strands, but only with dedicated “partners”. Because of its chemical structure, adenine only binds to thymine (or Uracil during ***DNA transcription***),

while guanine only binds to cytosine (Mason et al., 2020, p.48). The hydrogen bonds are the first of two bonds between nucleotides. The second bond is the phosphodiester bonds between each sugar-phosphate.

In Figure 1-16 the structure of a nucleotide can be seen. The carbon atoms in the deoxyribose molecules are marked with numbers 1-5 (Mason et al., 2020, p.47). When a new nucleotide is bound to the existing nucleotide, they can only be connected to the 3 carbon because they are able to chemically interact with the phosphate group of the incoming nucleotide to create the phosphodiester bond (Mason et al., 2020, p.284).

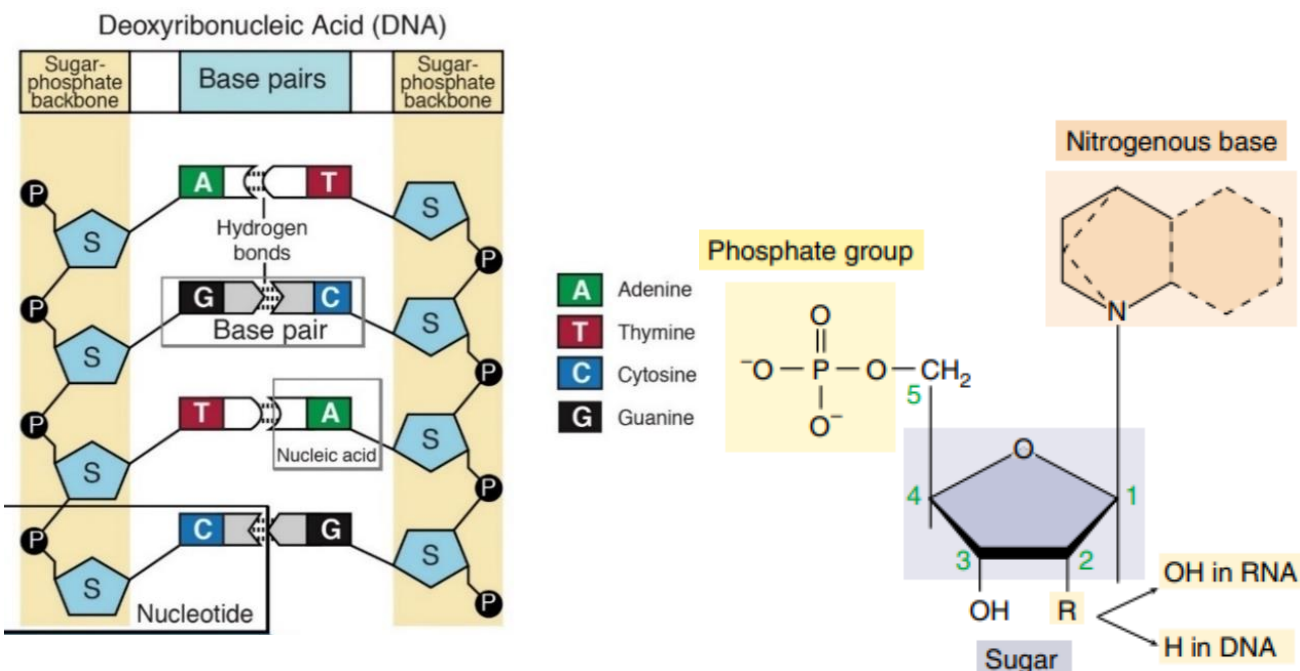


Figure 1-16. Schematic of DNA double strand (Nucleotide, n.d.). Bases form base pairs and nucleotides form phosphodiester bonds with neighboring nucleotides.

Figure 1-15. Three molecules making up a nucleotide, sugar, a phosphate group and the base. The positions of each carbon in the sugar molecule are marked by a number (Mason et al., 2020, p.47).

The DNA strands are twirled around its own axis to form a DNA double strand helix. DNA is further coiled around proteins known as histones to form nucleosomes. The nucleosomes are folded to produce fibers called chromatin (Figure 1-17). When the cell is prepared for cell division, the chromatin is tightly coiled into a supercoil (Mason et al., 2020, p.210). However, during interphase (non-dividing cell cycle phase), the DNA needs to be accessible for DNA replication and **DNA transcription**. Therefore, the chromatin is a dynamic structure that condense and decondense according to which phase the cell is in (Alberts et al., 2014, p.193). When chromatin is folded it forms a chromosome. The chromosome has a centromere which allows for linkage between chromosomes to generate chromosome pairs. When chromosomes are connected, we refer to the individual chromosomes as a sister chromatids (*Centromere / Biology / Britannica*, 2012).

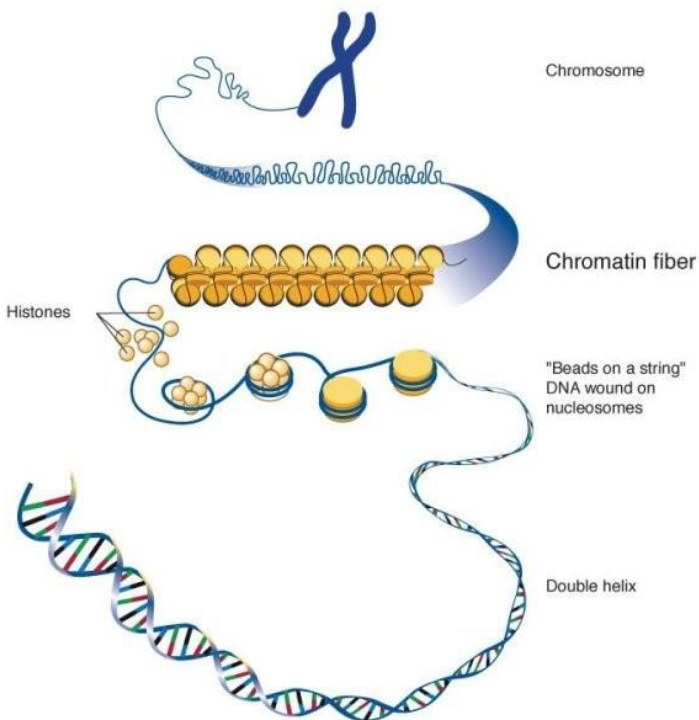


Figure 1-17. Chromosome structure (The Structure and Function of Chromatin, 2017). DNA strands are twirled and bound around proteins stacked to generate fibers that are condensed to make a Chromosome.

1.7.2 Cell Cycle and Checkpoint

The cell cycle consists of four phases: G1, S, G2 and M (Figure 1-18). G1 and G2 are the gap phases where cell growth occurs. During S-phase DNA is replicated. This happens by a series of initiator proteins that open the DNA double helix, creating a replication fork (see Figure 1-19)

(Mason et al., 2020, p.293). An *enzyme* known as helicase separates the strands by disrupting the hydrogen bonds between the base pairs (Matson et al., 1994). Two DNA-polymerase enzymes are recruited to the DNA strands, with the purpose of generating two new complementary DNA strands. DNA-polymerase is only able to continue an existing complementary strand, therefore **RNA-primers** are created as a starting point for the DNA-polymerase (Mason et al., 2020, p.293). As mentioned in 1.7.1 new nucleotides can only attach to the position 3 carbon. Since the two strands are antiparallel, the 5-3 strand is straightforward to replicate because the DNA-polymerase moves in the same direction as the helicase. This strand is known as the leading strand. But the complementary 3-5 strand must be replicated away from the replication fork. Therefore, the DNA-polymerase must jump back and forth, creating smaller bits of a DNA-strands called Okazaki fragments. Then the RNA primers are removed and the bits are glued together by an enzyme called ligase (Mason et al., 2020, p.292). This strand is known as the lagging strand.

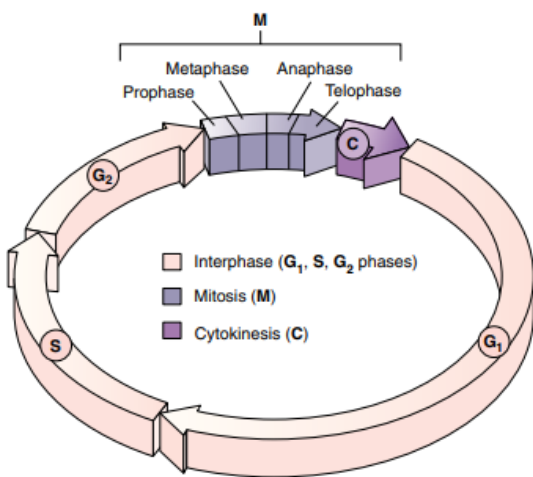


Figure 1-18. Cell cycle schematic, G₁, S and G₂ phase is known as interphase, where the cell grows and replicates its organelles to prepare for cell division in Mitosis. In Mitosis the cell separates the chromosomes before the cytoplasm is separated, and we are left with two identical daughter cells (Mason et al., 2020, p.212).

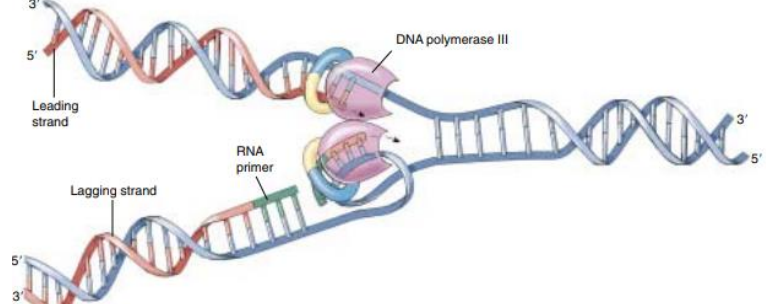


Figure 1-19. DNA replication schematic, where DNA is opened, and two complementary strands are created. Nucleotides only binds on 3'-OH group, which affects how the DNA-polymerase connects new nucleotides, leading to a leading strand and a lagging strand (Mason et al., 2020)

M-phase is mitosis and the process of separating the replicated chromosomes before the cytoplasm (medium surrounding the organelles of the cell) is separated to produce two identical daughter cells. This process is divided into **prophase**, where the chromosomes are condensed,

and the mitotic spindle apparatus is assembled. **Metaphase** is where the centromeres of the chromosomes align at the center of the cell. During **Anaphase**, centromeres separate and move towards each pole of the cell, splitting the chromosomes. Finally in **Telophase**, the spindle disassembles, and the daughter cells form individual nuclei (Mason et al., 2020, p.214-216). If the cell's external environment is not favorable the cell might enter a resting phase known as G0, where it is still able to perform its tasks, but where it does not progress to cell division (Mason et al., 2020, p.212).

A cell's progression through the cell cycle is highly regulated. The G1, G2, and M-checkpoint have the task of controlling that the associated phase has had time to complete its tasks (Alberts et al., 2014, p.967). If the cells were to enter cytokinesis before completely separating the chromosomes, or if the DNA were not replicated correctly before entering mitosis, it may have disastrous consequences.

One very important enzyme in cell cycle progression is the cyclin dependent kinase (CDK). CDKs are inactivated unless bound to another protein called cyclin. There are three main categories of cyclins: G1/S, S, and M-cyclins. Their levels rise and fall as the individual cyclins are needed (Mason et al., 2020, p.219). A CDK bound to a cyclin is called a CDK complex. For a cell to pass the G1-checkpoint and enter S-phase, there is a threshold of external and internal signaling levels that needs to be passed. A complex system of positive feedback loops drive the cell over a point called the restriction point (Pardee, 1974). For instance, when a sufficient amount of CDKs are activated, they will **phosphorylate** a protein called Rb (retinoblastoma). If the Rb protein receives two phosphors it will release itself from a protein called E2F, which in turn induce transcription of new cyclins (Alberts et al., 2014, p.1012-1013). E2F also targets a protein on the SCF protein complex, which is important in degradation of the p27 protein, a protein that binds to a CDK complex inhibiting phosphorylation (Yung et al., 2007).

The S-cyclin activated CDKs phosphorylate proteins, such as activation of DNA helicases responsible for activation of the DNA replication process. The S-CDK is also responsible for the

construction of a prereplicative complex (preRC), which ensures that the DNA is only replicated once per cycle (Alberts et al., 2014, p.974).

The G2-checkpoint makes sure that necessary proteins for mitosis are present and that the DNA, as well as all the organelles, has been correctly replicated in S-phase and G2-phase. Both G1- and G2-checkpoints can arrest the cell cycle if DNA-damage is spotted (Studzinski & Danilenko, 2005).

The M-checkpoint is the final checkpoint, and ensures correct separation of chromosomes before cytokinesis (Studzinski & Danilenko, 2005). Then, another set of positive feedback loops kicks in. A protein called Cdc25 activates M-CDK complexes, which became inactivated by another protein called wee1. These M-CDK complexes begin to inhibit the Wee1 protein, while also inducing important mitotic events (Alberts et al., 2014, p.978).

All checkpoints are controlled by genes that either promote or demote the cell cycle. Cell cycle promoting genes are called proto-oncogenes. If mutated, they become oncogenes and might lead to uncontrolled cell division and cancer (Weinstein, 2002). In the event of oncogene activation, tumor suppressors kick in. Tumor suppressors code for proteins responsible for inhibiting the CDK complexes from operating. Tumor suppressors are also responsible for cell cycle arrest when DNA-damages are detected (Alberts et al., 2014, p.1015). If DNA-damage is unrepairable the cell may go through *apoptosis* (Jeffers et al., 2003).

1.7.3 DNA damage and repair

Ionizing radiation damage the DNA in two ways: Either directly depositing its energy in a **biomolecule**, or by ionizing molecules surrounding the biomolecules, creating highly reactive radicals that oxidize the biomolecules (Radiation Biology: A Handbook for Teachers and Students, 2010). DNA is also damaged without being exposed to ionizing radiation, especially during DNA replication and building of Okazaki fragments (1.7.2). About one mistake is made for every 10^{10} nucleotide (Alberts et al., 2014, p.242). The mistakes might also be spontaneous such as deamination (cytosine become uracil) and depurination (loss of either Adenine or Guanine) (Cooper, 2000a). Even UV-light might cause adjacent pyrimidines to become glued together creating a pyrimidine dimer (Mason et al., 2020, p.364).

The mentioned damages are discontinuities in the DNA strands and might be classified as either single strand breaks (SSB) or double strand breaks (DSB). A single strand break only occurs in one DNA strand. If complete cleavage of two opposite strands occur with only a few base pairs of separation the damage is called a double strand break (Hall & Giaccia, 2012, p.12).

Damages might also be classified as sublethal, potentially lethal and lethal. Sublethal damages are not lethal, potentially lethal damages are lethal unless repaired and lethal damages are of course beyond repair.

The cell has many DNA repair pathways, it can remove deaminated bases through base excision or remove whole nucleotides in a pyrimidine dimer with nucleotide excision repair (Hall & Giaccia, 2012, p.16). However, for more complicated damages like DSBs, more intricate repair mechanisms are needed.

Nonhomologous end-joining (NHEJ) is a repair mechanism activated in G1. The DNA is yet to be replicated and no sister chromatid is available. The solution is to simply reattach the strands as seen in Figure 1-20. The result is loss of the damaged nucleotides, which might result in removing important protein coding exons (see 1.7.1) (Hall & Giaccia, 2012, p. 18).

Homologous recombination (HR) is another repair mechanism, but it is activated in late S/G2 when a sister chromatid is available as a template. A repair protein complex searches for a DNA segment on the unharmed sister chromatid, which is similar or identical to the damaged chromatid. A search for homology is performed by invading an unharmed strand and sampling base sequences. When homology is found DNA-polymerase is recruited to extend the damaged strand. The unharmed strand is released and the newly extended strand is used as a template to fix the other damaged strand (Alberts et al., 2014, p.278-279). Both the NHEJ and HR are illustrated in Figure 1-20 . Compared to NHEJ, HR is less efficient, but no DNA is lost during HR and DNA is accurately restored (Z. Mao et al., 2008). This underlines the importance of the G2 checkpoint.

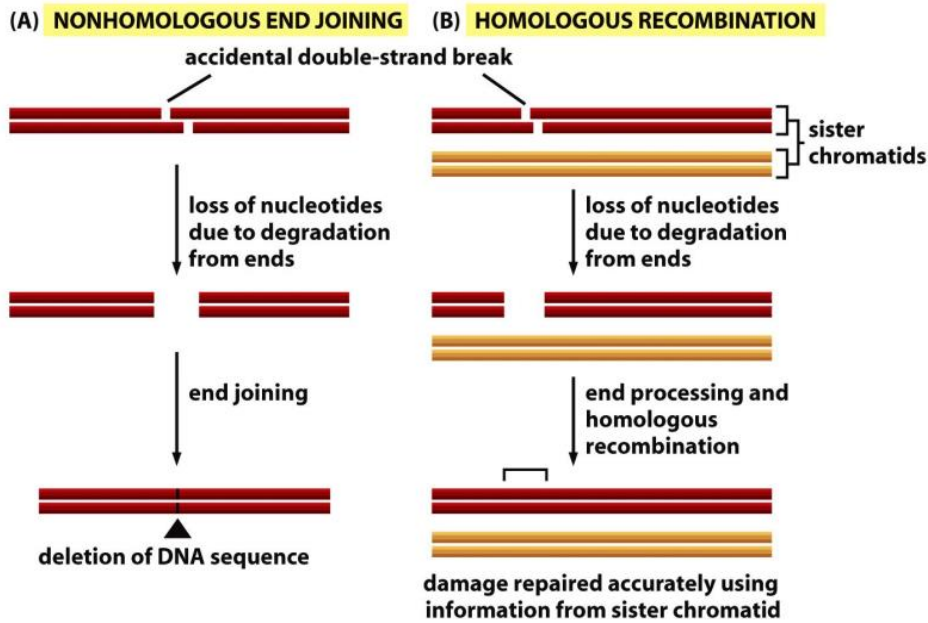


Figure 1-20. (A) Nonhomologous end-joining is DNA repair happening in the G1-phase of the cell cycle before DNA is replicated. The strands are connected, but the nucleotides that existed on the strand before damage occurred, are gone. (B) Homologous Recombination during late G2/S phase where sister chromatid is available after DNA replication and completely restores the broken DNA (Alberts et al., 2014, p.275).

Failure of repairing DNA damage might have severe consequences. An unbound base caused by a DSB easily forms new hydrogen bonds with unbound bases elsewhere on the strand where a DSB or SSB have occurred (Hall & Giaccia, 2012, p.25). If enough DSBs are left unrepaired, or the cell is not arrested or the damage occurs late in the cell cycle, they can cause severe abnormalities known as chromosomal aberrations (Grote & Revell, 1972). Lethal chromosomal aberrations result in the two sister chromatids being connected by so-called “sticky” ends. Because the centromere is the only point where chromatid sisters can be separated, it leads to a situation where the “sticky” end connections are left inseparable during mitosis causing mitotic cell death (Hall & Giaccia, 2012, p.26). Moreover, chromosomal aberrations may be non-lethal. Examples are symmetrical translocations and small deletions. Translocation is when a piece of chromosome breaks and reattaches to another chromosome, while deletion is removal of a piece of chromosome without reattaching. These aberrations are non-lethal because the chromosomes are able to separate successfully during mitosis (Hall & Giaccia, 2012, p.26-32). But the damages might lead to activation of oncogenes (Nambiar et al., 2008) or inactivation of a tumor.

suppressor gene (X. Mao et al., 2011), generating cells that avoid the cell cycle checkpoints and might evolve into cancer cells.

1.7.4 Cell Survival Curves

A cell survival curve is of key importance in radiobiology and explains the relationship between cell survival S and radiation dose D. If there is sufficient space and nutrients, a cancer cell will divide indefinitely. The cancer cell is therefore defined as dead if it has completely lost its ability to divide and form colonies; thereby the name clonogenic survival (Hall & Giaccia, 2012, p.35). Cancer cells' response to irradiation is often studied by in vitro (in a cell dish or cell flask) cell survival experiments. The cells are seeded in monolayers at the bottom of a cell flask with a medium containing all necessary nutrients. The cells are kept in an incubator with ideal temperature and are counted after a specified number of days to allow for sufficient growth time. The cells in a non-irradiated cell flask have a certain probability of forming colonies, which is affected by the external environment as well as cell division errors (Hall & Giaccia, 2012, p.36). This efficiency is called the plating efficiency (PE) and is represented by the formula

$$PE = \frac{\# \text{ colonies counted control flask}}{\# \text{ cells seeded}}. \quad 1-22$$

The ideal PE is 100% so that all seeded cells from colonies, but because of suboptimal growth medium, handling, or other external factors, optimal PE is around 50 % (personal communication, prof. Nina Edin). PE is used as a normalization factor to accurately compare different experiments with different conditions. The survival fraction (SF) of an irradiated cell dish is found using the formula

$$SF = \frac{\# \text{ colonies counted irradiated flask}}{\# \text{ cells seeded} \cdot PE}. \quad 1-23$$

In Figure 1-21 we see a typical cell survival curve, with the natural log of survival as a function of radiation dose. However, it is worth noting that each irradiated dish's survival constitutes a point on the curve, and the curve is a result of interpolation. The interpolation is decided by a model known as the linear-quadratic (LQ) model, which is discussed in 1.7.5.

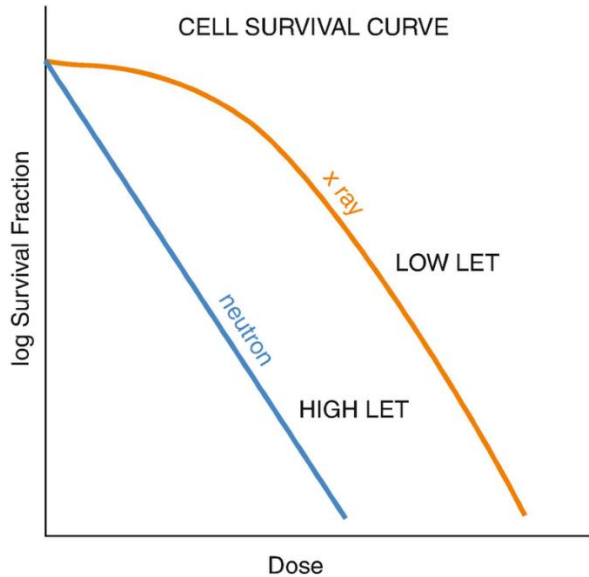


Figure 1-21. Typical cell survival curve with low and high LET (see 1.1.2) which is typically expressed in the natural log of survival (Giridhar & Rath, 2020).

1.7.5 LQ-model

This section is based on Chadwick & Leenhouts: A molecular theory of cell survival

The LQ-model is a mathematical model proposed to fit the shape of the cell survival curve as a function of increasing dose. From Figure 1-21 we see that the survival curve becomes less linear as LET (see 1.1.2) decreases. The increased curvature of the low LET region is known as the “shoulder” of the survival curve. The formula explaining this shape is

$$S = e^{-(\alpha D + \beta D^2)}, \quad 1-24$$

where D is dose. α and β represents radiosensitivity of the cell (McMahon, 2018). Several interpretations of the biological foundation for the LQ-model model have been proposed (Denekamp & Daşu, 1999; Kellerer & Rossi, 1971). The most commonly used is the derivation by Chadwick and Leenhouts, which assumes that there is a critical molecule crucial for a cell's ability to divide, and that this molecule is the DNA. It also assumes that DSB is the critical damage type, but that the cell has repair mechanisms that might repair the damage. It accounts for two different DSB events (breakage of chemical bonds in the DNA molecule).

1. One event causing one DSB
2. Two SSBs close enough in time and space to create one DSB

α represents mode 1, and β represents mode 2. In α and β we have the probability that the chemical bonds, are broken because of a received dose D and that the breaks induce lethal damage. This is derived as follows

1. $1 - e^{-kD\Delta}$
2. $1 - e^{-kD(1-\Delta)}$

where k is the probability per bond per unit dose that the bond is broken. Δ is the proportion of dose that breaks the bonds with mode 1, and $(1 - \Delta)$ is the proportion of dose for mode 2. Chadwick & Leenhouts showed that the mean number of DSBs from mode 1 was

$$A[1 - e^{-k\Delta D}],$$

where A is the number of bonds on the DNA double helix, where mode 1 DSBs occur.

A first order Taylor approximation around 0 for $e^{-k\Delta D}$ gives

$$A \cdot [1 - (1 - k\Delta D)] = Ak\Delta D$$

For mode 2 they showed that mean number of DSBs was

$$B[1 - e^{-k(1-\Delta)D}]^2,$$

where B is number of SSBs not repaired on both strands, that are also close enough in time and space to constitute a DSB. Doing the same Taylor expansion gives

$$B \cdot [1 - (1 - k(1 - \Delta)D)^2] = Bk(1 - \Delta)D^2.$$

Combining the number of DSBs from each mode and multiplying with the probability of the DSBs not being repaired f , we get

$$f \cdot [Ak\Delta D + Bk(1 - \Delta)D^2].$$

From here they introduced a proportionality constant to relate number of DSBs to cell death and assumed Poisson distribution (1.6.2) to achieve probability of cell survival per dose. This results in the equation 1-24, and shows why we have a linear and a quadratic link in the LQ-model. This is reflected in the curves we see in Figure 1-21, where the high LET radiation has a denser energy deposition, creating more mode 1 DSBs. And for low LET there is a shoulder caused by accumulation of SSBs for higher doses creating more mode 2 DSBs.

One should still be mindful about when to use the model. Studies have shown that the model can fit poorly for very small doses (hyper radiosensitivity Puck & Marcus, 1956) or higher doses (overestimated cell killing, Wang et al., 2010). The α/β ratio is a measurement of sensitivity to fractionation, where you find the dose of equal contribution between α and β (Figure 1-22). The ratio indicates whether it is reasonable to split the dose into fractions to allow time for repair, thereby extending the shoulder of the survival curve and increasing survival (van Leeuwen et al., 2018). The ratio is found by setting the contribution of α and β equal(Hall & Giaccia, 2012, p.39)

$$\alpha D = \beta D^2 \rightarrow D = \frac{\alpha}{\beta}.$$

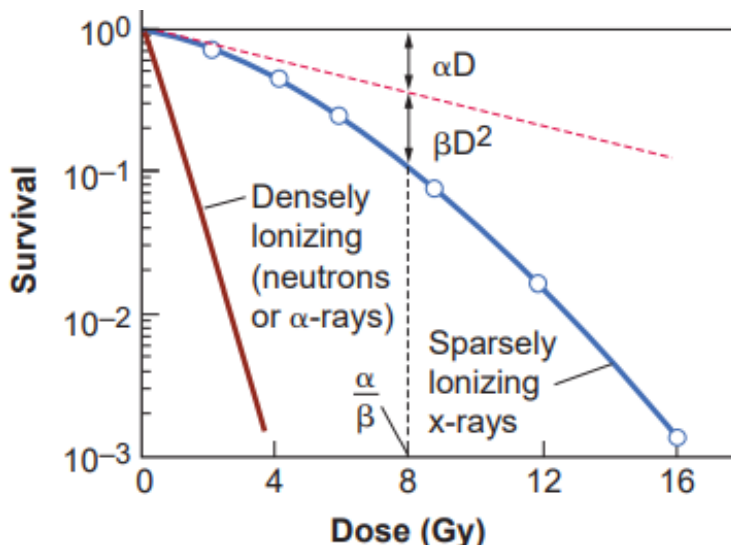


Figure 1-22. Typical cell survival curves for low (blue) and high (red) LET, with α/β ratio illustrated (Hall & Giaccia, 2012,p.39).

1.7.6 Radiation Induced Bystander Effect

Cells are as mentioned directly or indirectly damaged by irradiation (1.7.3). However, it has been showed that non-irradiated cells might exhibit the same biological endpoints (e.g., apoptosis, generation of micronuclei or DNA strand breaks) as irradiated cells. One study showed that 30% of analyzed cells expressed an increase in sister chromatid exchange (*SCE*), even though only 1% of cells were irradiated (Nagasawa & Little, 1992). This phenomenon is called the radiation induced bystander effects (RIBE). The hypothesis is that irradiated cells signal to non-irradiated cells, either by intracellular communication trough protein channels (Gap junctions) between cells (Mesnil et al., 1996), or intercellular communication by excreting soluble factors into the surrounding medium (Luce et al., 2009). Although the existence of RIBEs is indisputable, the characteristics of the biological parameters constituting an RIBE is not well defined (Blyth & Sykes, 2011).

It has been shown that a multitude of pathways are involved in RIBEs, such as *p53* (Koturbash et al., 2008), *ATM* (Ataxia telangiectasia mutated protein) (Ghosh et al., 2015), reactive oxygen species (*ROSs*) (Zhang et al., 2016) and various *cytokines* (Hu et al., 2014; Shareef et al., 2007). The bystander effect can either increase lethality or increase radio resistance. Mothersill & Seymour showed decreased clonogenic survival (see 1.7.4) when medium from irradiated cells were transferred to non-irradiated cells. However, Iyer & Lehnert showed increased clonogenic survival of cells that were irradiated after medium transfer. The observed effect appears to be highly dependent on radiation quality (e.g., protons or photons) dose, and which cell line is studied. A review from 2004 on recent developments and implications of bystander effect concluded: For low-LET, low dose irradiation the effects were predominantly protective, but for high-LET it was less clear as both protective and detrimental effects were observed (Mitchel, 2004). Soleymanifard & Bahreyni found that QU-DB cancer cells had increased production of micronuclei (*MN*), while number of MN for MRC5 fibroblasts remained constant. Better understanding of the biological mechanisms behind these results is important and has the potential of expanding how the effect can be utilized better in the future.

1.7.7 Spatially Fractionated Radiation Therapy

Spatially fractionated radiation therapy (SFRT or GRID therapy) aims to achieve a non-uniform dose distribution as shown in Figure 1-23. It is in stark contrast to traditional radiotherapy where dose uniformity in the target is desirable. A problem occurs when an organ at risk (OAR) is positioned within the target that receives an equally large dose. Should the dose-planer focus on dose conformity or OAR sparing. By spatially fractionating the radiation field and generating areas of low, one might take advantage of the healthy cells general superior repair capacities compared to cancer cells (Murphy et al., 2020). Traditionally a GRID block was used to create high (peak) and low (valley) dose areas (Billena & Khan, 2019). GRID therapy arose from the need of treating deep seated or bulky tumors (W. Yan et al., 2019) without excessive skin toxicity. The external beam therapy (EBT) machines of the early 20th century were typically X-ray tubes (1.2.1), and could not create photon beams with energies surpassing some hundred kV (Gianfaldoni et al., 2017). Therefore, few photons penetrated deep enough beyond the skin to reach the tumor. A GRID block was necessary to increase the dose but keep skin toxicity at a tolerable level. When MV photons were introduced with the linear accelerator (**LINAC**) and photon ranges increased, the need for GRID decreased (W. Yan et al., 2019).

Today there are many ways to apply SFRT. Linear accelerators have preinstalled **MLCs** which can modulate the GRID pattern in a way the static GRID block cannot (Billena & Khan, 2019). 3D SFRT methods ('lattice' radiotherapy) have been developed, where the linear accelerator is rotated and the beam is modulated to create a sphere-like dose distribution (Wu et al., 2010).

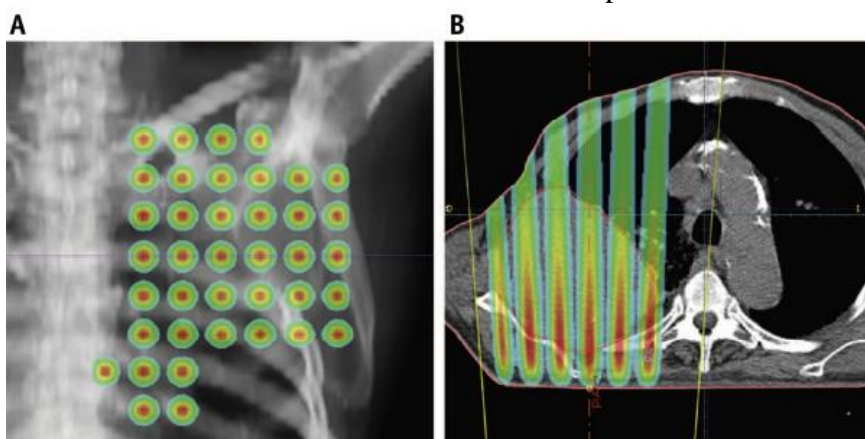


Figure 1-23. (A) An example of a dose plan for GRID therapy from anteroposterior view of the lung area. The GRID pattern is clearly visible with dose gradients out from the center of the circles. (B) A transversal view of dose plan. Here we also see gradients in dose into the patient as the radiation attenuates into the body (Billena & Khan, 2019)

From the 1990's to today, SFRT has primarily been used for palliative treatment (meant as pain relief rather than curing the patient) of bulky (larger than 8 cm) tumors (Mohiuddin et al., 1999). However, it has been showed *in vitro* that cells located in the low-dose valley region had overexpressed genes related to DNA-repair, cell cycle arrest and apoptosis (Mackonis et al., 2007; Suchowerska et al., 2005; Trainor et al., 2012). This study also showed that cells located in peak areas had increased survival, indicating that inter- and intracellular communication happen between the cells (1.7.6). There is also evidence of immune system activation by recruitment of T-cells (a type of white blood cell) (Kanagavelu et al., 2014). These results indicate the potential of SFRT as a curative treatment, either alone or in combination with immunotherapy or whole-tumor conventional radiotherapy.

2 Materials and Methods

The aim of this thesis is to model cell survival of *in vitro* GRID irradiated A549 cells. The steps taken towards this goal is represented in the pipeline in Figure 2-1. The cell experiments were performed by former MsC student Magnus Børsting (2.2). The cell flasks generated from these experiments were subsequently segmented by former PhD student Delmon Arous (section 2.3). Dosimetry for the cells was performed by calibrating the radiation field using an ionization

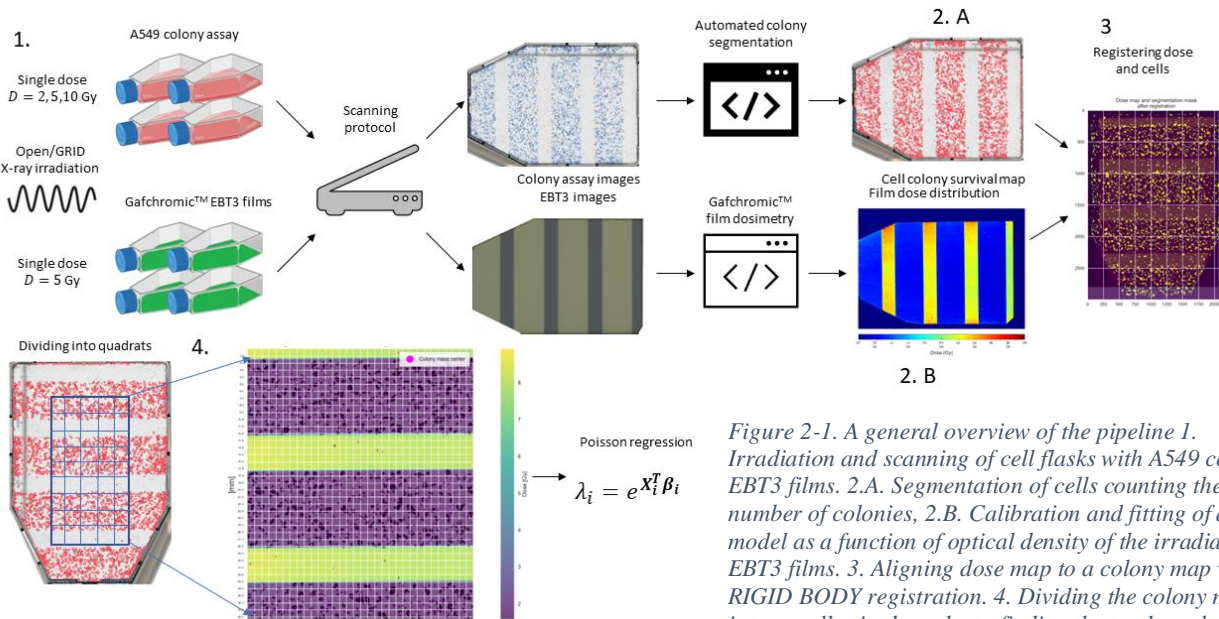


Figure 2-1. A general overview of the pipeline 1. Irradiation and scanning of cell flasks with A549 cells or EBT3 films. 2.A. Segmentation of cells counting the number of colonies, 2.B. Calibration and fitting of dose model as a function of optical density of the irradiated EBT3 films. 3. Aligning dose map to a colony map with RIGID BODY registration. 4. Dividing the colony maps into equally sized quadrats, finding the total number of colonies within each quadrat and the mean dose, before passing the values to a Poisson Regression model. 1. – 2B. was made by Delmon Arous.

chamber (2.1.1) then radiochromic films were calibrated to be placed inside the cell flask, generating 2D dose distributions (2.1.2). These dose maps could be aligned with colony maps generated from the segmented cell flasks and analyzed using 1D band analysis to generate survival profiles (section 2.4.2 not shown in Figure 2-1), before the 2D survival analysis method was introduced in section 2.4.3, where colony maps were divided into quadrats and predicted using Poisson regression.

Note: All programs generated for this thesis is stored in a GitHub repository called ProGrid_static. Data is given upon request.

https://github.com/jacobllie/ProGrid_static

2.1 Dosimetry

Establishing 2D survival analysis method for X-ray irradiated A549 cells through a GRID collimator, it was therefore necessary to develop methods for accurately measuring dose given to the cells. The dosimetry methodology was proposed by Bjørg Vårli Håland, 2020 in her master thesis but was further developed here. Gafchromic™ EBT3 film (Ashland, USA) was chosen as dosimeter for reasons to be elucidated in section 2.1.2. We needed to establish the films' dose response and generate a calibration curve. Therefore, X-ray dosimetry with an air-filled thimble ionization chamber (ion chamber) (FC65-G, IBA, Germany) was initially performed. Calibrations were made for both striped and dotted GRID configurations, respectively.

2.1.1 X-ray dosimetry

An X-ray beam was generated using a PMC 1000 X-ray unit (PANTAK, USA) operating at 10 mA and 220 kV. We used 0.7 mm Cu and 1.52 mm of Al for filtering. This is a standard in the X-ray lab at the Section for Biophysics and Medical physics, University of Oslo. The X-ray beam was enclosed in a lead cabinet, which we will refer to as the irradiation cabinet. The cabinet has a platform made from Perspex where cells can be placed at various distances from the X-ray source. A source to detector distance (SDD) of 60 cm was used to ensure the right beam divergence and sufficient intensity. The experimental setup can be seen in Figure 2-2. For irradiation, T25 cell flasks (Nunc, Denmark) were inserted into a cell flask holder made from polymethyl methacrylate (PMMA) holding four cell flasks in position A, B, C and D (Figure 2-3). The ionization chamber was placed inside a cell flask and measurements were performed in

all positions. Positioning of the cell flask holder on the Perspex platform inside the irradiation cabinet (Figure 2-3) was decided by field homogeneity measurements performed by Bjørg Vårli Håland. The protective cap of the ion chamber slightly lifts the sensitive volume above the bottom of the cell flask (see Figure 2-4)(i.e., closer to the radiation source), but the cells are seeded in monolayers at the bottom. It was therefore necessary to account for this height difference when prescribing a radiation dose. Because the X-ray intensity follows the inverse square law $I = \alpha/r^2$ (see 1.2.1), the ratio between intensity at the sensitive volume of the ion chamber I_1 and the intensity at the bottom of the cell flask I_2 is

$$\frac{I_1}{I_2} = \frac{r_2^2}{r_1^2}.$$

To find the distance from the cells to the X-ray source we needed the effective SDD, represented by the SDD, the thickness of the cell flask holder and the thickness of the cell flask bottom. Effective SDD the sensitive volume was the same except for the added radius of the protective cap. Measurements were made sing a caliper (FWP, Poland). Based on the smallest measurement possible of 0.01 cm, we assumed an uncertainty of 0.001 cm. The thickness of the cell flask holder and the cell flask bottom were found to be 1.500 ± 0.001 cm and 0.200 ± 0.001 cm, respectively. The diameter of the protective cap was 1.500 ± 0.001 cm, with a radius of 0.750 ± 0.001 cm. Uncertainty in I_1/I_2 was found with error propagation using equation 2-3 assuming negligible uncertainty in SDD

$$\frac{I_1}{I_2} = \frac{(60 - 1.5 - 0.2)^2}{(60 - 1.5 - 0.2 - 0.75)^2} = 1.02600 \pm 0.00002. \quad 2-1$$

We decided to neglect this uncertainty, to not further complicate the uncertainty analysis. Thus, we expect the intensity in the sensitive volume of the ion chamber to be 2.6% higher compared to the bottom of the cell flask, and we need to increase the dose accordingly when irradiating the EBT3 films and the cells.



Figure 2-2. An overlook of the experimental setup for X-ray irradiation. The cell flask holder is placed inside an in-house made irradiation cabinet.



Figure 2-3. A closer look at the experimental setup of X-ray irradiation. The ionization chamber is inserted into the cell flask, which is placed into the cell flask holder. Dose is measured in all four positions.

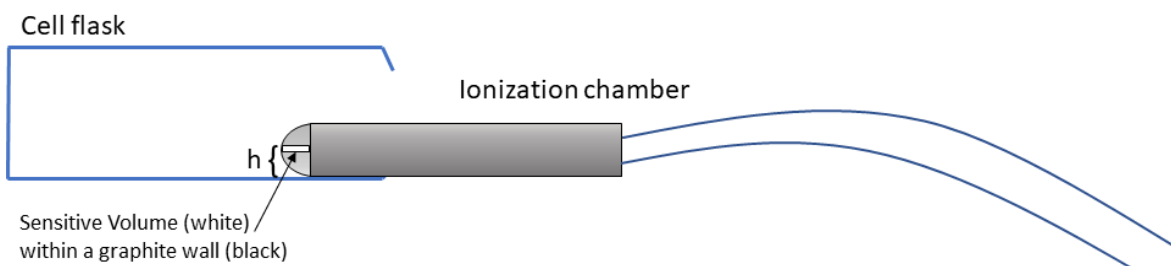


Figure 2-4. Ion chamber inserted into a T25 cell flask, that has been cut open. The sensitive volume is surrounded by a graphite wall within the protective cap, and we observe the height difference between the bottom of the cell flask and the cell flask. During experiments efforts were made to position the ionization chamber as flat as possible inside the cell flask. The figure is only for illustration purposes.

A max 4000 electrometer (Standard Imaging, USA) was used to measure the ionization current from the ion chamber. Converting the output of the electrometer, from nC in air to $Gy [J/kg]$ in water, was done using the formalism established by the International IAEA explained in 1.5.2

$$D_w = M_u N_k k_u p_u k_{TP} \left(\frac{\bar{\mu}}{\rho} \right)_{w,air} = C M_u N_k . \quad 2-2$$

D_w is dose to water, N_k [mGy/nC] is the calibration factor relating ion chamber output to dose in water and is given by the calibration lab (Norwegian Radiation and Nuclear Safety Authority). M_u is the output from the electrometer in nC, k_u is correction factor accounting for change in ion chamber response resulting in a shift in spectral distribution when moving from air to water. The correction factor is typically assumed to be 1, but it has been shown that k_u is dependent on the angular distribution of photons (P.Andreo et al., 1996, p.54-55). However, for our experiments we assumed this to have a negligible effect. p_u corrects for perturbation effects caused by the ion chamber displacing the water. $(\mu/\rho)_{w,air}$ is mass energy absorption coefficient (1.1.1.3) ratio between water and air averaged over the photon energy spectrum during reference conditions, which can be found in section 7.4. k_{TP} corrects for difference in air pressure and temperature conditions, compared to the reference conditions of the calibration lab. k_{TP} was found using the formula

$$k_{TP} = \frac{273.15 - T}{273.15 + T_0} \frac{P_0}{P} ,$$

where T and P are temperature and air pressure during calibration with an assumed negligible uncertainty. T_0 and P_0 are reference temperature and air pressure; $T_0 = 20^\circ C$, $P_0 = 1013 Pa$. Updated Correction factors and mass energy absorption coefficient rates were found in (Waldeleand et al., 2010) (Table 2-1).

Table 2-1. Calibration factor N_k with correction factors and mass energy absorption coefficient ratio. Two experiments were performed using dotted and striped GRID configurations with different temperature and air pressure conditions.

N_k [mGy/nC]	p_u	k_u	k_{TP} (stripes)	k_{TP} (dots)	$(\mu/\rho)_{air}^w$
43.77 ± 0.39	1.02	1	1.006745405	1.021463	1.075

The ionization chamber was irradiated 5, 10, 15, 20 and 60 seconds 3-4 times in each position. We wanted the dose prescribed to the calibration films to be analogue to doses received by the cells during cell GRID irradiation. Hence, doses of 0 (control), 0.1, 0.2, 0.5, 1, 2, 5, 10 Gy were chosen. For X-ray machines there is a delay from the machine starts producing a beam, to the desired dose-rate is reached. This time is called a ramp-up time (Heales et al., 1998). The ramp-up time is most prevalent for lower doses, where low exposure times are used. Therefore, a linear regression model (see 1.6.1) was found for 0.1, 0.2 and 0.5 Gy in each cell flask position using a function called *linregress* from the *scipy.v.1.6* library (Virtanen et al., 2020) in Python (v.3.8) (Guido van Rossum & and the Python development team, 2020). Then the estimated parameters were averaged to get a model independent of positioning in the cell flask holder. This would greatly decrease the duration of the experiment because we could irradiate in all positions at once. The resulting average regression model is

$$\widehat{D} = \bar{\beta}_0 + \bar{\beta}_1 t,$$

where $\bar{\beta}_0, \bar{\beta}_1$ are mean coefficients, t is exposure time and \widehat{D} is estimated dose. Rearranging the equation, we could find the time needed to achieve the desired low doses (0.1, 0.2, 0.5 Gy)

$$\hat{t} = \frac{D \cdot 1.026 - \bar{\beta}_0}{\bar{\beta}_1}$$

As mentioned in in 2.1.1 the dose needed to be multiplied with 1.026.

With a nonzero intercept, we could account for the ramp-up in beam production. *Linregress* returns the standard error of the estimated coefficients. Because we found the average model the combined standard error can be found with $\Delta\bar{\beta}_k = \sqrt{\sum_{i=0}^n \Delta\beta_{k,i}^2} / n$, where k is either 0 or 1, and n is the number of repeated measurements. The standard error of exposure time $\Delta\hat{t}$ was found using the formula for error propagation of the multivariate function $f(x_1, x_2 \dots x_n)$ with independent variables

$$df = \sqrt{\sum_1^n \left(\frac{\partial f}{\partial x_i} \Delta x_i \right)^2}.$$

2-3

The resulting error expression becomes

$$\Delta \bar{t} = \sqrt{\left(-\frac{1}{\bar{\beta}_1} \Delta \bar{\beta}_0\right)^2 + \left(-\frac{D \cdot 1.026 - \bar{\beta}_0}{\bar{\beta}_1^2} \Delta \bar{\beta}_1\right)^2}.$$

Because linear regression does not account for variability in the independent variable (see 1.6.1), $\Delta D = 0$. For doses above 0.5 Gy we assumed the effect of ramp-up time to be negligible. Therefore, we only made 60 second measurements to get dose rate (Gy/min) in all positions repeated 3-4 times. The measurements were averaged to obtain one common dose rate. We assumed the uncertainties were connected to N_k and M_u , respectively. With the error propagation we got

$$\Delta D_w = C \sqrt{(N_k \cdot \Delta M_u)^2 + (M_u \cdot \Delta N_k)^2}.$$

ΔM_u was found from the nC measurements by first averaging the repeated measurements of each position, then finding the standard errors between the averages of these by dividing it by $\sqrt{4}$ because we irradiated four positions. ΔN_k was reported as 0.39 mGy/nC by the calibration lab (*Norwegian Radiation and Nuclear Protection Authority*).

Finding time required for 1, 2, 5 and 10 Gy, we divided the dose with the dose rate. Again, using error propagation we got the uncertainty

$$\Delta t = \sqrt{\left(-\frac{D}{doserate^2} \cdot \Delta doserate\right)^2}.$$

2.1.2 Gafchromic™ film dosimetry

The protocol for Gafchromic™ film calibration follows the protocol established by (Devic et al., 2016).

The Gafchromic™ EBT3 films (lot #: 02122001) were chosen because they give a high spatial resolution, 2D dose distribution, and they can be neatly fitted to a cell flask. The near water equivalent property of the films offers comparative dose measurements to cells suspended in medium. The polymerization process (Figure 2-5) changes the color of the film post irradiation, and because of its low sensitivity to light, it is not necessary to develop the film (Niroomand-Rad et al., 1998).

EBT3 was chosen because of its symmetric chemical configuration (Figure 1-14), with a $125\ \mu m$ protective matt polymer layer on both side of a $26\ \mu m$ active layer. The implementation of a matte polyester protective layer instead of the smooth layer found in EBT2 removes the generation of the newton ring artefacts when scanning the films (GafChromic, n.d.). The films have a dose range of 0.1 – 10 Gy. Their optical density is known to change from exposure to UV light, temperature and humidity (Girard et al., 2012; Park et al., 2012), and the films were therefore handled using gloves in a room with dark curtains, and stored in a drawer at ambient temeprature. Because of the external influences in film response, it was important to have a set of control films, that received zero dose.

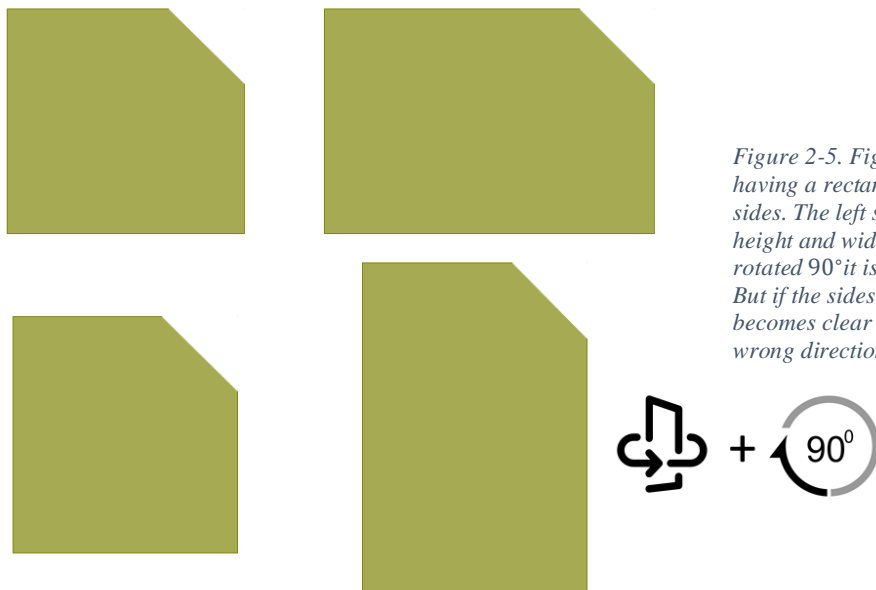


Figure 2-5. Figure illustrating importance of having a rectangle with two clearly different sides. The left side has a small difference in height and width. When the film is flipped and rotated 90°it is hard to observe the rotation. But if the sides are clearly different, then it becomes clear that the film is oriented in the wrong direction.

2.1.2.1 Film irradiation

As mentioned in section 1.5.3, we needed to establish a calibration curve before cell dose could be measured. Two calibrations were performed on two separate dates, one for striped and one for dotted GRID configurations. The method was mostly the same on both occasions, but the size of the calibration films was different. The films came in $20 \times 28 \text{ cm}^2$ sheets and were cut with a paper cutter that was sterilized before use. The calibration films for striped GRID were cut to a size of $4.3 \times 4.1 \text{ cm}^2$. It has been shown that the response of the films are sensitive to the direction of the film (Borca et al., 2013). A cut was therefore made on the top right corner of the longest side. The chosen size made it hard to detect which side was the longest. If the film was not handled properly and was flipped to its opposite side, one could not trust that the orientation was correct based on the cut. The scenario is illustrated in Figure 2-5. For dotted GRID, we increased the difference between width and height.

The T25 cell flasks were cut horizontally, and one film was placed inside each flask. The films were then irradiated in all positions simultaneously using the experimental setup shown in Figure 2-6, twice per dose point. This gave each dose eight calibration films.

A thin slab of 2 mm nylon6 (polymer) was placed on top of the films to act as a buildup material. The material filters low energy electrons and ensures CPE within the sensitive layer. Because the ionization chamber has a protective cap, the nylon6 slab will increase the similarity between the experimental setups of the film and ionization chamber irradiation, as well as cells suspended in medium. The films were irradiated with the exposure times found in 2.1.1.

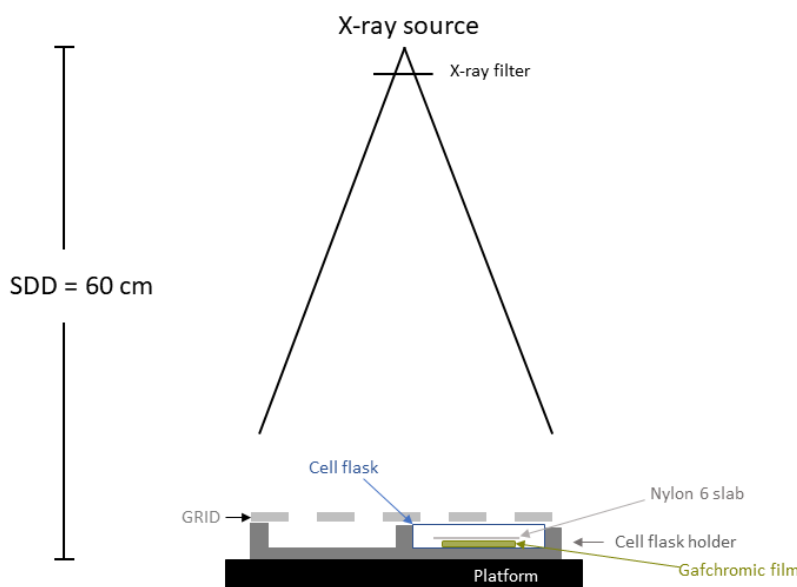


Figure 2-6. The experimental setup for GRID irradiation of Gafchromic™ films. For calibration and OPEN field irradiations in general, no GRID block was used.

A new set of films, referred to as the measurement films, were cut to match the shape of the bottom of the cell flasks. The films were given 5 Gy nominally. Then their response was mapped to the calibration curve. We irradiated films using the same experimental setup shown in Figure 2-6 On the first dosimetry experiment we irradiated using both GRID and OPEN field. The OPEN field films were used to evaluate the accuracy of our dosimetry. However, on the second dosimetry experiment, only GRID irradiations were made to save time. Four films were irradiated simultaneously in all four positions. This was repeated four times for OPEN field and GRID, giving 16 films per irradiation configuration. Because of poor cutting accuracy, the measurement films did not fit perfectly into the cell flask, causing them to have small variations in how they lay inside the flask. This resulted in slightly skewed response patterns after irradiations, assessed in section 2.1.2.3.

Two in-house with dimensions 150 x 130 x 5 mm³ tungsten metal collimators with striped or dotted grid patterns were constructed to be placed on top of the cell flasks laying in the cell flask holder (Figure 2-7). The stripes had 5 mm wide openings with 10 mm shielding in between. The diameter of the dots was 5 mm, with 12.5 mm shielding between. The collimator generates high and low dose areas called peaks and valleys. The high atomic number of tungsten (see 1.2.1) makes the material a great photon absorber. It is well known that collimating an X-ray beam results in increased scattering (Philip Mayes et al., 2007, p.377). The high density of tungsten allows for a thinner design, thereby reducing the scattering allowed within the openings of the GRID.

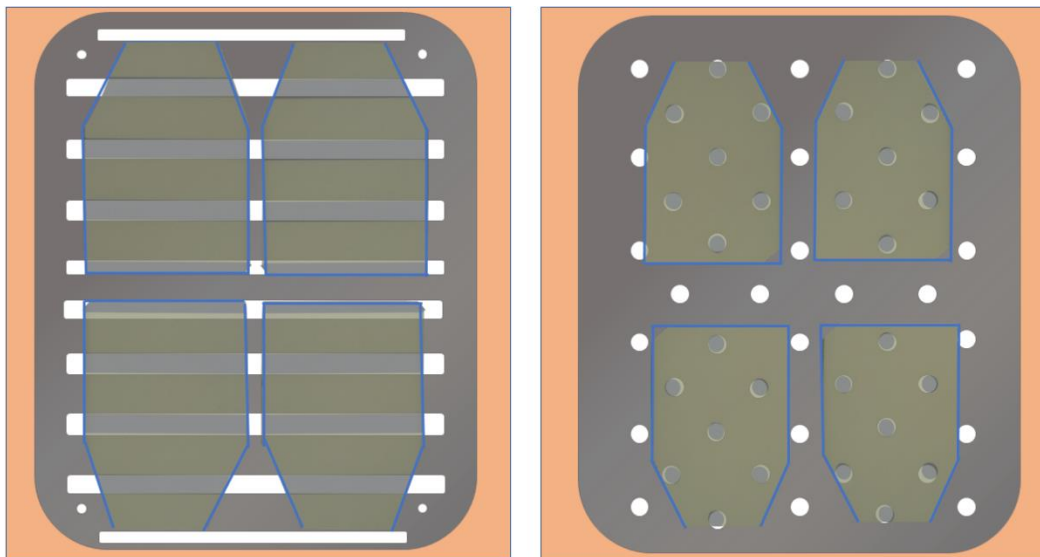


Figure 2-7. Illustration of how the Gafchromic™ films were positioned underneath the different GRID configurations. The films were of equal size in both GRID configurations, but the size has been modified to fit the illustrations. The blue lines indicate the outline of the cell flasks, and the background represents the cell flask holder.

2.1.2.2 Scanning

To ensure a stable optical density of the films, we waited 48 hours after irradiation before scanning the films (Devic et al., 2004).

An Epson Perfection V850 Pro flatbed scanner was used to digitize the films' radiation response. The films were placed in a central area of the scanner to minimize variations in scan readings (Lewis & Chan, 2015). Transmission mode was chosen, as recommended by (Aldelaijan & Devic, 2018). Using the Epson scan tool v.5.1 software we disabled automatic image corrections and adjustments to only extract raw data. Resolution of 300 dpi was chosen to achieve high enough spatial resolution while having a reasonable scanning time. A 16-bit color depth per channel ($0 - 2^{16}$) RGB image was chosen for satisfactory intensity resolution. The scanner was allowed time to warm up for 30 minutes, then 10 dummy scans were performed to limit warm-up effects causing variations in response readings (Paelinck et al., 2006). Four scans were made per film to account for possible change in intensity readings caused by the scanner. We found the largest relative percentage difference (RPD) between the mean pixel value of the four scans for all films to be approximately 0.1%. RPD between two measurements was found using the general formula

$$RPD = \frac{|A - B|}{(A + B)/2}.$$

The RPD was sufficiently small to neglect the scanners' effect on film response, and we could thus use the first scan exclusively in our dosimetry.

For a completely opaque film, light transmission should be zero. However, there will always be background noise. Therefore, a black sheet of paper was scanned, and its intensity was subtracted from all control and irradiated films.

The images were saved as TIFF (Tag Image File Format) without compression to retain as much information as possible from the images.

2.1.2.3 Film calibration

Calculating net optical density (OD) from the scanned images required image processing using Python. First the raw data of the images were read and separated into a red, green, blue, and grey channel. Grey channel conversion followed rec 601 (*Recommendation ITU-R BT.601-7, 2011*) using the formula

$$I_G = 0.299 \cdot I_R + 0.587 \cdot I_G + 0.114 \cdot I_B,$$

where I is pixel value.

In the cut area of the films a white color appears. These areas are undesirable, as they indicate damage to the film's sensitive layer. A Region of Interest (ROI) is therefore chosen in a central area of the calibration film that balances the need for sufficient datapoints and capturing the variance of the radiation field, while avoiding the edges of the film. A suitable ROI was found retrospectively, by evaluation of the mean squared error (MSE) from the non-linear fit of a dose-response model. Based on these calculations an ROI of $3 \times 3 \text{ mm}^2$ was chosen.

To measure darkening of the film due to irradiation we assessed the net optical density (OD). It describes the change in opacity compared to unirradiated films using the formula (Devic et al., 2004)

$$netOD_i = \Delta OD = \max \left[0, \log_{10} \left(\frac{\bar{PV}_{ctrl} - \bar{PV}_{bckg}}{\bar{PV}_{ctrl} - \bar{PV}_{bckg}} \right) \right] \quad 2-4$$

where \bar{PV}_{ctrl} and \bar{PV}_{bckg} was found by finding the mean pixel value within the ROI of the i^{th} control and background image, then finding a weighted average of these means (see Figure 2-8). The weights were based on the standard deviations of each mean following the relationship

$$w_i = \frac{1/\sigma_{PV}^2}{\sum_{i=1}^n 1/\sigma_{PV}^2} \quad (\text{Devic et al., 2004}). \quad \text{If the log returned a negative number, then the PV value}$$

of the irradiated film was larger than that of the control film, which should not be possible. We therefore set $netOD_i$ of that image to 0. $PV_{i,irr}$ is the mean PV of the ROI found for all irradiated films. A weighted average was not found for PV_{irr} , because we wanted each dose to have 8 accompanying films for increased precision when fitting the calibration curve. Using equation 2-3 we estimated the error in $netOD$ as

$$\sigma_{netOD_i} = \sqrt{\frac{\partial \Delta OD}{\partial PV_{ctrl}}^2 \cdot \sigma_{PV_{ctrl}}^2 + \frac{\partial \Delta OD}{\partial PV_{bckg}}^2 \cdot \sigma_{PV_{bckg}}^2 + \frac{\partial \Delta OD}{\partial PV_{irr}}^2 \cdot \sigma_{PV_{irr}}^2}$$

$$= \frac{1}{ln10} \sqrt{\left(\frac{\sigma_{\bar{PV}_{ctrl}}}{\bar{PV}_{ctrl} - \bar{PV}_{bckg}}\right)^2 + \left(\frac{\sigma_{PV_{irr}}}{PV_{irr} - \bar{PV}_{bckg}}\right)^2 + \left[\frac{\bar{PV}_{ctrl} - \bar{PV}_{bckg}}{(PV_{irr} - \bar{PV}_{bckg})(\bar{PV}_{ctrl} - \bar{PV}_{bckg})}\right]^2 \sigma_{\bar{PV}_{bckg}}^2}$$

For measurement films, all pixels were converted to netOD, hence no mean pixel value was found and $\sigma_{PV_{irr}} = 0$. We found $\sigma_{\bar{PV}_{ctrl}}$ and $\sigma_{\bar{PV}_{bckg}}$ using (Devic et al., 2004)

$$\sigma_{\bar{PV}_{ctrl}} = \frac{1}{\sqrt{\sum_{i=0}^n \frac{1}{\sigma_{i,PV_{ctrl}}^2}}}, \sigma_{\bar{PV}_{bckg}} = \frac{1}{\sqrt{\sum_{i=0}^m \frac{1}{\sigma_{i,PV_{bckg}}^2}}},$$

where n and m was the number of control and background films, respectively. $\sigma_{PV_{ctrl}}$ and $\sigma_{PV_{bckg}}$ represents the standard error of the weighted mean pixel value within the ROIs of the control and background images.

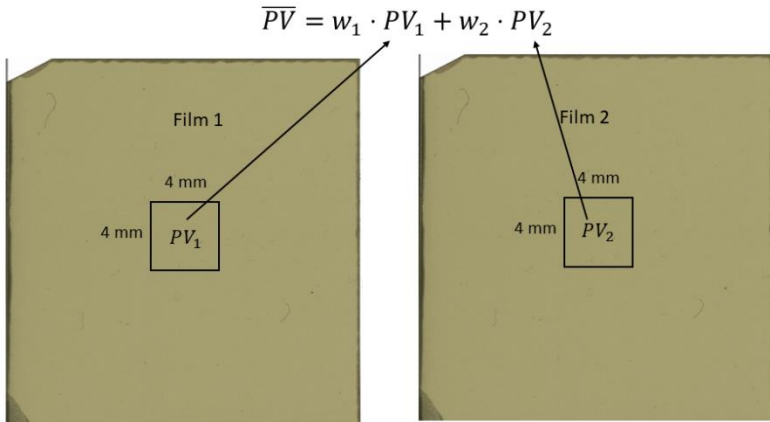


Figure 2-8. Illustration explaining the notation behind calculating weighted average pixel values \bar{PV} . Both PV_1 and PV_2 are mean pixel values within the $4 \times 4 \text{ mm}^2$ ROI.

When plotting netOD against dose it became apparent that the films differed in their response, which can be seen in Figure 2-9. It appeared that the film response was split in two categories: “low” and “high”. This was not the case for the second set of calibration films, which complicated the process of converting from netOD to dose (discussed further down). Using kernel density estimation (KDE) we were able to separate the films. KDE estimates the probability density function (PDF) of the data (Silverman, 1998, p.1). The method sorts the data in increasing order, before centering a kernel over all the datapoints. The kernel is a known PDF

with a specified smoothing parameter called bandwidth. For our netOD data we used a Gaussian kernel, where the bandwidth acts as the standard deviation in the Gaussian PDF. The kernels are

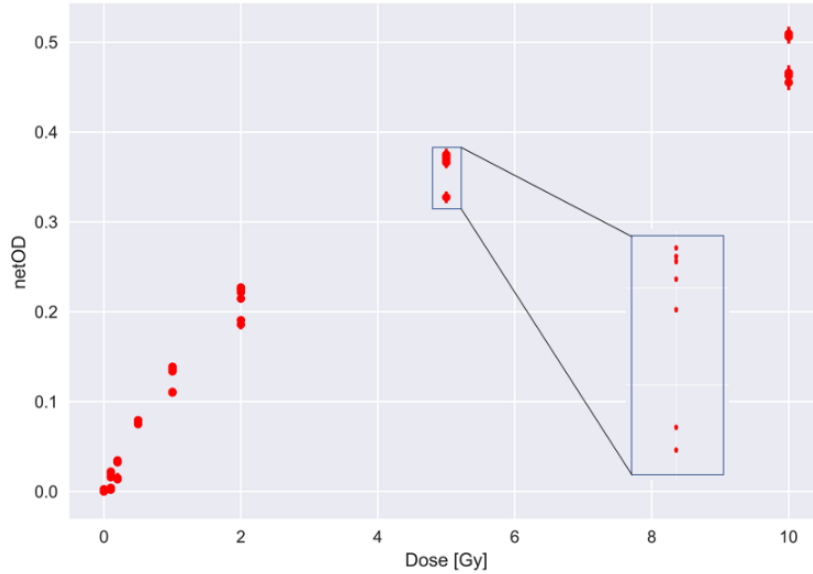


Figure 2-9. Illustration of the split response in netOD. This was apparent in all color channels.

summed together, and the sum increases if kernels are within each other's bandwidths. We used a python package called *sklearn.neighbors* (Pedregosa et al., 2011) with the module *KernelDensity*. This function finds the log likelihood of the kernels. We know that we have two response groups, and it is therefore possible to identify the global minimum of the log likelihood curve to obtain the index separating the netOD values into high or low response. This method was also used for the measurement films.

Following separation of high and low response, we could fit the data to a model explaining the relationship between dose given and netOD measured $D(\text{netOD})$. Bjørg Vårli Håland evaluated models using corrected Akaike Information criteria (AIC_c). We will come back to the concept of AIC in 2.4.3.5 , but we will not perform the same analysis. Based on the results of Bjørg Vårli Håland, we chose the model

$$D = a \cdot \text{netOD} + b \cdot \text{netOD}^n , \quad 2-6$$

where a , b , and n are unknown parameters. The python package *scipy.optimize* with the module *least_squares* estimates the parameters using the LM method. It also returns necessary

goodness of fit values to evaluate the model. Extracting uncertainties of the estimated parameters is not trivial, as they are not returned by the function. However, it does return the Jacobian (see 1.6.1), which can be used to find the variances of each parameter. Using the relationship (Niclas Börlin, 2007, slide 12)

$$\Sigma = \sigma^2 H^{-1},$$

where Σ is the covariance matrix, a $p \times p$ matrix explaining how the parameters in \mathbf{p} vary following the expression

$$\Sigma(p_x, p_y) = \frac{1}{n-1} \sum_{i=1}^n (p_{x_i} - \bar{p}_{x_i})(p_{y_i} - \bar{p}_{y_i})$$

The diagonal element of this matrix reduces to $Var(p_x)$. H^{-1} is the inverted hessian matrix. From 1.6.1 we saw that the hessian matrix could be approximated to $J^T J$, without the weights \mathbf{W} . σ^2 is the standard error of the residuals. Combining these elements, we found the variances of each estimated parameter. The LM method demands an initial guess of parameters. We evaluated the robustness of the algorithm by initializing random guesses for a,b and n, where the guesses came from a standard normal distribution. The output parameters were recorded to observe if the algorithm consistently converged to the same parameters. The only criterion was that $n > 0$. All color channels were fitted, but only one channels was chosen for dosimetry. The channel selection was decided based on the respective color channels' sensitivity to dose (Stevens et al., 1996) and the mean squared error (MSE) of the fit. The red color channel proved to have highest sensitivity and lowest MSE.

With an established response between dose and netOD, we could perform netOD calculations on the measurement films. Then these pixel values of the films were first converted to netOD using equation 2-4, before they were classified as either high or low response using the KDE method. Then these pixel values were converted to dose using the newly fitted equation 2-6. No ROIs were used because we wanted each pixel in the image to correspond to a dose measurement. This made it possible to determine peak and valley doses in the GRID irradiated films. Uncertainty in dose measurements were calculated using error propagation of the fitted function in equation 2-6.

2-7

$$\sigma_{D_{fit}} = \sqrt{\frac{\partial D^2}{\partial a} \cdot \sigma_a^2 + \frac{\partial D^2}{\partial b} \cdot \sigma_b^2 + \frac{\partial D^2}{\partial netOD}^2 \cdot \sigma_{netOD}^2 + \frac{\partial D^2}{\partial n} \cdot \sigma_n^2}$$

$$= \sqrt{netOD^2 \sigma_a^2 + (netOD^n)^2 \sigma_b^2 + (a + bn \cdot netOD^{n-1})^2 \sigma_{netOD}^2 + (b \ln netOD \cdot netOD^n)^2 \sigma_n^2}$$

One mean dose map was generated for OPEN field and both GRID configurations based on the 16 irradiated films following the formula

$$\frac{1}{\# \text{films}} \sum_{i=0}^{\# \text{films}} \mathbf{D}_i \quad 2-8$$

where \mathbf{D}_i is the i^{th} dose map. The steps taken to generate the mean dose map is illustrated in Figure 2-10. The estimated uncertainty in the mean dose map was a combination of fitting uncertainty found from equation 2-7 and the standard error in the pixels across the 16 measurement films. Each pixel has a standard error from the fit σ_{fit} . Because our mean dose was calculated using equation 2-8 we can find the corresponding error using

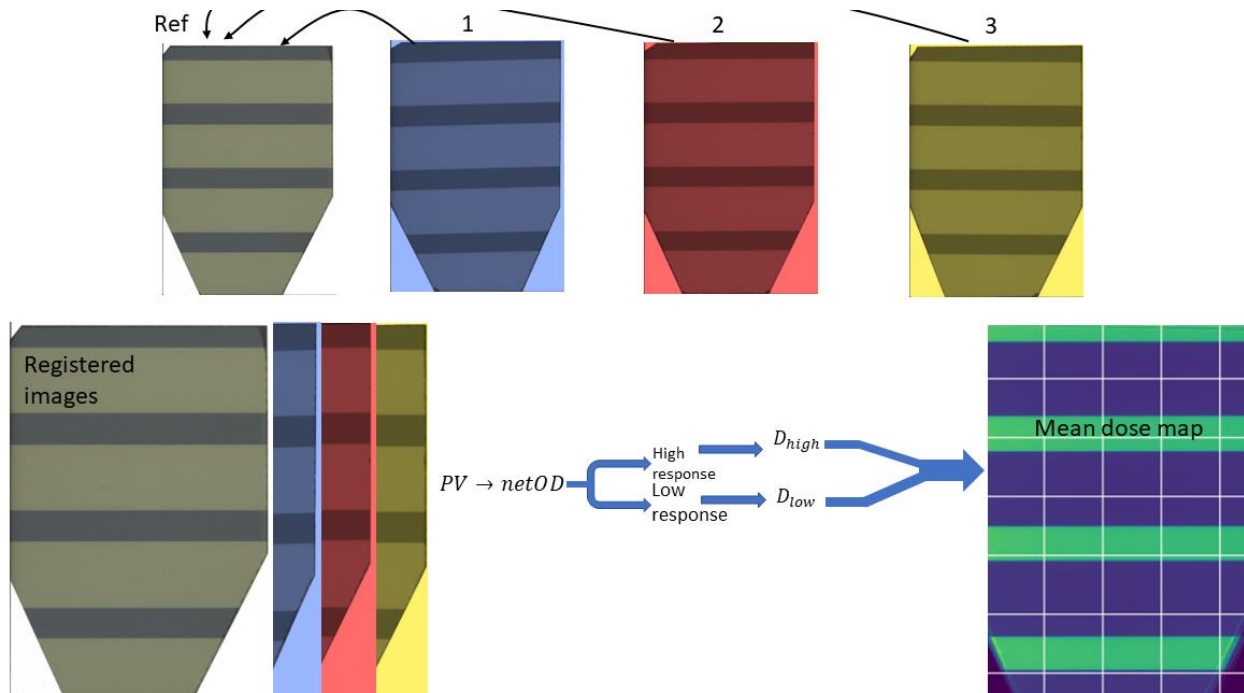


Figure 2-10. An overview of registration process to generate a mean dose map from the measurement films. First all films were registered to the first film in the folder (reference image), then each image pixel value converted to netOD using equation 2-4, before being converted to dose via equation 2-6. Then all dose films are averaged to generate a mean dose map. This process is equal for all irradiation configurations: OPEN field or GRID.

$\frac{1}{\#films} \sum_{i=0}^{\#films} \sigma_i^2$, where $\sigma_i = [\sigma_{D_{fit,0}}, \sigma_{D_{fit,1}}, \dots, \sigma_{D_{fit,n}}]$. As a consequence of the split response, the uncertainty of high and low response was found separately before being combined to total standard error of fit $\sigma_{fit,tot}$. Similarly, a total standard error of each pixel across the measurement films of high or low response was calculated $\sigma_{\bar{D},tot}$. Finally, we combined all the errors to get the total standard error of the mean dose map $\sigma_{tot} = \sqrt{\sigma_{fit,tot}^2 + \sigma_{\bar{D},tot}^2}$.

Stacking dose maps to generate one, demanded pixel to pixel correspondence between the individual dose maps. It was therefore crucial that the maps were spatially aligned. However, because of poor accuracy when cutting the measurement films, they were not equally positioned within the cell flask (see Figure 2-11). We therefore had to co-register the measurement films. The only possible displacements of the EBT3 films were rotational and translational; hence a rigid body registration (preserving Euclidean distance) was performed.

A python module called *pystackreg* (*version 0.2.5*) was used. The package is a port of the imageJ extension TurboReg/StackReg based on a paper by Thevenaz et al. Turboreg is a subpixel registration algorithm that aligns a source image f_S to a reference image f_R , both with dimension M x N (rows, columns). Subpixel means that the algorithm has an error less than ± 1 pixel. Turboreg uses the integrated square difference of the intensity values as a cost function denoted by ϵ^2

$$\epsilon^2 = \int \int f_R(x, y) - Q_p\{f_S(x, y)\} dx dy = \|f_R(x, y) - Q_p\{f_S(x, y)\}\|^2,$$

where Q_p is a transformation of the source image (e.g., translation, rotation scaling etc.) parametrized by \mathbf{P} . The goal is to find a transformation that minimizes the intensity difference, by tuning the parameters in \mathbf{P} following

$$\frac{\partial \epsilon(\mathbf{P})^2}{\partial \mathbf{P}} = 0$$

The algorithm uses a modified LM (see 1.6.1 for general LM) to find the optimal parameters. When a minimum is reached, or number of maximal iterations is reached, it returns a 3×3 transformation matrix. To optimize the registration various degrees of preprocessing was necessary. Calibration films had smaller displacements compared to the measurement films, but were registered to ensure that the region of interest (ROI) was positioned equally in all calibration films.

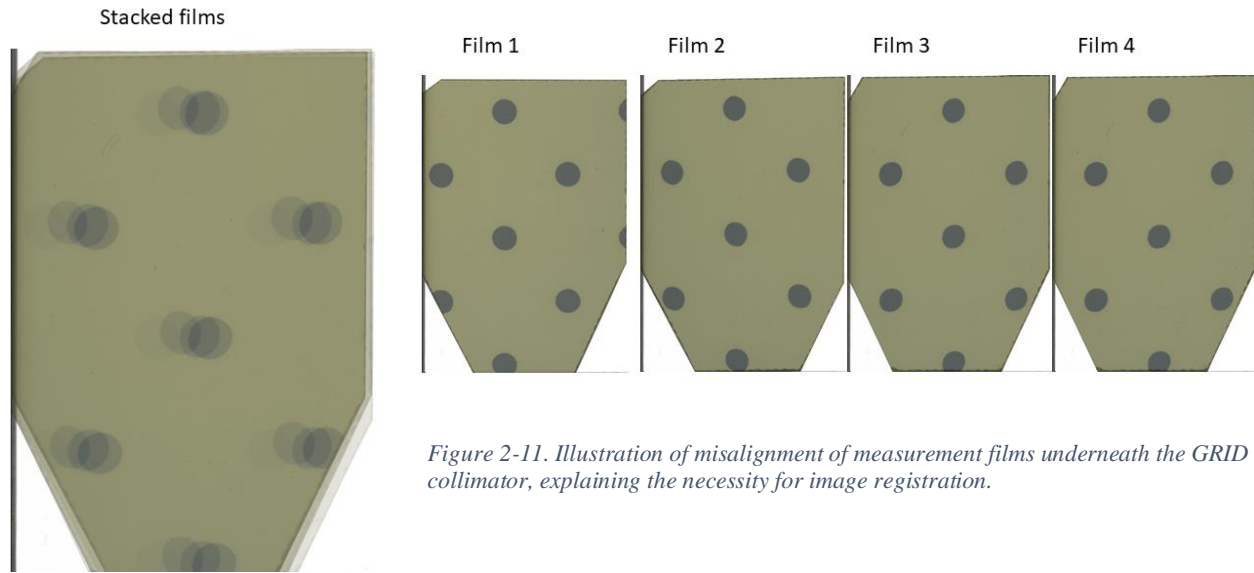


Figure 2-11. Illustration of misalignment of measurement films underneath the GRID collimator, explaining the necessity for image registration.

Pystackreg tended to align the background of the image, rather than the objects within. Therefore, a small crop of 10 pixels in each direction of the image was made. We wanted all images to be aligned to the first image in the folder. However, the high intensity discrepancy of the calibration films for doses ranging from 0 Gy to 10 Gy; caused large errors in the registration. We therefore registered each image to the neighboring image. This was not required when registering the measurement films, as they were all irradiated with 5 Gy. The background of the measurement films had to be dulled as well as cropping the image. We chose to use a package called *skimage.transform*, which includes a function called *warp*. *Warp* both applies the transformation matrix on an image and interpolates. Interpolation is necessary because when an image is transformed, each pixel is mapped into a new coordinate $P(x, y) \rightarrow P'(x', y')$ (Ashburner & Friston, 2007). For instance, rotating an image is done by applying the rotational matrix \mathbf{R} , with added translational elements t_x and t_y , on each coordinate of the image

$$\begin{bmatrix} x' \\ y' \end{bmatrix} = \begin{bmatrix} \cos \theta & -\sin \theta & t_x \\ \sin \theta & \cos \theta & t_y \\ 0 & 0 & 1 \end{bmatrix} \begin{bmatrix} x \\ y \end{bmatrix}.$$

It results in non-integer coordinates with unknown intensity values. The easiest solution is to round the coordinates to nearest integer and use the intensity values of these coordinates (called nearest neighbor interpolation). However, a more accurate interpolation called bi-cubic interpolation was used. We will not go into detail, but the method looks at the 16 neighboring pixels and estimates the unknown pixel's intensity value from these (Han, 2013). It is an advantage to extract the transformation matrix before applying it, because you can make small corrections to the registration by tuning the rotational and translational parameters.

1D dose profiles were made from the 2D maps by calculating the mean dose in each pixel row along the height of the films within a limited area (Figure 2-12) The left figure shows how the dose profiles were drawn. The figure on the right shows the resulting profiles for OPEN field and striped GRID. An upper and lower limit was chosen to remove variations caused by areas where the GRID openings were of unequal length. From the dose profiles we estimated the dose prescribed with OPEN field and GRID, in the peak and valley areas. For OPEN filed, mean dose was found from all 16 dose profiles generated from the irradiated measurement films. The dose

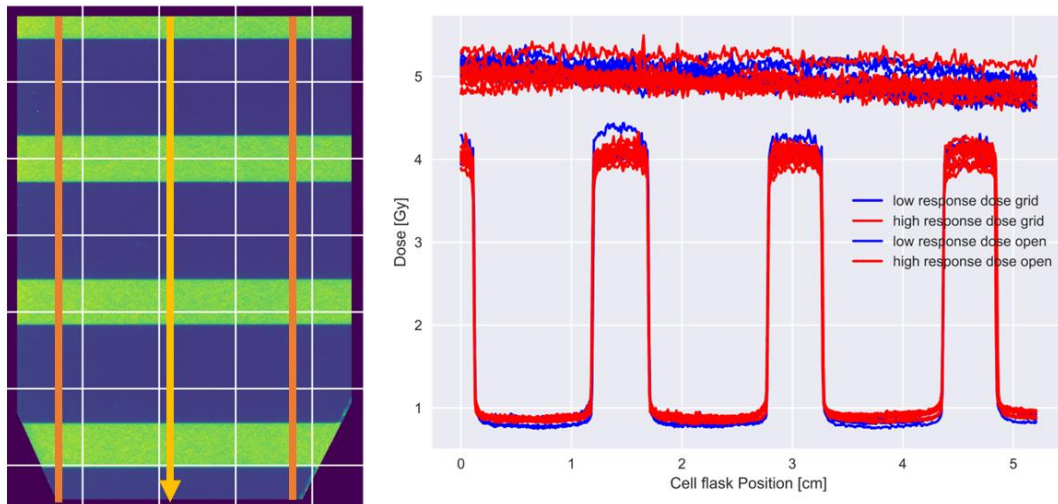


Figure 2-12. Dose profile for striped GRID measured by calculating mean dose for each pixel row in the image (y-axis). Each row was cropped within the orange lines before making a dose profile (right figure) to remove variations in mean dose caused by areas where the GRID pattern was not of equal length.

profiles for GRID irradiated measurement films were separated into datapoints that were within the peak or valley dose category. Peak and valley doses were defined as being **above** 95% of maximum dose, and **below** 105% of the minimum dose, respectively. Then the mean dose of all these datapoints was found. Uncertainty was estimated by combining the total uncertainty of all films, both high and low response. As mentioned, the lack of high and low response in the calibration films for dotted GRID complicated the fitting of equation 2-6. When plotting the netOD from these films together with the data from the first calibration, we saw that films belonging to certain dose categories exhibited **only** low or high response, **not** both (see Figure 2-13). As a solution, we tried two approaches: First, the calibration films were fitted ignoring the possibility of high and low responses. The fit was subsequently used on the measurement films, converting their netOD values to dose. Second, we did not ignore the high and low responses and used the fitting parameters from the first calibration on the high and low response measurement films, respectively, assuming only two possible responses.

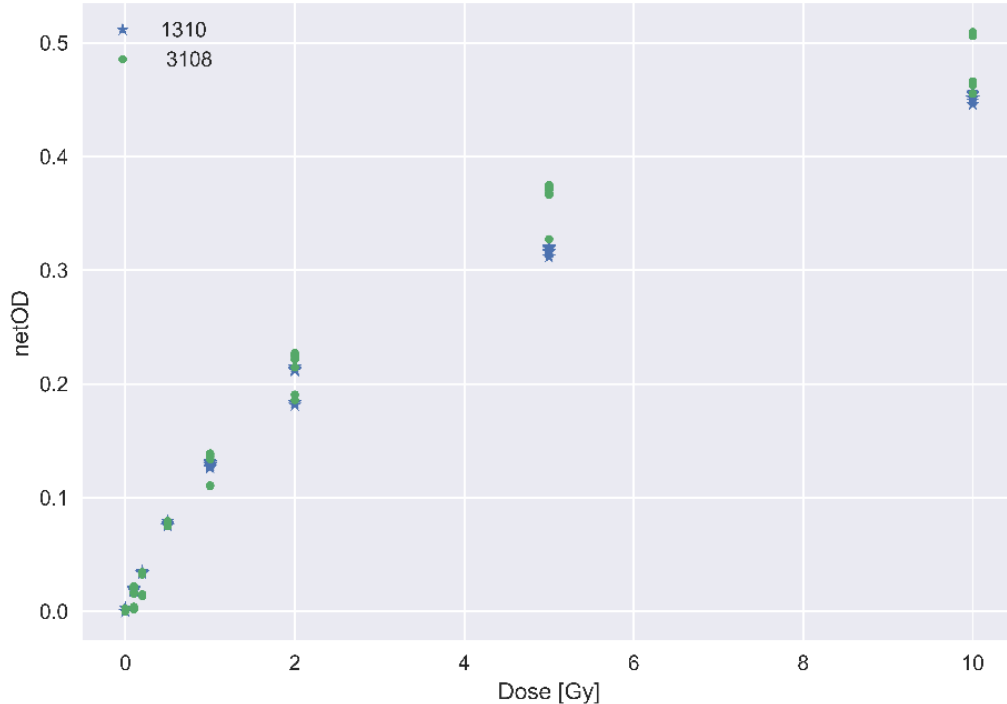


Figure 2-13. netOD of red channel for both sets of calibration films performed at two different time points. We see a clear separation of the netOD from the first calibration for the same dose, but this is often not the case for the second calibration films. A clear observation of this scenario can be seen for 5 and 10 Gy.

2.1.2.4 Dose evaluation by Monte Carlo simulations

Striped GRID dosimetry for GRID was validated with Monte Carlo simulations performed by Delmon Arous, PhD-student. He used FLUKA version 4-2.1 (Battistoni et al., 2015; Böhlen et al., 2014), a particle physics Monte Carlo simulation package to simulate how the photons would interact in our experimental setup (Figure 2-6), including chemical composition of EBT3 films, the T25 cell flasks, the 220 kV photon energy spectrum filtered through 0.7 mm Cu and 1.52 mm Al and the collimation of the beam through the GRID collimators. The algorithm follows the photons' interactions until a specified cutoff energy has been reached, and the remaining energy is deposited locally (N. Reynaert et.al, 2006). Cutoff energy of 1 keV was chosen for photons and secondary electrons (Jabbari, 2011), and a total of $2 \cdot 10^7$ primary X-rays were simulated. With these Monte Carlo simulations, the absorbed dose within the EBT3 films was numerically estimated.

2.2 Cell Experiments

Cell experiments were performed by Magnus Børsting in his master thesis:
“*GRID irradiation and bystander effect in lung cancer cells*”
(Magnus Børsting, 2020, p. 45-56).

A549 cells were chosen for in vitro GRID irradiation. The cell line is an alveolar basal epithelial cancer cell originating from the study of 200 human tumors, where the goal was to establish cell lines for laboratory research (Giard et al., 1973). An alveolar cell originates from the alveoli of the lungs, which are small cavities that exchange oxygen for carbon dioxide. Epithelial cells are cells that covers the surface areas of the body (*Epithelium / Anatomy / Britannica*, 2009). Basal means that the cell is found in the deepest layer of the epithelium (Morgenroth & Ebsen, 2008, p.70). A549 cells are well suited for GRID experiments, as the cell lines has exhibited radiation induced bystander effects in previous studies (Ghasemi et al., 2020; Yang et al., 2015). 30 000 cells were seeded with 6 ml growth medium in a T25 cell flask (Nunclon, Denmark) with 25 cm² cell culture area. The cells were incubated in an incubator (Thermo, USA) holding 37°C with a CO₂ percentage of 5%. The number of 30 000 was found by Magnus Børsting after performing a pilot experiment where different cell densities were used. All experiments used 30

000 cells to remove variability in survival that occurs for different cell densities. The number was chosen because it best balanced the need of having sufficient cell density to leave some surviving colonies at high doses and having non-confluent (confluence: fraction of cell flask area covered by cells) colonies at low doses. The irradiations of the cells were done using the same experimental setup as shown in Figure 2-6, and the same X-ray beam settings were chosen, with the same filtration. However, no EBT3 films or nylon6 slabs were used. The cells are as mentioned seeded at the bottom of the cell flask, with medium covering the cells acting as buildup. The irradiation cabinet seen in Figure 2-2 has a heater, ensuring the ideal temperature of 37°C. One source of uncertainty was that the dosimetry was performed following a protocol proposed by a former master student Anne Marit Rykkeliid. In this protocol the exposure times necessary for desired dose did not account for the height difference between the sensitive volume of the ionization chamber and the bottom of the cell flask, where the cells are seeded. Nominal doses of 2, 5 and 10 Gy were chosen. Four flasks were used per dose point, including control flasks. The irradiation was done for OPEN field, GRID stripes and GRID dots.

A colony is a cluster of more than 50 cells (Franken et al., 2006). Number of colonies formed after irradiation was our metric of survival. It was chosen to wait six days before fixating the cells, seeing that a typical doubling time for A549 cells is 22 h (*A549 Cell Subculture Protocol – A549 Cell Line*, n.d.). Fixation of cells is the process of fixing the cells in their position and terminating all ongoing biological mechanisms, essentially killing them and disabling their natural degradation mechanisms so they can be viewed in a microscope (Panzacchi et al., 2019). 3 ml of Ethanol was used to fixate. Ethanol was chosen because it is fast and has optimal preservation of cell structure (Rahman et al., 2022). 3 ml of methylene blue dye was then added to stain the colonies. Because of a specific chemical reaction that only occurs in living cells, only dead cells are colored by the dye (O'Connor-Cox et al., 1997).

After fixation and staining the cell flasks with cells were scanned by Bjørg Vårli Håland the same way as the EBT3 films (see 2.1.2.2), except using a dpi of 1200 with the resolution of 2220 x 2976 x 3. The cell flasks have a height making it impossible to close the scanner completely. The scans of the cell flasks will therefore have a slight angle, causing a sharp dark shadow on the image.

2.3 Segmentation

Segmentation of cells was performed by Delmon Arous in the article:

“Principal component-based image segmentation: a new approach to outline in vitro cell colonies”. (Arous et al., 2022).

This section uses the same notation found in (Strang, 2006, p.425-427).

The scanned cell flask images were segmented using an algorithm combining PCA, GLCM, k-means and topological multi-threshold watershed. The segmentation algorithm was developed in MATLAB. PCA is principal component analysis and aims to reduce the dimensionality of the image while retaining most of its variation (Jolliffe, 2002, p. IX). For ease of explanation, one scanned image of a cell flask is used as an example. The dimension of the image is M x N x 3.

By collapsing the first two dimensions and transposing the matrix, you get the matrix

$X \in \mathbb{R}^{3 \times MN}$. Each column represents the RGB values $[r_i, g_i, b_i]^T$. The data is centered around the origin by subtracting the mean $\mu \in \mathbb{R}^{3 \times 1}$ of each row of X from the r_i , g_i and b_i values, to generate $\hat{X} = X - \mu$. The covariance matrix $C \in \mathbb{R}^{3 \times 3}$ is generated from \hat{X} and explains how the color channel intensity values r, g and b vary among themselves.

Through Singular Value Decomposition (SVD), which will not be elaborated further, eigenvectors of C are found and represented by the matrix $P = [\mathbf{u}_1, \mathbf{u}_2, \mathbf{u}_3] \in \mathbb{R}^{3 \times 3}$. The eigenvectors are ordered in descending order, from highest to lowest variance. The important thing to note is that the eigenvectors are per definition uncorrelated, so they represent different parts of the image. It is therefore possible to isolate the eigenvector that represents the variance of the clusters of cell colonies in the image. Using the eigenvectors, you can transform the data in \hat{X} into the PCA space using the transformation

$$\hat{Y} = P\hat{X} = \begin{bmatrix} \mathbf{u}_1^T \hat{X}_i \\ \mathbf{u}_2^T \hat{X}_i \\ \mathbf{u}_3^T \hat{X}_i \end{bmatrix},$$

where \hat{Y} are the new pixel values in the transformed data. \hat{Y} is divided into three parts I_{PCA1} , I_{PCA2} and I_{PCA3} , which is named the PCA images with dimension 1 x MN. Deciding which image that contains cell colony variance was decided using the Grey-level co-occurrence

matrix (GLCM) (Haralick et al., 1973). Here, it was implicitly assumed that the suitable I_{PCA} is composed of pixel values that are insensitive to and suppress the presence of various high-contrast artefacts, such as contaminants or residue in the suspension medium, shadow artefacts or background noise from the scan acquisition and the cell container boundary. With a suitable I_{PCA} it was necessary to distinguish background from foreground, that is separating cell colonies from the cell flask. Using k-means on clusters of 9 pixels (one central pixel, with eight surrounding pixels), the pixels were assigned to either foreground or background (Lloyd, 1982). The resulting matrix is a binary mask (only two intensity values) with foreground objects named Binary Large Objects or BLOBs.

Topological multi-threshold watershed segmentation was then applied to separate the BLOBs (see Figure 2-14) into individual colonies (Khan et al., 2016). The watershed works by identifying parts of an image with local intensity minima known as catchment basins. These areas are labeled with colors to identify different objects within the image (Preim & Botha, 2014, p.130). If watershed was used on the original scanned images, which does contain noise, dust etc. it would see all these artefacts as cell colonies. But because the BLOB's coordinates were extracted using PCA, they are independent from the mentioned artefacts. Each BLOB was searched for local minima in intensity, but watershed has a tendency to over-segment an image caused by naturally occurring variations in intensity (Preim & Botha, 2014, p.130). Therefore, minima with depth less than a threshold value h were suppressed.

After segmentation, the program returned information about individual colonies' centroid coordinates, area, circularity, mean and standard deviation of intensity, as well as delineated cell flask images (see Figure 2-14).

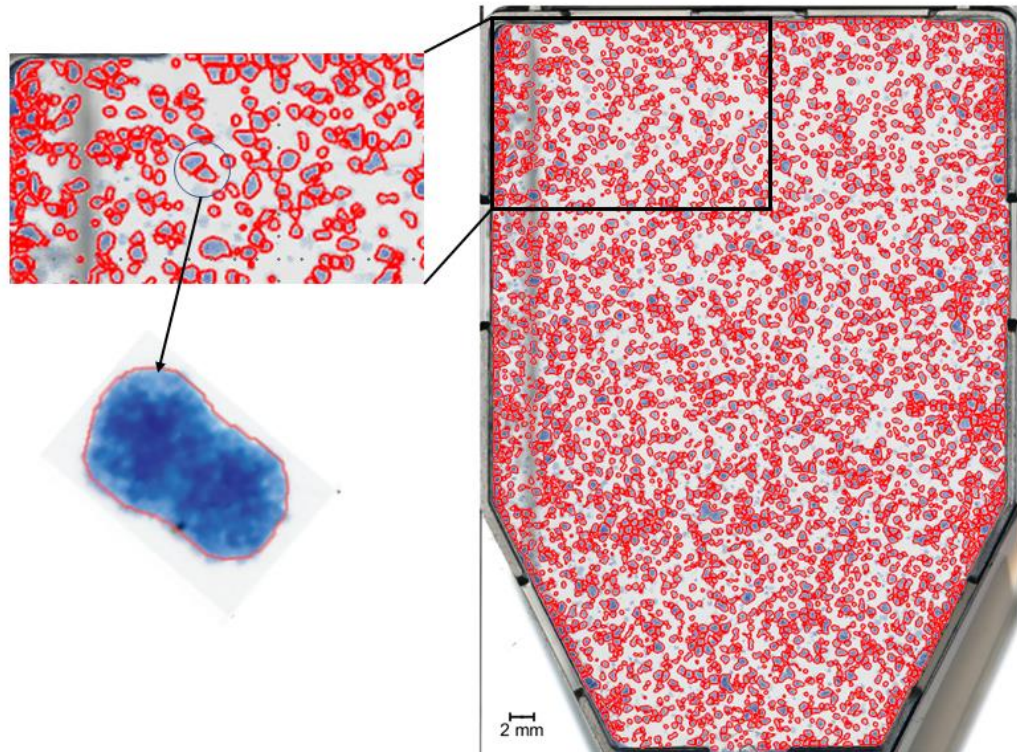


Figure 2-14. An example where the segmentation algorithm tries to decide whether the proposed BLOB is one or two colonies. The red circles are delineations of the stained colonies. Here we see a successful delineation of two separate colonies within a BLOB.

2.4 Cell Survival Analysis

With an established dosimetry for the cells, we could analyze the survival data from Delmon Arou's segmentation program. Magnus Børsting performed four different single fractionation experiments. The irradiation configurations used in these experiments are summarized in Table 2-2. An LQ model was fitted for analysis of OPEN field survival data, while a band analysis proposed by Bjørg Vårli Håland was employed on striped GRID data to have a basis of comparison for the novel 2D approach (see below).

Table 2-2. Segmentation data generated by Delmon Arous, PhD student, from experiments performed by Magnus Børsting, former Msc student.

	Experiments			
Configurations	18.11.2019	20.11.2019	03.01.2020	17.12.2020
OPEN	✓	✓		✓
GRID Stripes	✓	✓		✓
GRID Dots		✓	✓	✓

2.4.1 Data acquisition and image registration

The scanned cell flask images will from here on, be referred to as cell flasks and the scanned film images will be referred to as dosimetry films or simply films.

For our novel 2D survival analysis (see below) we used absolute counting data of the number of colonies per area was required. As mentioned in 1.7.4, one might normalize survival data using the plating efficiency to compare experiments performed under different conditions, but this will not be possible with the proposed approach. Thus, data series deviating greatly with respect to plating efficiency should be omitted. Still, we wanted to use as much clonogenic survival data as possible. We therefore performed an Analysis of Variances (ANOVA, explained in 2.1.2.2) to evaluate the differences in mean number of colonies found in the four control cell flasks per experiments. There was no significant difference between experiments performed on the 18.11.2019 and the 20.11.2019, and we therefore chose to combine these results in our analysis. Using the centroid coordinates of the cell colonies we created a **colony map** (binary), where intensity value 1 indicated a cell colony. The coordinates provided by the segmentation algorithm were in decimals, and it was therefore necessary to round to nearest whole number pixel to place the colony in the colony map. In our 2D analysis we divided the colony maps into quadrats of different sizes. The smallest size of our quadrats was 0.5 mm², which for 1200 dpi corresponded to a 24 x 24 matrix (with a 47 pixels/mm conversion factor).

The mean dose map was registered to the colony maps. Because the dose map was based on EBT3 films registered to the first film of the folder (reference film) (Figure 2-10), and colony maps were registered to each other by Delmon Arous, it was only necessary to register the reference film to one of the colony maps. Then we used the obtained transformation matrix on the mean dose map. Final tuning of said transformation matrix was made to achieve ideal match between the dose map and the colony map. As mentioned, the different irradiation configurations (GRID Stripes or Dots or OPEN field) needed various degrees of image processing, but the common modification was to match the resolution of the images. We chose to upscale the resolution of the films (300 to 1200 dpi), which was done to retain as much accuracy as possible when pinpointing the positions of the cell colonies. Downscaling an image may result in valuable information being lost, and the centroid position of the colonies would be spread out onto four pixels if $1200 \rightarrow 300$ dpi had been chosen.

The films and the colony maps have different image information, and we therefore needed to create binary maps to enhance the similarity of the images and subsequent registration. For instance, in the striped GRID we see dark striped patches in the peak area matched by a decrease in survival in the same area of the cell flasks (see Figure 2-15). This approach was also used for OPEN field and dotted GRID. We still used a rigid body registration because the main displacements were still translational and rotational.

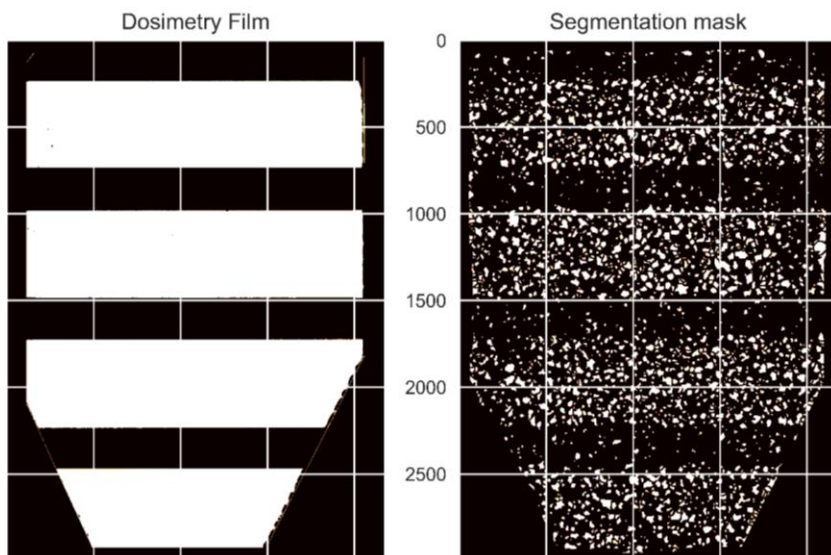


Figure 2-15. How the patterns of the segmentation mask and the dosimetry films were matched for better registration. One of the 16 dosimetry films for striped GRID can be seen on the left, and the segmentation mask of counted colonies can be seen on the right.

2.4.2 1D survival analysis

A 1D analysis of survival, as introduced by Bjørg Vaarli Håland, was performed to have a basis of comparison to our novel 2D analysis. For OPEN field data all colonies within an area of the films with reliable data (discarding colonies near the edges) were summed. The number of colonies for control and irradiated flasks were normalized to control before being log transformed. They were then fitted using the traditional LQ model. Log transforming equation 1-24 we get the quadratic expression

$$\log S = -\alpha D - \beta D^2 ,$$

that we could fit using ordinary least square (OLS) fitting from the *statsmodels* package (Seabold & Perktold, 2010) in *Python*. It finds the optimal parameters, with uncertainty, using the closed form solution of least squares (see 1.6.1). The OLS function takes the response variables \mathbf{y} and the explanatory values \mathbf{X} . It demands \mathbf{X} to have the shape m x n, with m datapoints and n explanatory variables. With dose and dose squared as explanatory variables we get the matrix

$$\mathbf{X} = \begin{bmatrix} 1 & d_{0,1} & d_{0,2}^2 \\ 1 & d_{1,1} & d_{1,2}^2 \\ 1 & d_{2,1} & d_{2,2}^2 \\ \vdots & \vdots & \vdots \\ 1 & d_{n,1} & d_{n,2}^2 \end{bmatrix},$$

where the first column was added so statsmodels fits an intercept as well as α and β . We only used data from 2 and 5 Gy, because the segmentation algorithm did not perform well for 10 Gy OPEN field. We therefore had to extrapolate the fit to cover 10 Gy. Because all flasks were seeded with 30 000 cells, we normalized the data using mean survival of the control flasks across all experiment included in the analysis to obtain SF. The 95% confidence interval of estimated survival was found using *statsmodels*' own method.

Striped GRID data were analyzed by iterating over the rows of the colony maps and summing up number of SC within each row. As seen in (Figure 2-15), not all rows have an equal area to grow cells. Using a binary template image of the cell flask (0 is background 1 is cell flask), provided by Delmon Arous, we found a weighting factor for each row-sum based on the ratio of zeros and ones $w = 1 + \frac{\text{zeros}}{\text{ones}}$. We divided the rows into survival bands of specified widths and summed up

the colonies within the bands. Survival profiles along the height of the colony maps (y-axis) were made by calculating mean survival within the bands across all colony maps (Figure 2-16). The observed survival was compared to the survival predicted by the LQ model for homogeneous, OPEN field. Because of the heterogeneous dose distribution generated by the GRID, predicting survival was done by making similar survival profiles generated by inserting the mean dose profile for 5 Gy striped GRID irradiated measurement films into the fitted LQ model.

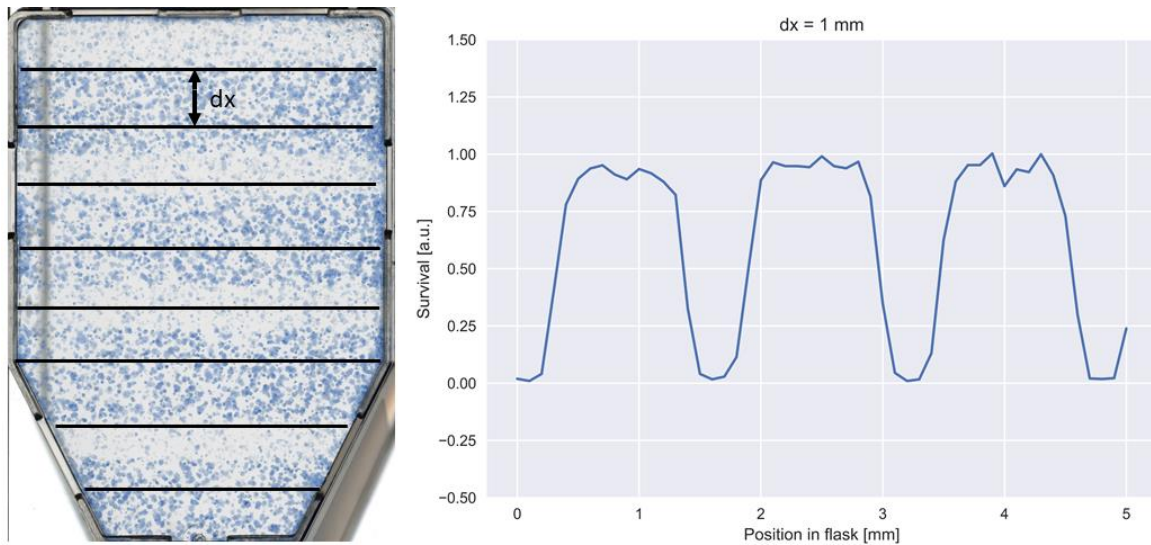


Figure 2-16. Illustration of 1D analysis of striped GRID irradiated cell flask. The colony maps were generated from segmented colony maps from segmented cell flasks and divided into bands of 1 mm width, where the colonies within these bands were counted. Note: The figure is meant for visualization, and is not an accurate representation.

2.4.3 2D survival analysis

The 1D method of analysis was best suited for striped GRID as the survival naturally separated into high and low survival bands following the shape of the GRID. However, such a model would not work for dotted GRID, and we wanted an analysis that was independent of GRID configuration. We therefore introduced a 2D analysis method where the colony maps were divided into equally sized quadrats and the number of colonies within were summed and fitted with Poisson regression (1.6.2). The Poisson regression was chosen because the cell survival can be assumed to be Poisson distributed (Nomiya, 2013). Also, since we divided the area into quadrats it was not straightforward to normalize the data with control leaving us with whole number survival not SF, which is suitable for the Poisson regression.

2.4.3.1 Pooling

We started by dividing the registered colony maps and dosimetry films into equally sized quadrats. Because of the geometrical displacement mentioned in 2.1.2.3, after registration, the GRID patterns would match nicely but the edges of the image would not. This limited the area where we had accurate dose measurements, thereby limiting the amount of survival data we could include.

The number of colonies within each quadrat was summed using a *python* function called *LPOOL2D* from the *pytorch* library (*LPool2d — PyTorch 1.11.0 Documentation*, n.d.). The function lets a $n \times n$ kernel move in strides across the image, computing the power-average within the kernel

$$f(X) = \sqrt[p]{\sum_{x \in X} x^p}.$$

Setting p to 1, it simply finds the sum of the pixels within each kernel. We talk about kernels as being dynamic, while the quadrats are fixed in place. The process of sum pooling is visualized in Figure 2-17. Choosing a kernel and a stride with the same size as the quadrats, will let the kernel jump from quadrat to quadrat extracting the desired quantity from the pixel values within the quadrat. Because we had generated dose maps where each pixel constituted a dose value, we had to find the mean dose of all pixels within the quadrat. The mean dose was found in a process very similar to sum pooling called average pooling using the *AvgPool2D* (*AvgPool2d — PyTorch 1.11.0 Documentation*, n.d.), which finds the average pixel value within the kernel. Choosing the right size of the quadrats is important, because we want to cover enough pixels to get a significant number of colonies within the quadrat. A 1×1 pixel sized quadrat would greatly inflate the number of quadrats not containing any colonies (zero inflation), making the data deviate from the Poisson distribution (Perumean-Chaney et al., 2013). But the size of the quadrats must be adequate, so that the number of quadrats is large enough to have sufficient data for Poisson regression. Also, choosing too large quadrats will lead to smoothing of doses because the quadrats might cover an area between a peak and a valley.

We examined the striped GRID survival data within quadrats using sizes of 0.5×0.5 , 1×1 , 2×2 , 3×3 and 4×4 mm². Evaluations of each size were made using a set of measurements: zero

inflation, dose variance (smoothing), relative percentage difference (RPD) between variance and mean for peak and valley survival and a chi-squared (χ^2)-test. We assumed that optimal quadrat size was the same for both GRID configurations. Figure 7-6 and Figure 7-7 are visualizations of see the cells with their associated dose for 0.5- and 4-mm quadrat sizes and increasing doses. For striped GRID, larger quadrat sizes will not necessarily impact the results significantly compared to dotted GRID but making the quadrats smaller will generally reduce the “smoothing” errors. Zero inflation was found by pooling the colony maps generated from the control cell flasks and finding the number of quadrats with zero colonies. Dose variance was found by calculating the variance of the average pooled dose maps. RPDs were found by separating the mean dose map for GRID into peak and valley doses, where peak and valley doses were defined as greater than 70% of maximum, and smaller than 115% of minimum dose, respectively. We increased the definition of peak and valley doses to ensure enough data within each respective category. Quadrats outside these dose ranges were not included. Because the Poisson regression assumes Poisson distributed data with equal variance and mean, we calculated the RPD between these quantities for peak and valley quadrats.

The χ^2 -test is a significance test, to test whether the difference between observed and expected values are significantly different (Heiberger & Holland, 2015, p.149). We used the test to evaluate if our peak and valley survival data were Poisson distributed. The null hypothesis H_0 is that the data follows the Poisson distribution, and the alternative hypothesis H_a is that the data does not follow the Poisson distribution. The number of colonies in all quadrats were recorded and binned. These were our observed values. The expected values were found from a theoretical Poisson distribution generated using the mean number of colonies from the observed values. χ^2 is found using the sum

$$\chi^2 = \sum_{i=0}^k \frac{(E_i - O_i)^2}{E_i},$$

with k being number of possible categories (1 colony, 2 colonies etc.), E being the expected values and O being the observed values. From the χ^2 distribution with degrees of freedom k - 1 we found the p-value.

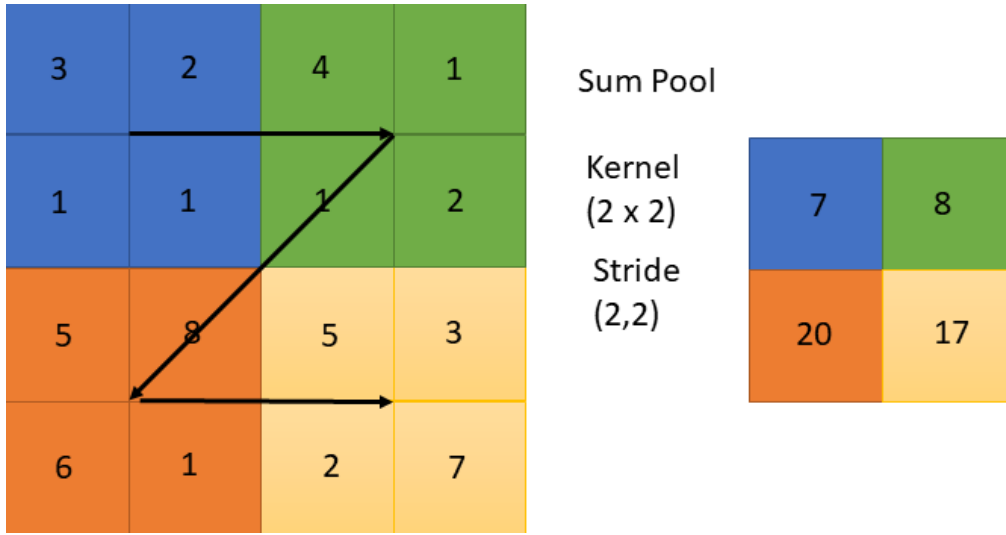


Figure 2-17. Sum pooling, with a 2×2 kernel moving in 2×2 strides across the image, summing up the pixel values within the kernel. The arrows indicate the movement of the kernel.

2.4.3.2 Poisson Regression

For the Poisson regression itself, we chose the Generalized Linear Models (GLM) from the *statsmodels* module (Seabold & Perktold, 2010). GLM takes the response data \mathbf{y} and the explanatory data \mathbf{X} . We chose to split the data into training and test (80/20 split). The training data were stacked together, to generate a model suitable for all irradiation scenarios: OPEN field, GRID stripes and GRID dots survival data. The test data were kept separate for model evaluation, which we will explain further in 2.4.3.5. Input data passed to GLM needs to have the same shape as for OLS in 1D survival 2.4.2. GLM also takes a family class. The family class provides the link function and the mean-variance relationship. We will of course use the Poisson family for our Poisson regression. After fitting the data, the GLM returns the estimated coefficients for our explanatory variables, and numerous statistical quantities. Comparing the 2D analysis to the 1D band analysis was not straightforward, because band analysis draws survival profiles along the length of the colony map and compares the profile with predicted survival from a LQ model fitted to OPEN field survival data, while the 2D analysis splits the flask into quadrats where the positions of said quadrats within the colony map are unknown. We therefore found a way to compare the peak and valley survival with predicted survival from a Poisson regression model fitted to the OPEN field survival data with dose and dose squared as explanatory variables. It was yet again necessary to define the peak and valley doses. The definition was chosen to allow variation. Peak was now defined as being doses above 70% of

maximum, while valley was defined as doses being below 130% of minimum. The quadrats were separated into their respective category, before the mean SC was found with standard error.

These would act as the observed data, to be compared to the predicted data.

We wanted to expand the model and include explanatory variables that could possibly explain difference in survival of GRID compared to OPEN field irradiated cells. We first incorporated the peak area ratio (see below). The aim was that the ratio could describe degree of cell killing caused by different GRID configurations. Second, we incorporated the distance from a quadrat to the nearest peak. This distance might explain the bystander effects occurring between the cells. When introducing new explanatory variables, we tested for multicollinearity. Multicollinearity is significant correlation between the explanatory variables making them incapable of independently predicting the dependent variable (*Collinearity / Statistics / Britannica*, 2013). Multicollinearity also has a tendency of increasing the estimated coefficients' standard error, thereby decreasing the precision of the estimates (Alin, 2010).

2.4.3.3 Peak area ratio

For both striped and dotted GRID we measured the area positioned underneath the grid opening, called peak area. Using a caliper and one irradiated EBT3 film, we were able to measure the area of the stripes appearing in the films to calculate the peak area (measurements in Figure 2-18).

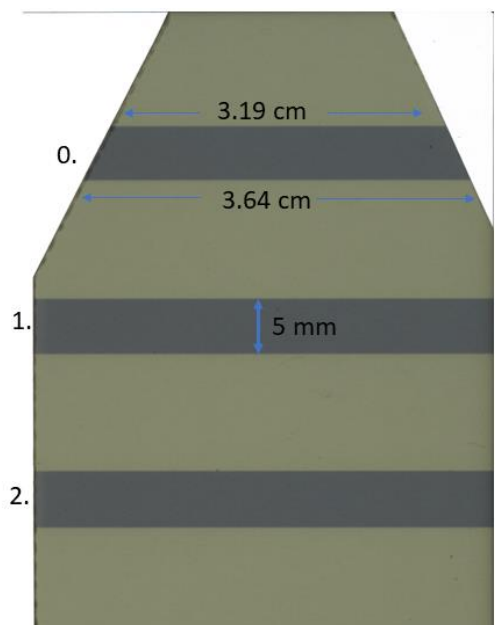


Figure 2-18. Caliper measurements on irradiated EBT3 film. Every peak is marked with a number.

However, poor cutting accuracy caused this area to be slightly different for all films and did not perfectly represent the peak area of the irradiated cells. For peak 3 we assumed the same area as peak 1 and 2; $4.3 \cdot 0.5 = 2.15 \text{ cm}^2$. This resulted in the total area for peak 1, 2 and 3 of $3 \cdot 2.15 = 6.45 \pm 0.01 \text{ cm}^2$. Peak 0 had a trapezoidal shape, with the area of $\frac{3.19+3.64}{2} \cdot 0.5 = 1.7075 \pm 0.0004 \text{ cm}^2$, which results in a total peak area of approximately $8.16 \pm 0.01 \text{ cm}^2$. The total peak area was divided by the total area of the bottom of the cell flask (25 cm^2) to obtain peak area ratio (PAR).

Uncertainties were found using the error propagation in equation 2-3, with the assumption of no uncertainty in the

width of the grid slits and the uncertainty of the caliper being 0.001 cm. For dotted GRID the peak area ratio was found by multiplying the number of holes within the irradiated films, of which there were 7, with the area of the holes. The holes have a diameter of 5 mm, resulting in a peak area of $7 \cdot \pi \left(\frac{0.5}{2}\right)^2 = 1.37 \text{ cm}^2$. No uncertainties were estimated because no caliper measurements were needed. For OPEN field all area would be within a “peak”, and PAR was therefore 1. The control films were not irradiated; hence they are neither peak nor valley and the PAR was set to 0. In Table 2-3 we see the PARs for all irradiation configurations.

Table 2-3. PAR measured from a striped and dotted GRID irradiated EBT3 film using a caliper to estimate the area of the peaks seen in Figure 2-18.

	Dots	Stripes	Open	Control
Peak area ratio	0.05	0.3264 ± 0.0005	1	0

2.4.3.4 Peak distance estimation

An algorithm was made to loop over each quadrat and find the distance to the nearest peak. The code can be found in the Appendix, section 7.3. Note that kernel_size is the length of the sides of the quadrats converted to pixels.

Peaks were identified with contour lines. To exclude sporadically occurring high intensity pixels, which did not constitute peak doses, we only included lines surpassing 500 pixels. The two loops are iterating over rows (y-axis) and columns (x-axis) in the pooled image, jumping from quadrat center to quadrat center. For all centers the algorithm searches for the smallest Euclidean distance between the center and the peak contour lines and stores them in a matrix with the same dimension as the pooled image. If the center is positioned within a peak, then the distance is set to 0. Because we are iterating over the coordinates of the quadrat centers, the indexes i do not follow 0, 1, 2 etc. but rather $\sum_{k=0} (\frac{\text{kernel_size}}{2} + \text{kernel_size} \cdot k)$. In the case of a $3 \times 3 \text{ mm}^2$ quadrat converted to 141×141 pixels for a 1200 dpi image, the indexes i become 70, 211, 352 etc. One cannot index the distance matrix using these values, it was therefore necessary to find a general expression to downscale the indexes, so they became 0, 1, 2 etc. For even quadrat pixel sizes, we could subtract the index with integer divided quadrat size following $i - \frac{\text{kernel_size}}{2}$. For odd quadrat pixel sizes, we used the formula

$$i - \frac{\text{kernel_size}}{2} \cdot \text{odd_i},$$

where odd_i increases with one each iteration (1,3,5 etc.). The resulting distance measurement are illustrated in Figure 2-19.

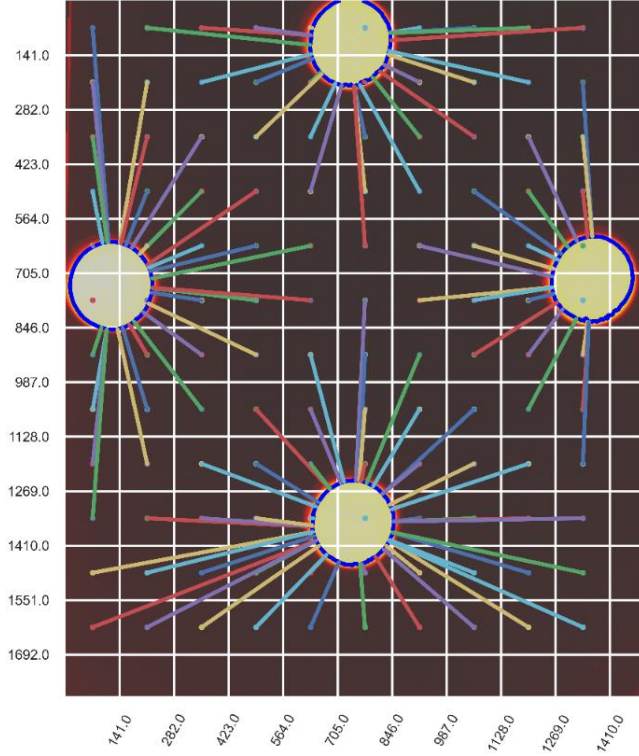


Figure 2-19. Illustration of nearest peak distance for all quadrats of size $3 \times 3 \text{ mm}^2$ with dotted GRID configuration. The distances of quadrats with center located inside a peak, are set to zero.

2.4.3.5 Model Evaluation

A χ^2 test was performed to provide the first indicator of goodness of fit. *Statsmodels* provide the χ^2 value, and we could use the cumulative distribution function from the *scipy.stats* library to calculate the p-value. Introducing more explanatory variables might lead to a better result but making a more complex model might lead to overfitting. The opposite problem occurs if not sufficient complexity is introduced. Overfitting and underfitting are illustrated using polynomial fitting in Figure 2-20.

Akaike information criteria (AIC) is a model selection metric that represents the tradeoff between overfitting and underfitting, and is found using the expression (Burnham & Anderson, 1998, p.47)

$$AIC = 2k - 2 \ln \hat{L},$$

where \hat{L} is the likelihood (see maximum likelihood function 1.6.2) when the algorithm reaches convergence (or maximum iterations have been reached). $-2 \ln \hat{L}$ tends to shrink when introducing more explanatory variables. k is the number of estimated parameters increasing the AIC score, thereby penalizing inclusion of additional parameters. A small AIC is desired, but evaluating a model using AIC alone is not fruitful, as AIC increase with sample size (Burnham & Anderson, 1998, p.55). However, if two models are curated from the same dataset, we can use AIC to find the model that strikes the best balance between complexity and generality. AIC values were extracted from the GLM model.

The model was also evaluated based on how well it predicted survival \hat{y} of the test data. For all irradiation configurations, including control, we found the MSE. Thus, we could test if the model predicted certain categories better than others. Separation of training and test data is a highly used method of assessing overfitting in machine learning. The fitting parameters are found for the training data, before testing the model on the test data. This ensures that the model works even when being exposed to unknown data.

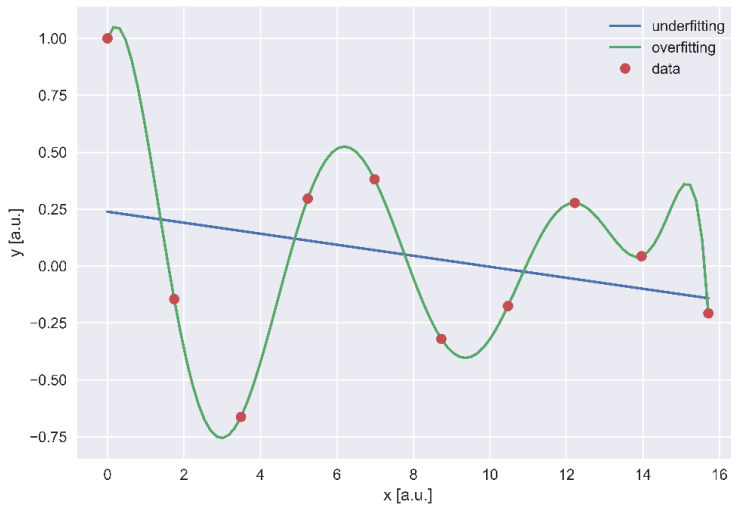


Figure 2-20. Overfitting vs underfitting of data. The Straight blue line fits the data using a one-degree polynomial (underfitting), while the green line fits the data using a tenth-degree polynomial (overfitting).

3 Results

3.1 X-ray dosimetry

X-ray dosimetry was necessary to have a known radiation field when calibrating the EBT3 films.

Two calibrations were performed: one for striped and dotted GRID. The methodology was the same, except for three repeated measurements being made in the first calibration versus four in the second. We therefore decided to only include the most important results from the second calibration. Table 7-1 shows the charge output (nC) from all four cell flask positions for both calibrations. The low dose regression plots for 5, 10, 15 and 20 second exposure times can be seen in Figure 3-1 with the associated R^2 .

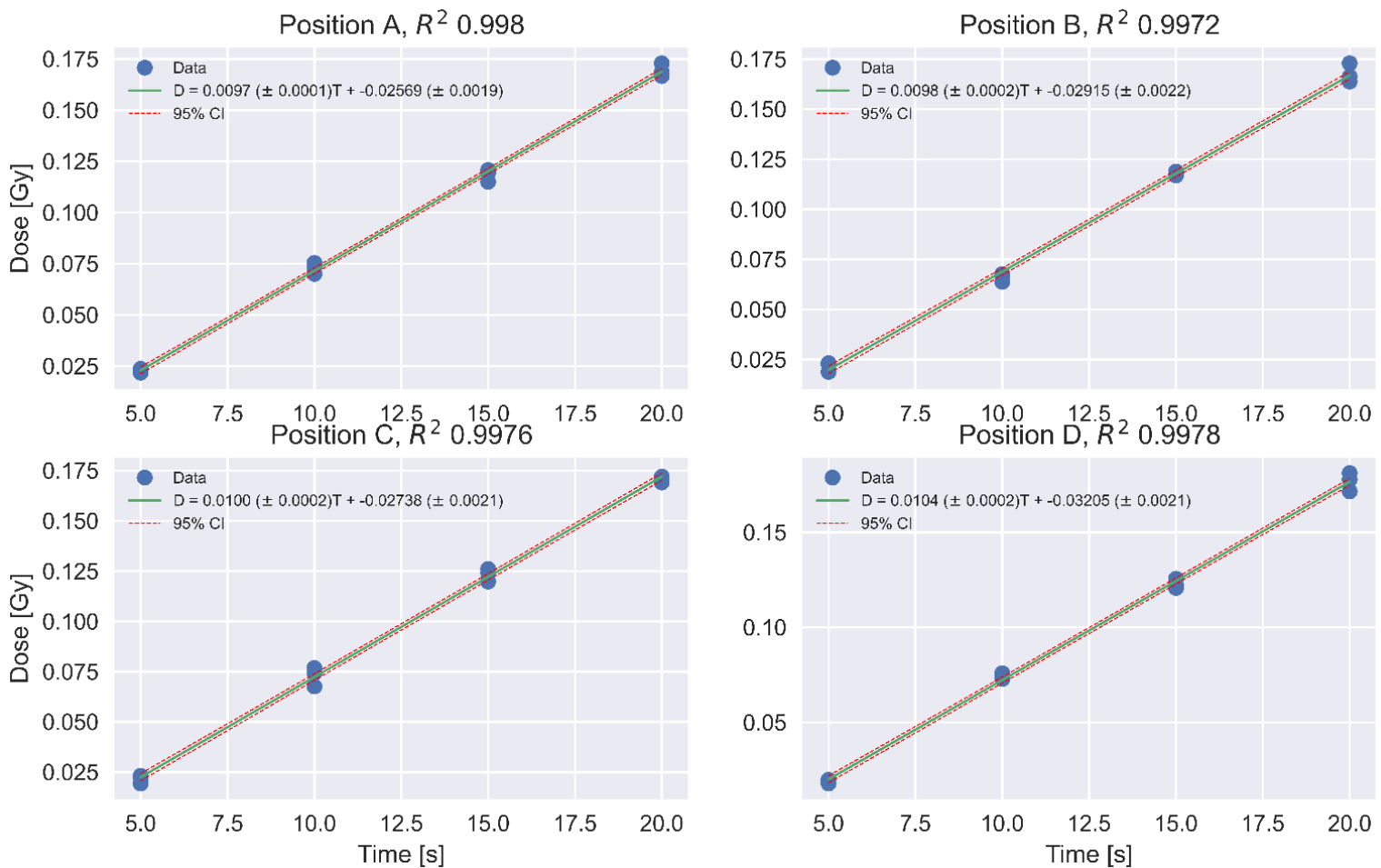


Figure 3-1. Regression lines generated from the ionization chamber output irradiated in all positions of the cell flasks holder, with R^2 .

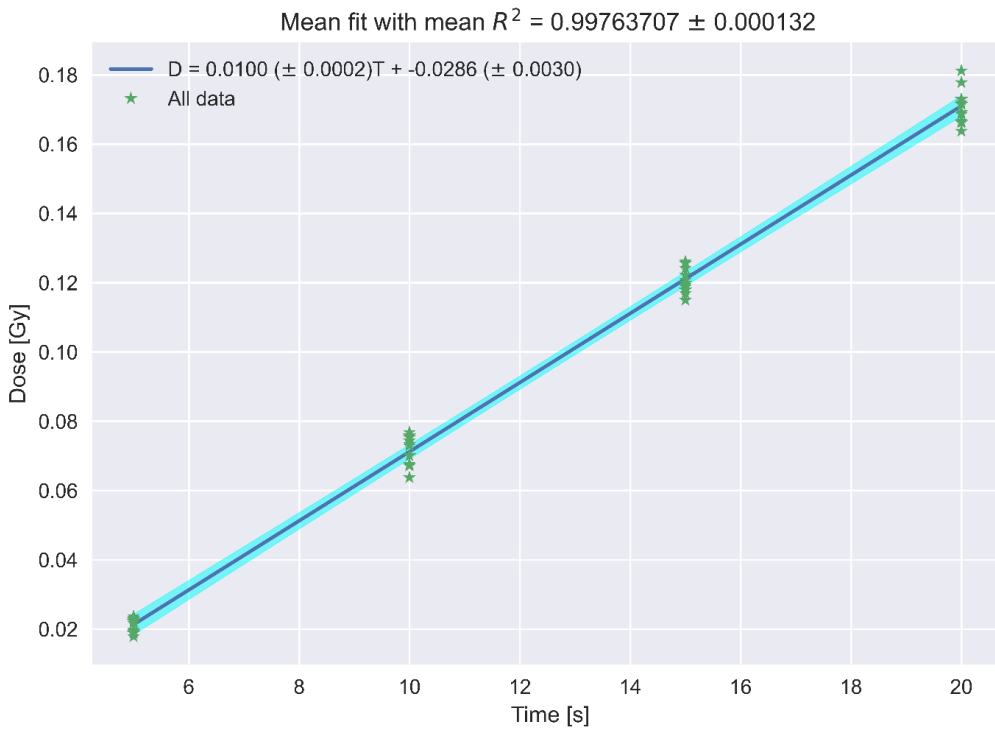


Figure 3-2. Mean fit generated from four regression lines (see previous plot) for all positions (A,B,C,D) of the cell flask holder.

The mean fit in equation 3-1 below represented the linear relationship between exposure time T [s] and dose [Gy] for low doses, with a measured R^2 of 0.9976 ± 0.0001 seen in Figure 3-2

$$\hat{D} = 0.010 \pm 0.0002 \text{ [Gy/s]} \cdot T \text{ [s]} - 0.029 \pm 0.003 \text{ [Gy]}. \quad 3-1$$

Rearranging equation 3-1 for time T and inserting $D = 0$, we measured a ramp-up time of 2.9 seconds. Converting the dose rate from [Gy/s] to [Gy/min] we got

$$\dot{D} = 0.60 \pm 0.01 \text{ Gy/min}$$

For doses higher than 0.5 it was assumed that a steady production of X-ray was reached, and the negative intercept's impact on dose could be neglected. From 60 second measurements we found a dose rate of $\dot{D} = 0.59 \pm 0.02 \text{ Gy/min}$.

On the second calibration we obtained a mean fit of

$$\hat{D} = 0.0102 \pm 0.0002 \text{ [Gy/s]} \cdot T \text{ [s]} - 0.031 \pm 0.002 \text{ [Gy]}. \quad 3-2$$

The 60 second measurements resulted in a dose rate of $\dot{D} = 0.60 \pm 0.02 \text{ Gy/min}$.

Exposure times necessary to achieve 0.1, 0.2, 0.5 Gy was found using the mean fit equations 3-1 and 3-2 (accounting for non-zero intercept), while doses above 0.5 Gy was found using the dose rates. All doses were multiplied with the correction factor 1.026, correcting for the height difference between the ionization chamber's sensitive volume and the EBT3 films positioned on the bottom of the cell flasks. The exposure times for both calibrations can be found in Table 7-2.

3.2 GafchromicTM film dosimetry

The calibration films were given 0.1, 0.2, 0.5, 1, 2, 5 and 10 Gy using the exposure times from Table 7-2. We wanted to evaluate if the light from the scanner affected the response of the films. Therefore, four scans were made and the RPD between the pixel values of all four scans was found. The mean RPD for all films is shown in Figure 3-3. The maximum difference was \approx 0.1%, with the majority being in the 0.01 – 0.03 % range.

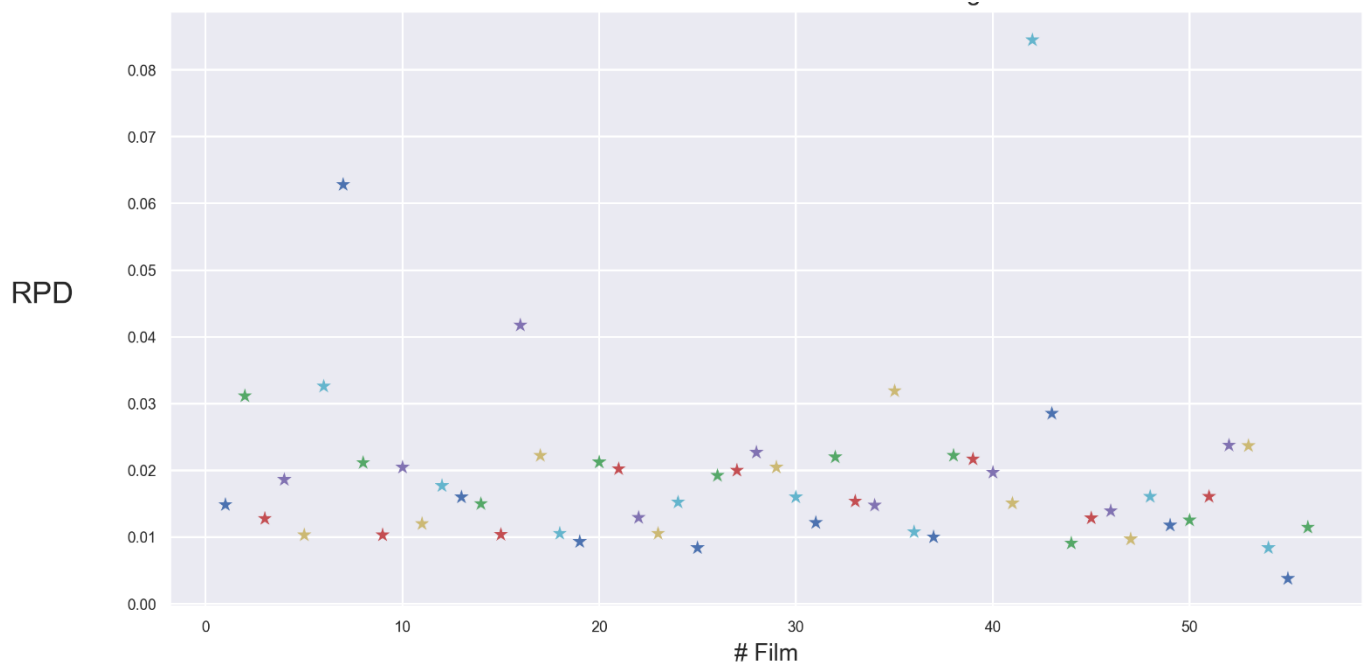


Figure 3-3. Mean RPD between the pixel values of 4 scans of the same EBT3 film, to evaluate if the scanner affected the response of the films.

The pixel values of all the calibration films were converted to netOD using equation 2-4. Even though all color channels were calibrated and their dose response was established, only one color channel was chosen to measure the dose received by the measurement films. Sensitivity to irradiation was one of the criteria, and Figure 3-4 showed that GREEN and RED channel

exhibited the highest sensitivity, although it was hard to detect the difference. Figure 3-5 was made for easier comparison between the channels. Both GREEN and RED channel exhibit superior separation of the netOD values for different doses, but RED color channel had a slightly higher sensitivity.

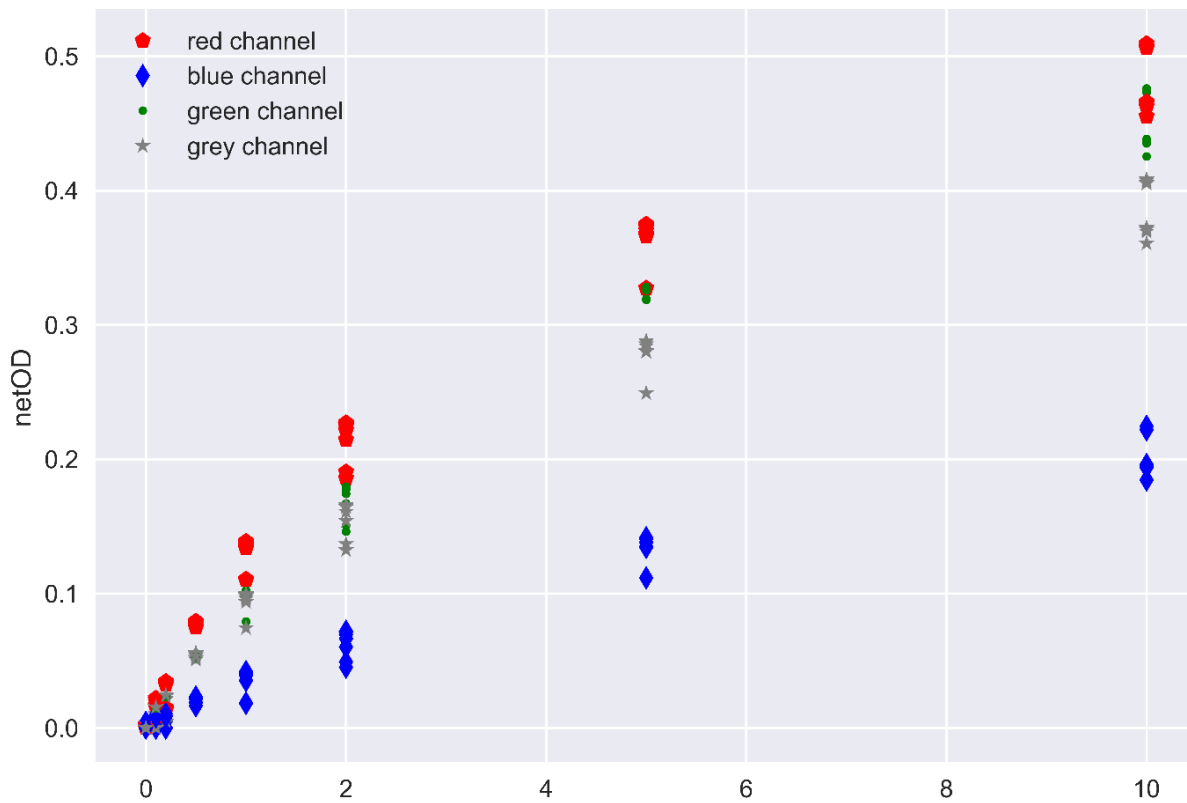


Figure 3-4. NetOD of all EBT3 calibration films for all color channels calculated using equation 2-4. One color channel was to be chosen for fitting of the dose model $D(\text{netOD})$. Two different responses were found within one batch of films, which can clearly be seen for doses above 0.5 Gy.

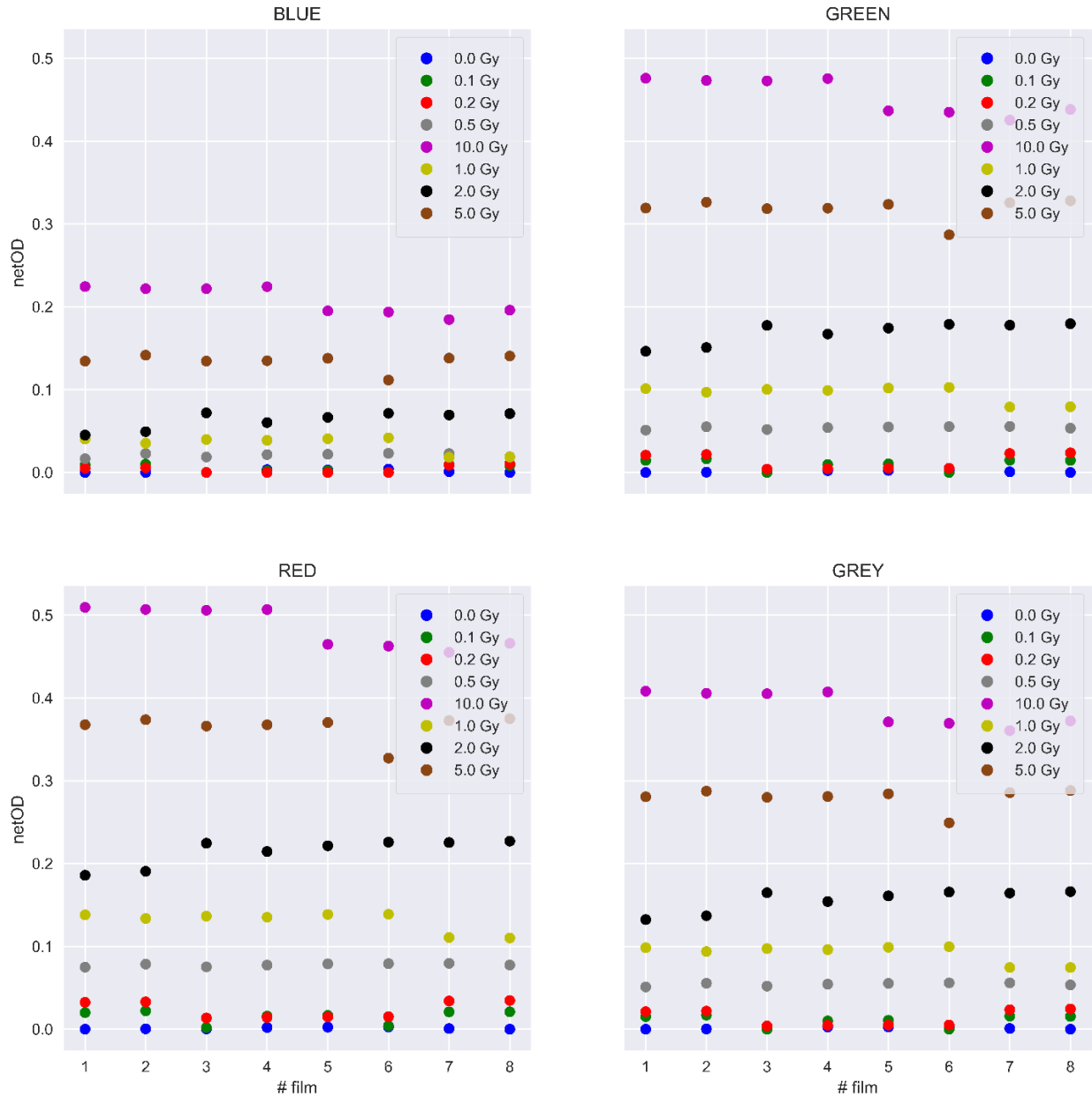


Figure 3-5. NetOD found using equation 2-4 of all films for all doses and all color channels. There were eight films per dose.

The last criterium for choosing color channel was the goodness of fit quantity MSE found after fitting equation 2-6 with non-linear regression. MSE was also used to find the optimal ROI size. The results can be seen in Table 3-1. Because of a split in film response, the films were separated into low and high responding films before being fitted, and the MSE of high and low response films was summed. The optimal protocol thus proved to be a combination of a $3 \times 3 \text{ mm}^2$ ROI and RED color channel.

Table 3-1. MSE found after non-linear fitting of equation 2-6 for different color channels and ROIs. The values are separated into high and low, because of the film-to-film variation. The combination of color channel and ROI size giving the lowest total MSE is marked in orange.

MSE (Low + High)	ROI (mm ²)		
Color channel	2 x 2	3 x 3	4 x 4
BLUE	0.0428	0.0441	0.0431
GREEN	0.163	0.0160	0.0163
RED	0.127	0.0122	0.0124
GREY	0.194	0.0190	0.0193

Figure 3-6 shows the RED channel netOD data for high and low response with the associated regression line. The fit was based on 42 high response films and 22 low response films and resulted in the following dose models

$$\widehat{D}_{high} = 6.2 \pm 0.2 \cdot netOD + 51 \pm 1 \cdot netOD^{2.96 \pm 0.05} \quad 3-3$$

$$\widehat{D}_{low} = 7.3 \pm 0.9 \cdot netOD + 51 \pm 6 \cdot netOD^{2.6 \pm 0.2}$$

The higher uncertainty of \widehat{D}_{low} compared to \widehat{D}_{high} was caused by the lower amount of low responding films, compared to the high responding films. An evaluation of the robustness of the model was done by giving the non-linear regression algorithm a set of random starting points as initial guesses for the fitting parameters a , b and n . The numbers were drawn from a normal distribution with $\mu = 0$ and $\sigma^2 = 1$. n had to be a positive value (section 7.5.2) shows the resulting parameters after fitting. Only once did the algorithm return a nonsensical result.

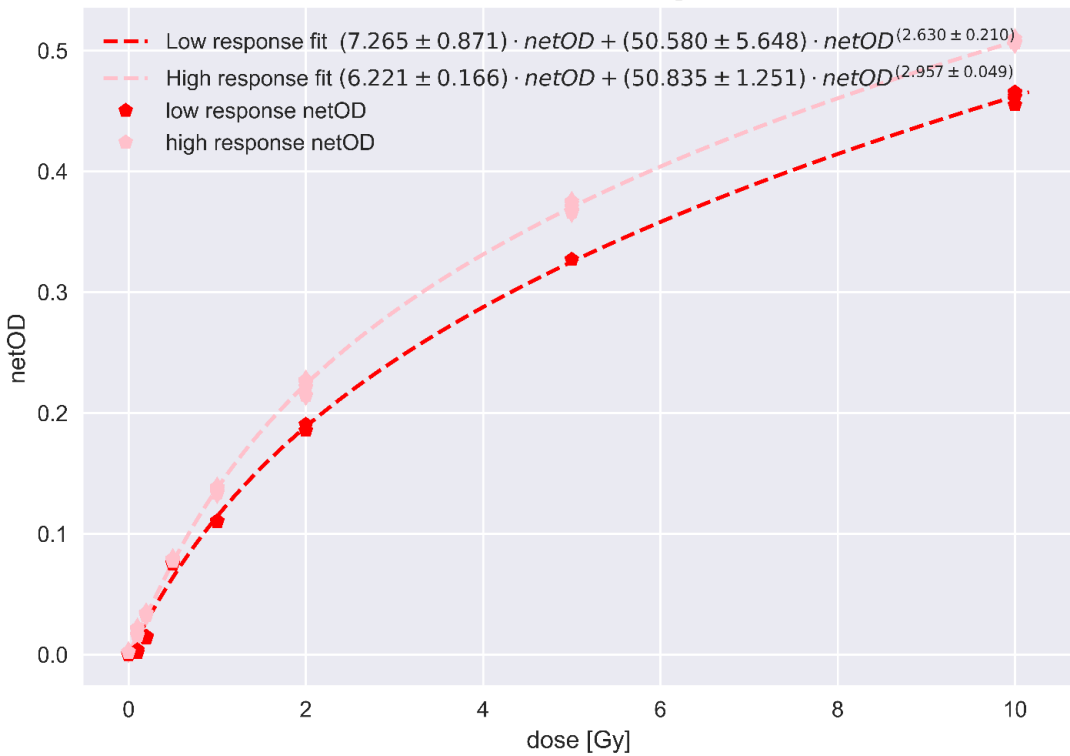


Figure 3-6. netOD data from the first calibration using the RED color channel. Two non-linear regression line was generated from equation 2-6, for high and low response EBT3 films, respectively.

The second calibration, with a lack of high and low response films for all doses, was not trivial. First the films were calibrated ignoring high and low split using the same ROI and color channel as the first calibration. The resulting fit can be seen in Figure 3-7 with a dose model of

$$\hat{D} = 4.2 \pm 0.6 \cdot \text{netOD} + 52 \pm 2 \cdot \text{netOD}^{2.34 \pm 0.09}. \quad 3-4$$

With an established model for dose as a function of netOD for both calibrations we measured the received dose in each pixel of the measurement films, generating dose maps. For OPEN field irradiated measurement films, there were 8 high and 8 low response films. For striped GRID irradiated films, the number was 11 high and 5 low response films, respectively. As mentioned, there was no clear separation for the dotted GRID calibration films, and all measurement films were converted to dose using equation 3-4. One dose profile was generated for each dose map and can be seen in Figure 3-8 and Figure 3-9, for striped and dotted GRID respectively.

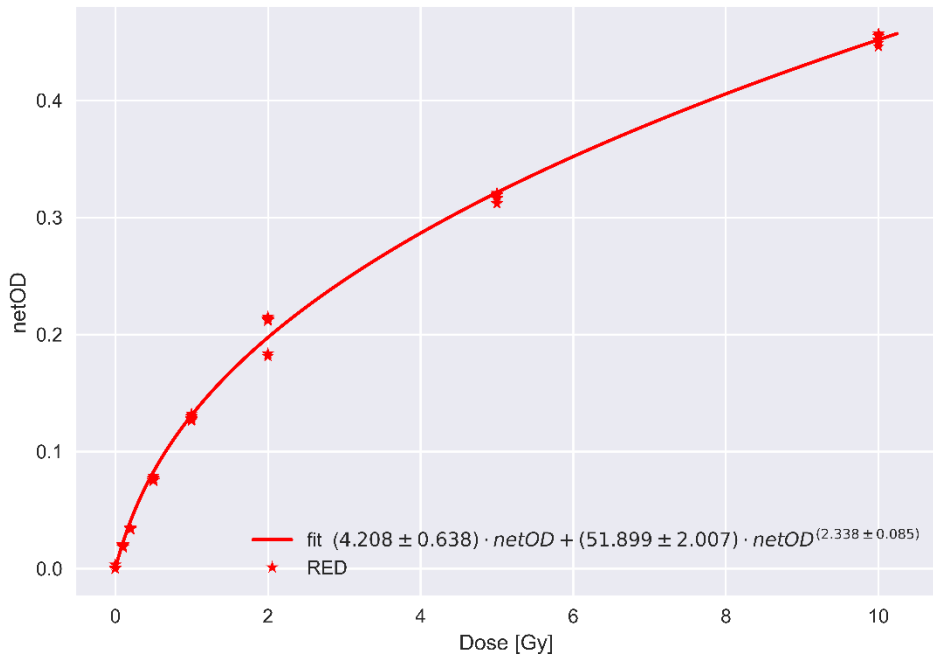


Figure 3-7. Data from the second calibration. netOD data with regression line for the RED color channel fitted using non-linear regression of equation 2-6. A split response can be seen for some doses, but not all.

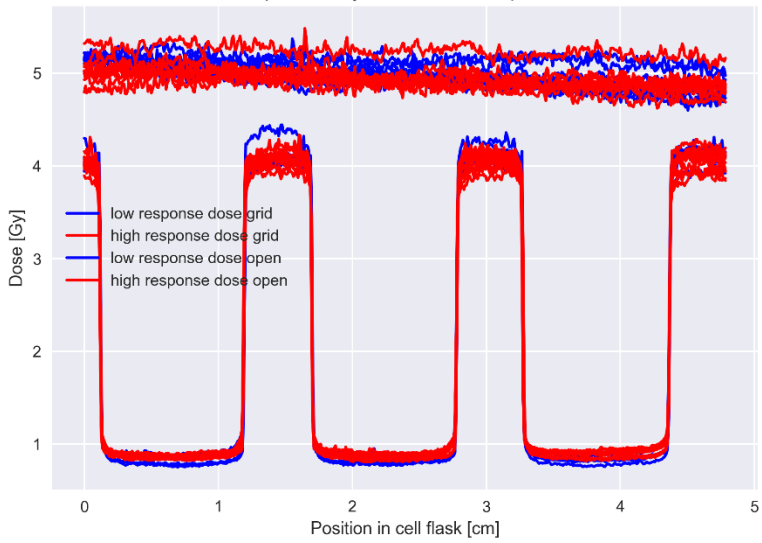


Figure 3-8. Dose profiles generated by finding the mean dose on each row in a mean dose map for OPEN field and striped GRID irradiated EBT3 films. The dose maps were generated by converting all pixels within a limited area of the measurement films to dose using either \bar{D}_{high} or \bar{D}_{low} from equation 3-3. Blue profiles were low response films, while red profiles were high response films.

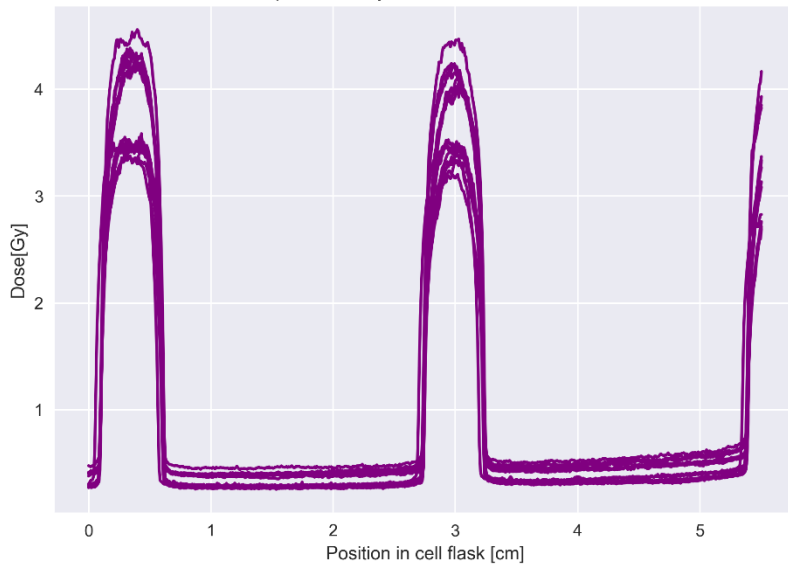


Figure 3-9. Dose profiles generated by finding the mean dose on each row in a mean dose map for dotted GRID. The mean dose maps were generated similarly as for striped GRID, but no separation of high and low response films were done.

For dotted GRID, ignoring the split in film response resulted in a split in the dose profiles seen in Figure 3-9. Thus, it was clear that also the films in this series of measurement films had two different sensitivities. The solution was therefore to separate the films, and use the fitting parameters obtained from the first calibration in equation 3-3. A new set of dose profiles were generated, which can be seen in Figure 3-10. This time there was a better match between the profiles.

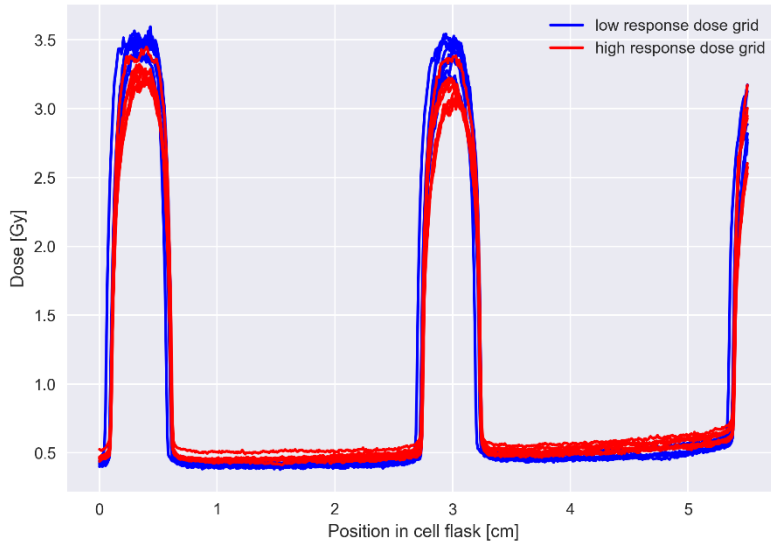


Figure 3-10. Dose profiles generated by finding the mean dose on each row in a mean dose map for dotted GRID irradiated EBT3 films. Blue profiles were low response films, while red profiles were high response films.

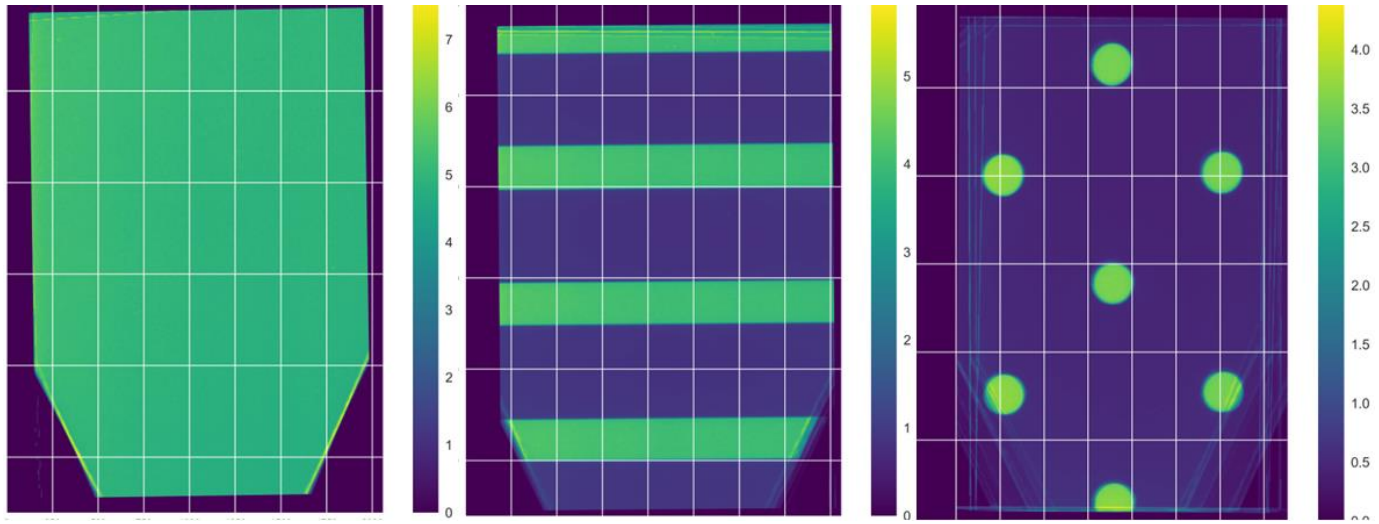


Figure 3-11. Mean dose maps for all irradiation configurations given 5 Gy nominally. The dose maps were generated by combining the high and low response measurement film that were registered to each other and converted to dose. The color bar represents the dose. Apparent dose spikes near the edges of the films were disregarded in the analysis.

One mean dose map was generated for all irradiation configuration, which can be seen in Figure 3-11. From these, one dose profile was generated for each irradiation configuration. These profiles can be seen in Figure 3-12 and Figure 3-13. The OPEN field profile was around 5 Gy, which was the dose we expected the measurement films to receive. The peak dose in striped GRID was slightly higher than the peak dose of dotted GRID, which was also the case for the valley doses. All GRID doses were lower than OPEN field doses.

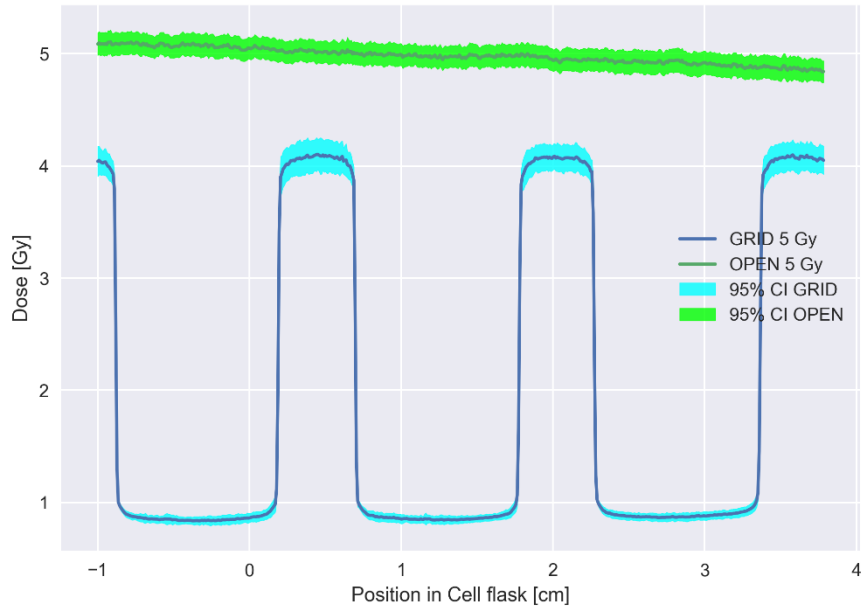


Figure 3-12. One mean dose profile found from the mean dose map generated from all 16 high or low response dose maps for OPEN field (green) and striped GRID (blue) irradiated EBT3 measurement films receiving 5 Gy nominally.

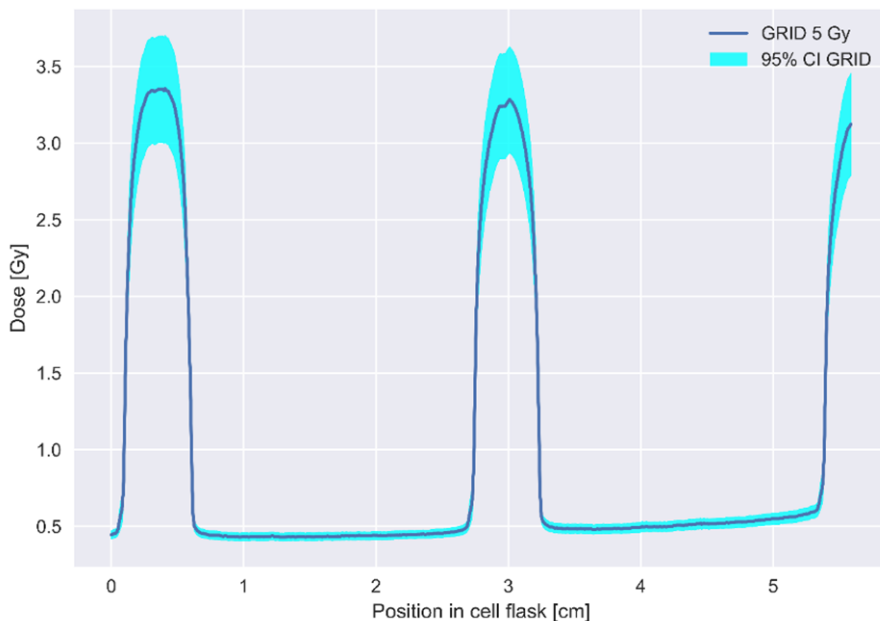


Figure 3-13. Mean dose profile found from the mean dose map generated from all 16 high or low response dose maps for dotted GRID irradiated EBT3 measurement films receiving 5 Gy nominally.

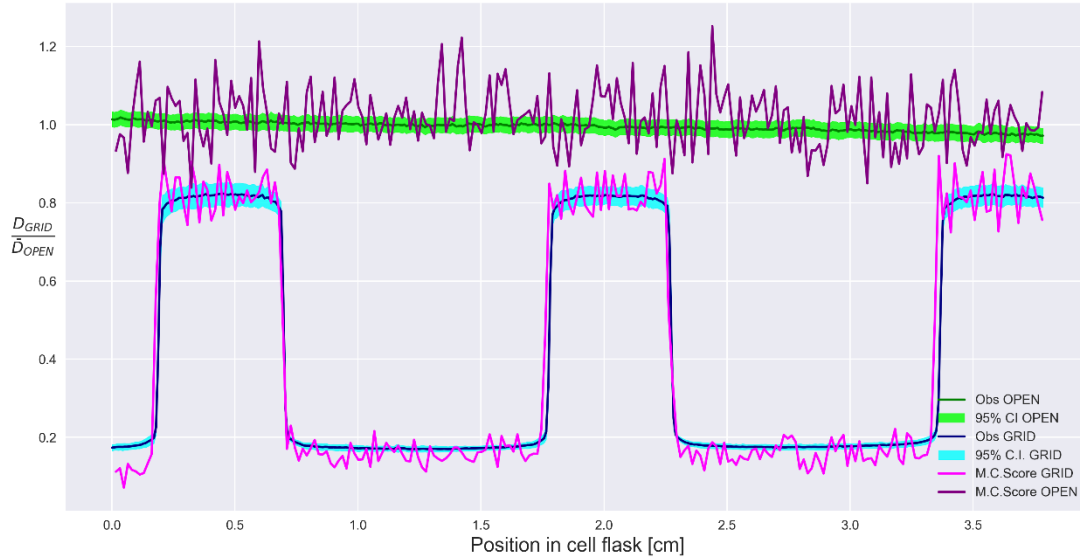


Figure 3-14. Mean dose profiles for GRID and OPEN field (from Figure 3-12) normalized to OPEN field dose. Monte Carlo simulated data was plotted over each profile for dosimetry validation.

Further evaluation of the dose profiles was done, by a comparison with MC simulated data. The MC data were normalized to an OPEN field. The comparison of MC and striped GRID can be seen in Figure 3-14. For OPEN field the MC data were relatively noisy with larger oscillations around the OPEN field dose profile. Smaller oscillations were found for the striped GRID MC data. One value of estimated dose was found for OPEN field, striped and dotted GRID in peak and valley areas. The values were found by averaging the relevant parts of the mean dose profile per irradiation configuration. As mentioned, peak was defined as doses above 95% of maximum dose, while valley was defined as doses below 115% of minimum dose. The results can be seen in Table 3-2.

Table 3-2. Mean dose values for OPEN field, striped and dotted GRID with 95% confidence intervals. Peak dose was defined as values above 95% of maximum dose. Valley was defined as values under 115% of minimum dose. The values were found as a mean of 16 dose profiles, both high and low response.

Open Field (95% C.I.)	Striped GRID (95% C.I.)		Dotted GRID (95% C.I.)	
	Peak	Valley	Peak	Valley
4.98(4.93,5.03)	4.04(3.98,4.16)	0.86(0.80, 0.87)	3.37(3.28, 3.45)	0.44(0.41, 0.45)

3.3 Cell survival

What data to use for survival analysis was chosen based on the similarity between the control flasks across the performed cell experiments. Figure 3-15 shows number of colonies counted as well as PE. The first two experiments (18.11 and 20.11) yielded the highest PE in the range of 8-10% and Table 3-3 shows that the control flasks from these two experiments were not significantly different (p-value 0.581).

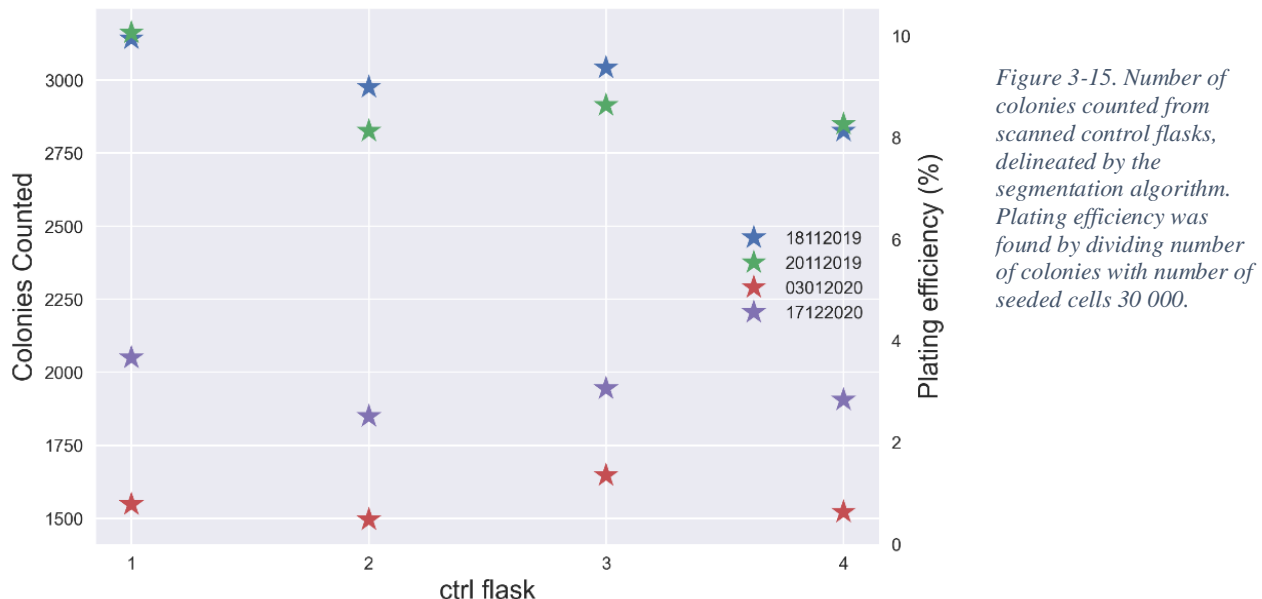


Table 3-3. Four cell experiments were performed where cell flasks were irradiated with OPEN field, striped and dotted GRID. The cell flasks were scanned and segmented to count the number of colonies within the flasks. An ANOVA test was performed between the control flasks to evaluate whether the number of colonies were significantly similar. The P-values from this test is seen in the third row.

	18.11.2019	20.11.2019	03.01.2019	17.12.2020
Mean counted colonies ctrl flasks	2996 ± 58	2937 ± 67	1553 ± 29	1936 ± 37
Anova p-value	0.581			0.0004

Following data acquisition, image registration was necessary to align the irradiated measurement films of each irradiation configuration to the cell flasks. Preprocessing steps were taken to increase the similarity between these images before the rigid body registration was performed. Following registration, the transformation matrix was applied on the mean dose map. Figure 3-16 shows all steps taken during registration. The top images show alteration of the films for increased similarities between reference cell flasks and dosimetry film. The bottom images show the match between the mean dose map and the reference cell flask before and after registration.

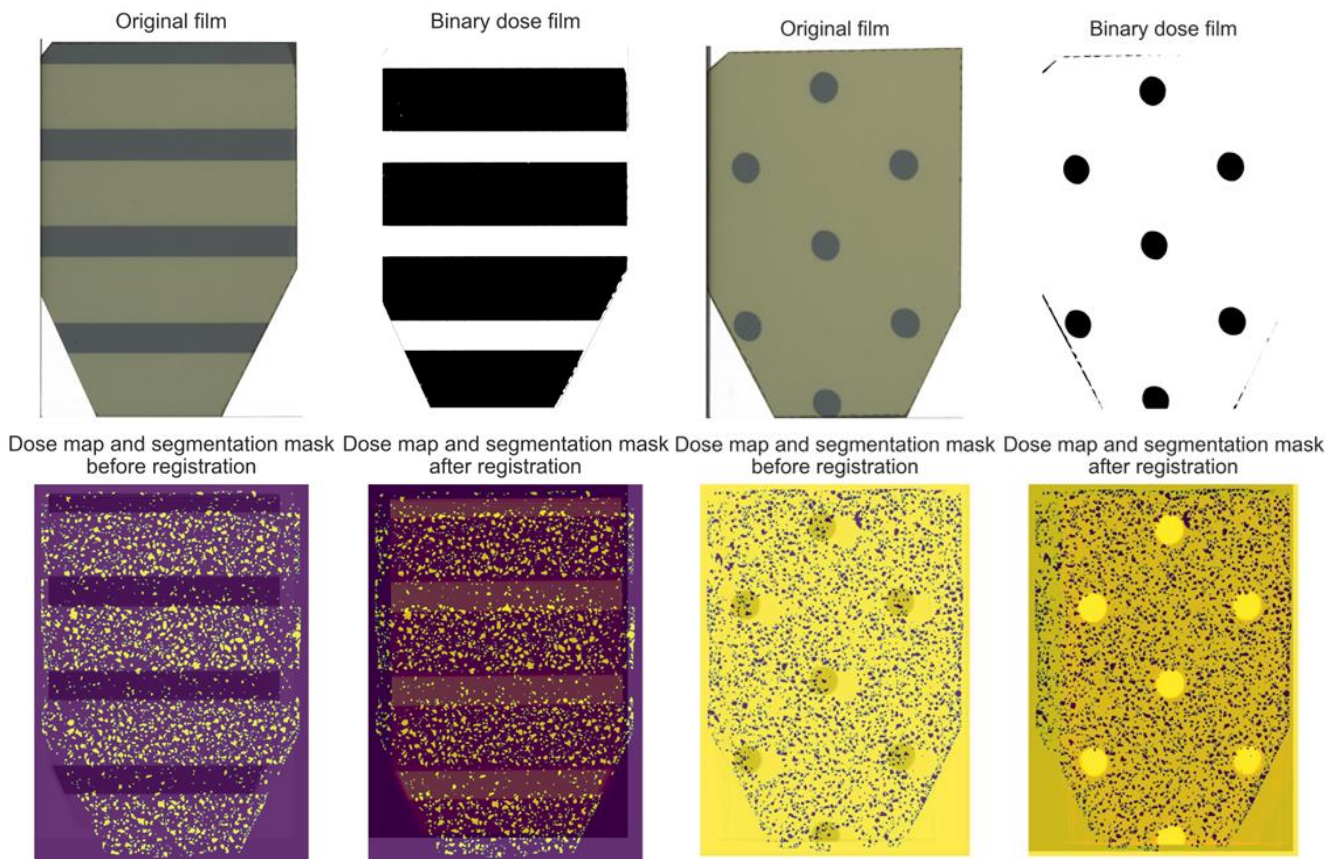


Figure 3-16. Preprocessing steps taken to match cell flasks and dosimetry films. First, edges were removed. Secondly, intensity values were changed to enhance similarities. Thirdly, Rigid Body registration. And lastly, small adjustments to transformation matrix for optimal alignment. All objects in this figure were irradiated with 5 Gy nominally.

3.3.1 1D survival analysis

3.3.1.1 LQ modelling

Fitting the OPEN field survival data resulted in the estimated α and β parameters given in Table 3-4, yielding an LQ model of $\log SF = -0.06D - 0.01D^2$, which we would use to estimate predicted survival when comparing OPEN field and GRID for equal dose. The α/β -ratio was $6 \pm 5 \text{ Gy}$. Figure 3-17 shows the log transformed SF data observed from the OPEN field irradiated cell flasks with a regression line. The reason for the large confidence interval at 10 Gy, was that the 10 Gy data were not included in the analysis and the regression line had to be extrapolated.

Table 3-4. Estimated fitting parameters from statsmodels OLS model, after fitting the log transformed LQ model to survival data normalized to control and log transformed.

	Estimate	Standard error	p-value
α	0.06	0.04	0.061
β	0.01	0.01	0.143

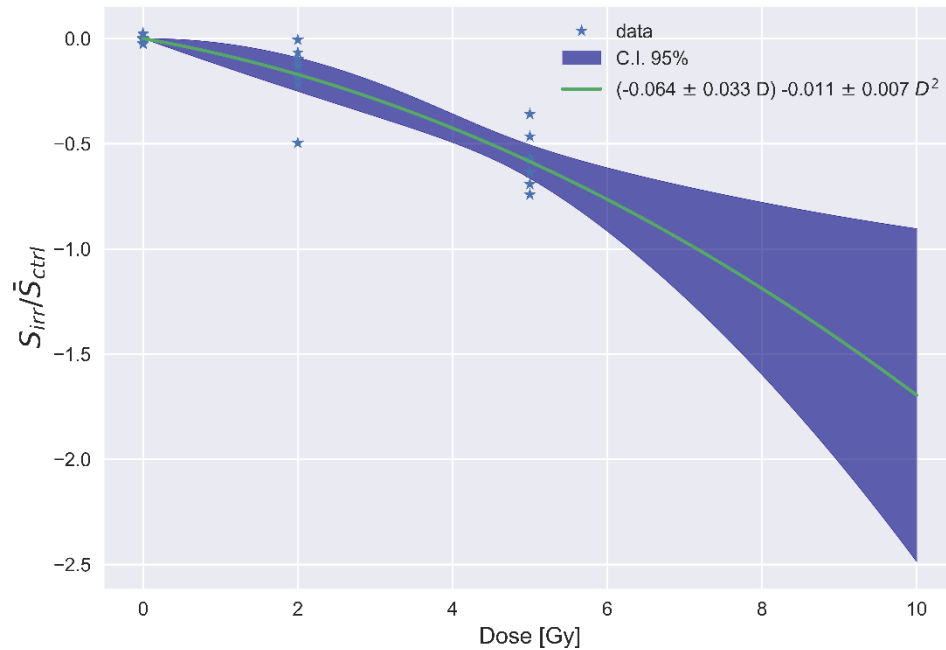


Figure 3-17. Fitting OPEN field survival data from segmented cell flasks to generate α and β values for the LQ-model. The large confidence band seen for doses above 5 Gy stem from the lack of 10 Gy survival data.

3.3.1.2 1D band analysis

Analysis of survival for striped GRID irradiated cell flasks was performed by dividing the colony maps into bands of equal width and summing the number of colonies within each band. Before band analysis could be performed, the number of colonies on each pixel row (y-axis) was found. All pixel rows did not have the same width, it was therefore necessary to weight them accordingly. Figure 3-18 shows how the weights were calculated based on the number of zeros on the binary image of the cell flask.

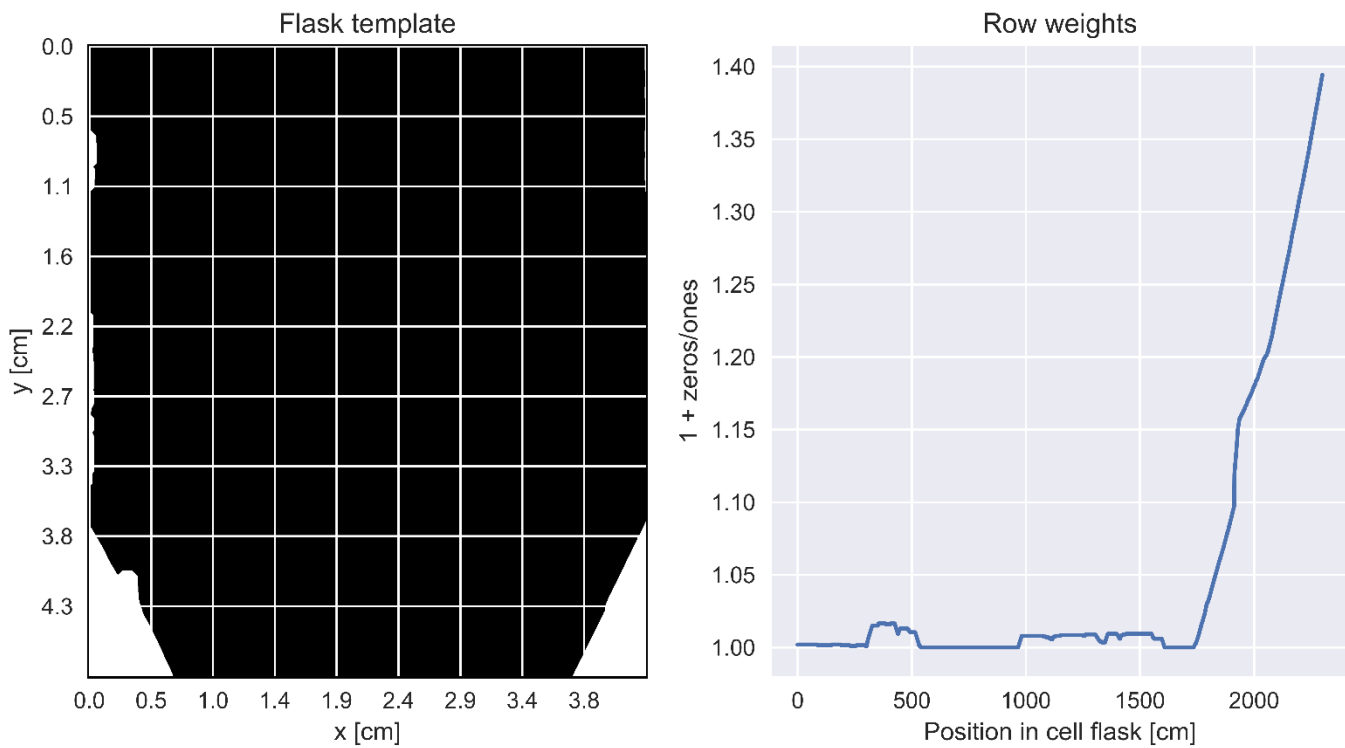


Figure 3-18. How each pixel row (y-axis) was weighted based on how many zeros there were on the row in the flask template (left) image. More zeros meant less area to grow colonies, hence increased weight. This seen in the right image, as the weight increases with vertical position.

The analysis was only performed for 1 mm bandwidth on cells irradiated with 2 and 5 Gy nominally to have comparative results to the 2D analysis, where $1 \times 1 \text{ mm}^2$ was deemed the optimal quadrat size (3.3.2). The number of colonies within each band was plotted as the observed values in the figures below. The predicted data were found by inserting the doses from the 5 Gy striped GRID dose profile (Figure 3-12) into the fitted LQ model from section 3.3.1.1. Observed and predicted survival together with the RPD between observed and predicted survival can be seen in Figure 3-19 for 2, 5 and 10 Gy respectively. All plots showed a decreased observed survival in the peak areas compared to predicted survival, albeit the pattern was clearer,

less noisy and had a narrower confidence band for predicted data for 5 Gy irradiated cells. The survival in valley was more or less the same as predicted.

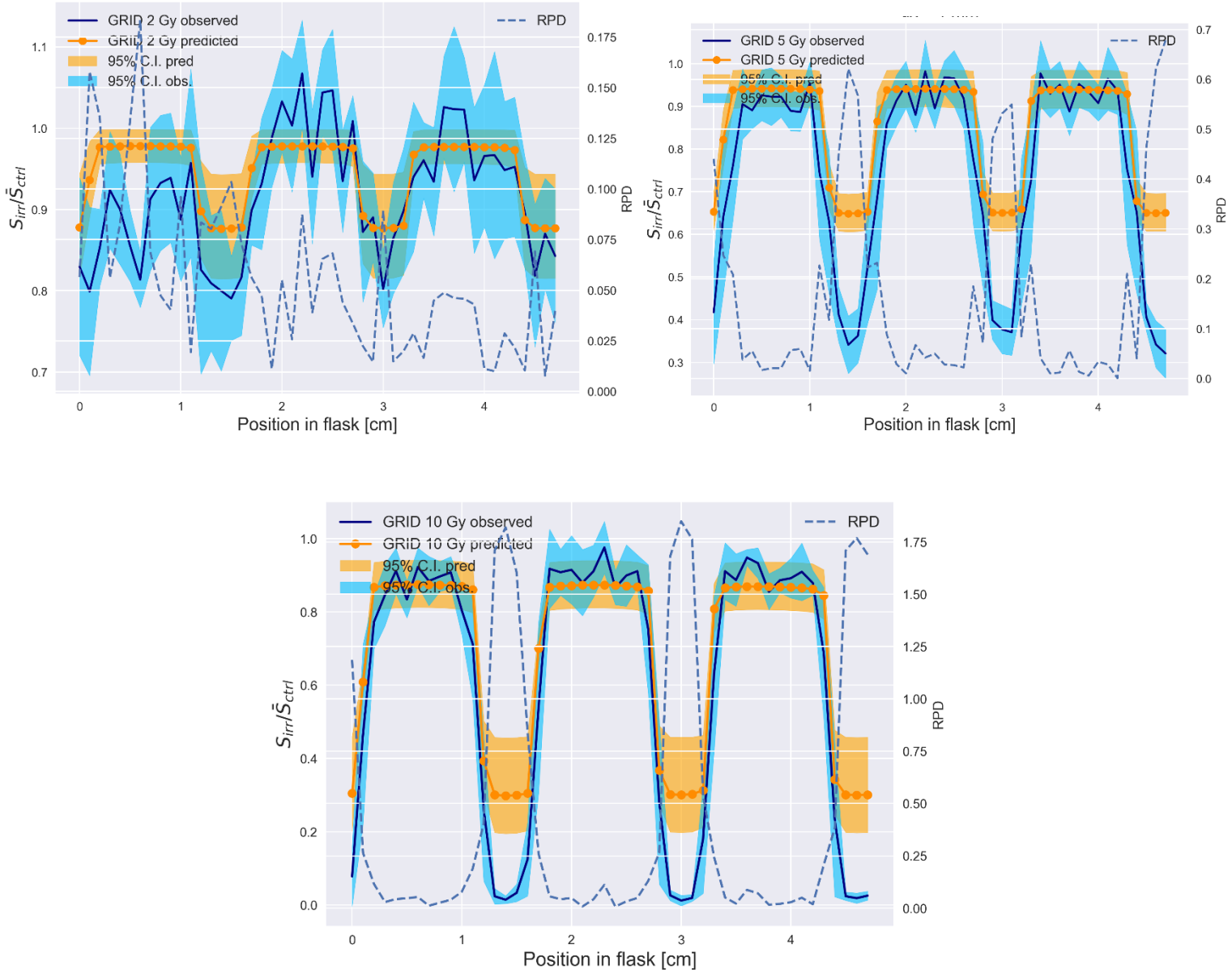


Figure 3-19. Combined caption for the figures above. The plots represent 2, 5 and 10 Gy band survival analysis using 1 mm wide bands. Predicted data was obtained using LQ model fitted to SF data from OPEN field irradiated cell flasks in orange vs observed in blue. Stippled line is relative percentage difference between predicted and observed.

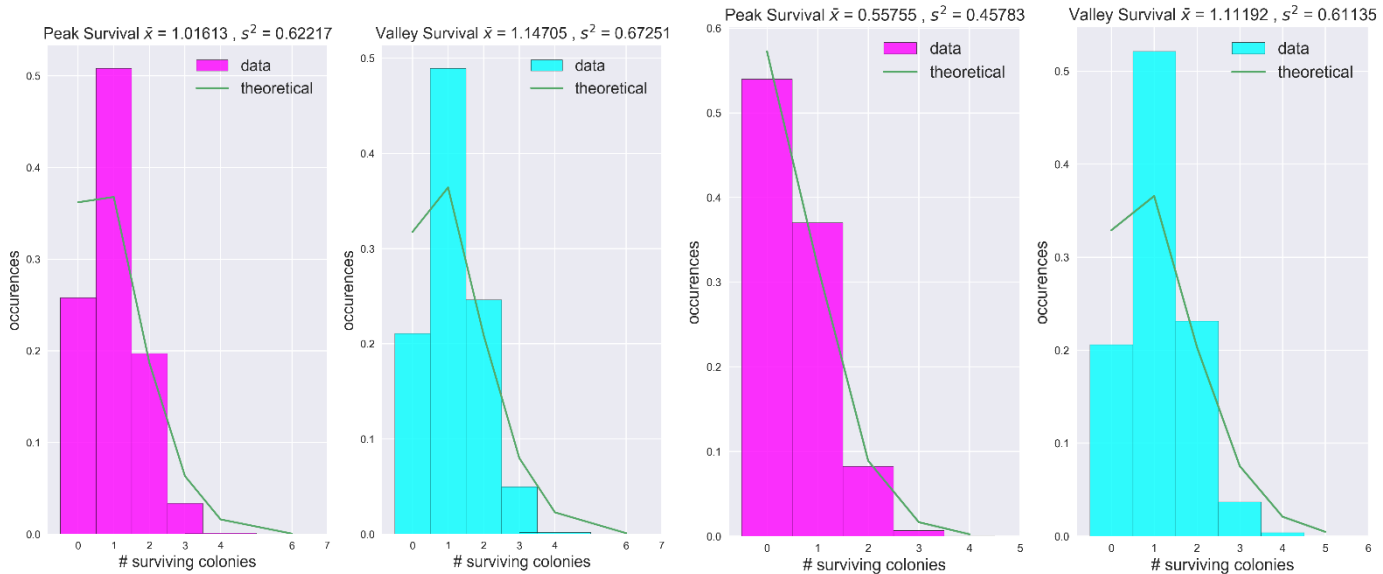
3.3.2 2D analysis

For the 2D analysis of the cell survival, we moved away from the band analysis, and divided the whole colony map into quadrats of equal size. The number of colonies and the mean dose within each quadrat was found and passed to the Poisson regression pipeline.

3.3.2.1 Evaluation of Poisson regression quality criteria

Before performing the Poisson regression, we evaluated the performance of different quadrat sizes. The first criterium was that the survival data in the peak and valley areas were Poisson distributed. RPDs between mean and variance were found for all quadrat sizes and doses.

Additionally, a χ^2 -test was performed to compare a theoretical Poisson distribution with the observed peak and valley survival data. Histograms were generated from the observed data and can be seen in Figure 3-20 with peak survival in the left subplots at valley survival in the right subplots, with increasing dose for each plot (2, 5 and 10 Gy nominally). The histograms generated from the remaining quadrat sizes can be seen in section 7.8. RPD and p-values can be seen in Table 3-5. A p-value > 0.05 meant that there was no evidence that the observed values did not follow the Poisson distribution. Quadrat sizes were also evaluated based on number of quadrats containing no colonies in the control flasks (zero inflation), as well as variance between quadrat doses. Figure 3-21 shows how all quadrat sizes impacted these quality criteria for nominally 5 Gy irradiated cells. Based on these results $1 \times 1 \text{ mm}^2$ quadrats were chosen.



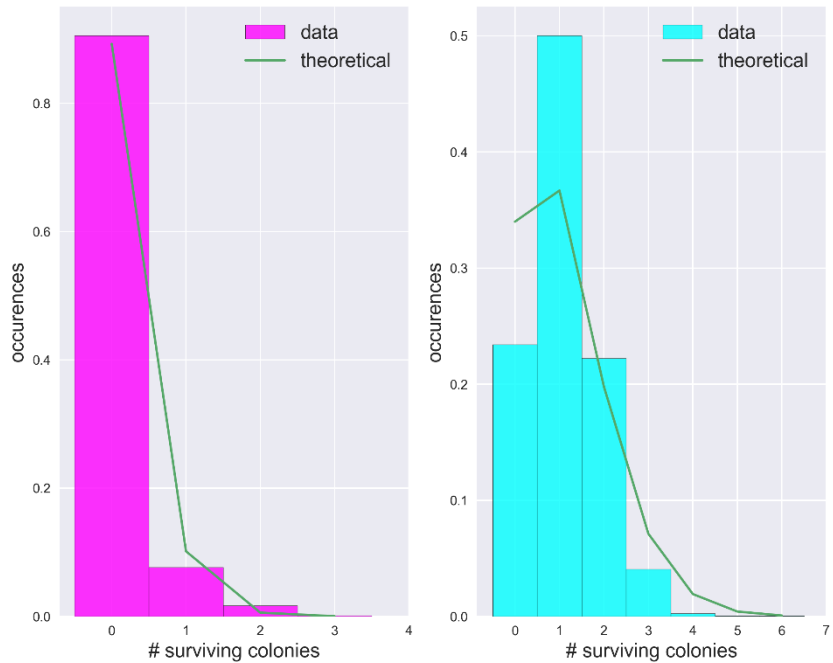


Figure 3-20. Combined caption for the three histograms. The histograms were generated by separation of striped GRID irradiated survival data separated into peak (left) or valley (right) category based on their received dose. The observed values are the number of counted colonies within the colony maps divided into $1 \times 1 \text{ mm}^2$ quadrats. The upper two plots represent survival data from 2 and 5 Gy irradiated cells, while the lower plot represents 10 Gy irradiated cells. A theoretical distribution was generated from the mean of the observed data.

Table 3-5. RPD between mean and variance of survival data in either peak (above 70% max dose) or valley (below 115% min dose) dose category for all quadrat sizes and nominal doses. P-values were found by performing χ^2 -tests between observed and expected occurrences of counted colonies for $X \times X \text{ mm}^2$ quadrats, with null hypothesis being that there were no significant differences between the theoretical Poisson distribution and the observed distribution.

	2 Gy				5 Gy				10 Gy			
	Peak		Valley		Peak		Valley		Peak		Valley	
Quadrat sizes	RPD	p-value	RPD	p-value	RPD	p-value	RPD	p-value	RPD	p-value	RPD	p-value
0.5	0.06	0.99	0.07	1	0.03	1	0.08	0.98	0.01	1	0.99	0.99
1	0.12	1	0.14	1	0.05	1	0.16	1	0.054	1	0.17	1

2	0.12	1	0.14	1	0.02	1	0.17	1	0.15	≈ 0	0.18	5	1
3	0.10	1	0.13	1	0.01	1	0.17	1	0.23	≈ 0	0.16	9	1
4	0.12	1	0.14	1	0.03	1	0.14	1	0.14	1	0.07	6	1

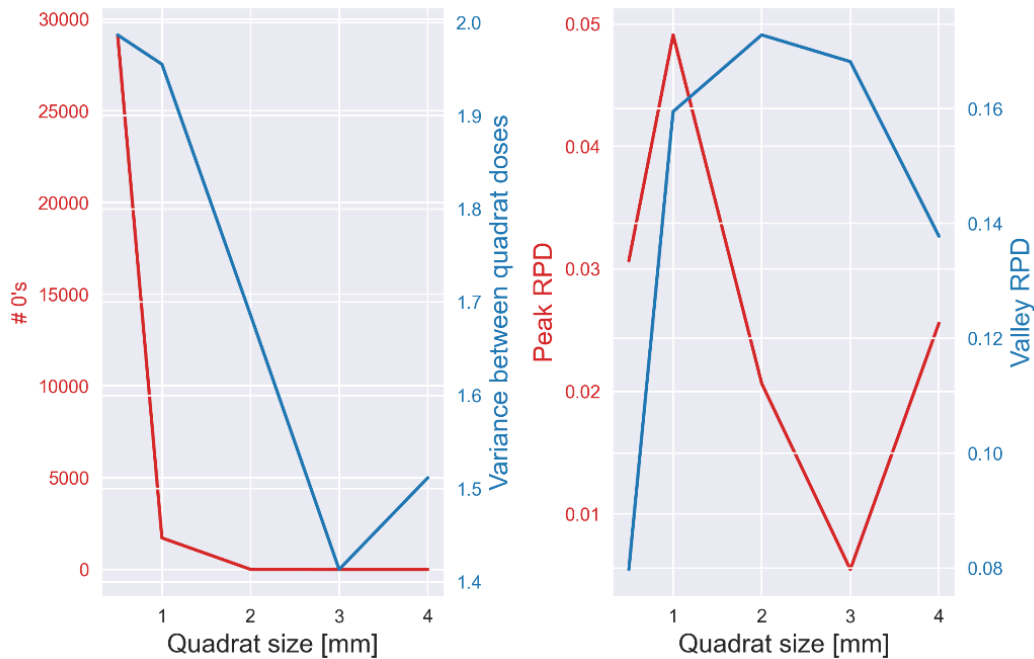


Figure 3-21. Evaluation of the impact of quadrat sizes on quality criteria for subsequent Poisson regression for 5 Gy striped GRID irradiated cells. Quality criteria were number of quadrats in the control flasks containing 0 colonies to mediate zero inflation, variance between the doses of each quadrat to mediate smoothing of doses and RPD between variance and mean for peak and valley survival data to ensure Poisson distributed data.

3.3.2.2 Poisson regression

As mentioned in 2.4.3.2 we wanted to make a model suitable for all irradiation configurations.

But we also wanted to see if the new Poisson quadrat analysis gave comparable results to the traditional LQ model fitted for OPEN field irradiated data. Using dose and dose squared as explanatory variables, we fitted the OPEN field data once more, only now we used the Poisson regression. This time we could not normalize with to control flasks as we did in section 3.3.1.

The result can be seen in

Table 3-6. The output was generated by the *statsmodels* package and contains the coefficients for all fitted parameters, their standard error, z-score, p-values and 95% confidence interval.

Additionally, a χ^2 -test was performed to estimate the goodness of fit between the model and the observed data, only p-value are represented as the χ^2 statistic is highly sensitive to sample size and not very informative on its own. The α and β coefficients became 0.06 ± 0.1 and 0.014 ± 0.002 , respectively. This yielded an α/β -ratio of 4 ± 1 .

Table 3-6. Poisson regression output for 1 x 1 mm² with two explanatory variables. The fitting parameters are const, x1 and x2. Const is the intercept (log of expected number of colonies at zero dose), x1 and x2 is dose and dose squared, respectively. The p-value of the coefficients show if there is a significant correlation between the explanatory variable and the independent variable. The p-value in the right column was calculated from the χ^2 output gathered from the regression result, indicating a goodness of fit between the observed data and the model.

# Explanatory variables	Poisson regression output 1 x 1 mm ² quadrat size						χ^2 (p-value)
2	coef	std err	z	P> z 	[0.025	0.975]	
	const	0.1744	0.011	16.527	0.000	0.154	0.195
	x1	-0.0566	0.012	-4.622	0.000	-0.081	-0.033
	x2	-0.0144	0.002	-6.028	0.000	-0.019	-0.010

With these results we could expand the model, by incorporating all survival data from all quadrats for all irradiation configurations OPEN field, GRID stripes and GRID dots. The data were as mentioned divided into a training (80%) and a test (20%) set. Regression results from fitting the survival data from the training set with 1 x 1 mm² quadrats are represented here, while the results from 4 x 4 mm² quadrats are in the Appendix, section 7.9. Table 3-7 shows the 1 x 1 mm² regression output. Various number of explanatory variables were tested. The first two variables were D and D^2 , both having p-values < 0.05. Peak distance was introduced as a third variable. Peak distance was significant, though with a higher p-value of 0.023. PAR was also introduced as a third variable and had a p-value of 0.0. PAR had a larger impact on the other coefficients changing their values significantly compared to peak distance. Finally, all variables were included in the model. This resulted in all variables having p-values below 0.05, and the p-value of peak distance reduced from 0.023 to 0.0. All coefficients were negatively correlated with survival, expect for the coefficient of peak distance. And all χ^2 -tests did not show significant difference between the model and the data.

Table 3-7. Poisson regression output for 1 x 1 mm² with increasing number of explanatory variables. The fitting parameters are const, x1, x2, x3 and x4. Const is the intercept, x1 and x2 is dose and dose squared, respectively. x3 is either peak distance or PAR when number of explanatory variables are 3. x4 is peak distance when all explanatory variables are included. The p-value of the coefficients show if there is a significant correlation between the explanatory variable and the independent variable. The p-value in the right column was calculated from the χ^2 output gathered from the regression result, indicating a goodness of fit between the observed data and the model.

# Explanatory variables	Poisson regression output 1 x 1 mm ² quadrat size						χ^2 (p-value)																																																	
2	<table> <thead> <tr> <th></th><th>coef</th><th>std err</th><th>z</th><th>P> z </th><th>[0.025</th><th>0.975]</th><th></th></tr> </thead> <tbody> <tr> <td>const</td><td>0.1582</td><td>0.007</td><td>22.346</td><td>0.000</td><td>0.144</td><td>0.172</td><td></td></tr> <tr> <td>x1</td><td>-0.0320</td><td>0.008</td><td>-4.191</td><td>0.000</td><td>-0.047</td><td>-0.017</td><td></td></tr> <tr> <td>x2</td><td>-0.0247</td><td>0.001</td><td>-18.537</td><td>0.000</td><td>-0.027</td><td>-0.022</td><td></td></tr> </tbody> </table>							coef	std err	z	P> z	[0.025	0.975]		const	0.1582	0.007	22.346	0.000	0.144	0.172		x1	-0.0320	0.008	-4.191	0.000	-0.047	-0.017		x2	-0.0247	0.001	-18.537	0.000	-0.027	-0.022		1																	
	coef	std err	z	P> z	[0.025	0.975]																																																		
const	0.1582	0.007	22.346	0.000	0.144	0.172																																																		
x1	-0.0320	0.008	-4.191	0.000	-0.047	-0.017																																																		
x2	-0.0247	0.001	-18.537	0.000	-0.027	-0.022																																																		
3 (peak distance)	<table> <thead> <tr> <th></th><th>coef</th><th>std err</th><th>z</th><th>P> z </th><th>[0.025</th><th>0.975]</th><th></th></tr> </thead> <tbody> <tr> <td>const</td><td>0.1514</td><td>0.009</td><td>17.548</td><td>0.000</td><td>0.135</td><td>0.168</td><td></td></tr> <tr> <td>x1</td><td>-0.0325</td><td>0.008</td><td>-4.210</td><td>0.000</td><td>-0.048</td><td>-0.017</td><td></td></tr> <tr> <td>x2</td><td>-0.0246</td><td>0.001</td><td>-18.451</td><td>0.000</td><td>-0.027</td><td>-0.022</td><td></td></tr> <tr> <td>x3</td><td>0.0359</td><td>0.016</td><td>2.266</td><td>0.023</td><td>0.005</td><td>0.067</td><td></td></tr> </tbody> </table>							coef	std err	z	P> z	[0.025	0.975]		const	0.1514	0.009	17.548	0.000	0.135	0.168		x1	-0.0325	0.008	-4.210	0.000	-0.048	-0.017		x2	-0.0246	0.001	-18.451	0.000	-0.027	-0.022		x3	0.0359	0.016	2.266	0.023	0.005	0.067		1									
	coef	std err	z	P> z	[0.025	0.975]																																																		
const	0.1514	0.009	17.548	0.000	0.135	0.168																																																		
x1	-0.0325	0.008	-4.210	0.000	-0.048	-0.017																																																		
x2	-0.0246	0.001	-18.451	0.000	-0.027	-0.022																																																		
x3	0.0359	0.016	2.266	0.023	0.005	0.067																																																		
3 (PAR)	<table> <thead> <tr> <th></th><th>coef</th><th>std err</th><th>z</th><th>P> z </th><th>[0.025</th><th>0.975]</th><th></th></tr> </thead> <tbody> <tr> <td>const</td><td>0.1557</td><td>0.007</td><td>21.978</td><td>0.000</td><td>0.142</td><td>0.170</td><td></td></tr> <tr> <td>x1</td><td>-0.0785</td><td>0.011</td><td>-7.359</td><td>0.000</td><td>-0.099</td><td>-0.058</td><td></td></tr> <tr> <td>x2</td><td>-0.0199</td><td>0.002</td><td>-12.634</td><td>0.000</td><td>-0.023</td><td>-0.017</td><td></td></tr> <tr> <td>x3</td><td>0.1278</td><td>0.019</td><td>6.867</td><td>0.000</td><td>0.091</td><td>0.164</td><td></td></tr> </tbody> </table>							coef	std err	z	P> z	[0.025	0.975]		const	0.1557	0.007	21.978	0.000	0.142	0.170		x1	-0.0785	0.011	-7.359	0.000	-0.099	-0.058		x2	-0.0199	0.002	-12.634	0.000	-0.023	-0.017		x3	0.1278	0.019	6.867	0.000	0.091	0.164		1									
	coef	std err	z	P> z	[0.025	0.975]																																																		
const	0.1557	0.007	21.978	0.000	0.142	0.170																																																		
x1	-0.0785	0.011	-7.359	0.000	-0.099	-0.058																																																		
x2	-0.0199	0.002	-12.634	0.000	-0.023	-0.017																																																		
x3	0.1278	0.019	6.867	0.000	0.091	0.164																																																		
4	<table> <thead> <tr> <th></th><th>coef</th><th>std err</th><th>z</th><th>P> z </th><th>[0.025</th><th>0.975]</th><th></th></tr> </thead> <tbody> <tr> <td>const</td><td>0.1303</td><td>0.009</td><td>14.749</td><td>0.000</td><td>0.113</td><td>0.148</td><td></td></tr> <tr> <td>x1</td><td>-0.0865</td><td>0.011</td><td>-8.050</td><td>0.000</td><td>-0.108</td><td>-0.065</td><td></td></tr> <tr> <td>x2</td><td>-0.0186</td><td>0.002</td><td>-11.715</td><td>0.000</td><td>-0.022</td><td>-0.016</td><td></td></tr> <tr> <td>x3</td><td>0.1677</td><td>0.019</td><td>8.612</td><td>0.000</td><td>0.130</td><td>0.206</td><td></td></tr> <tr> <td>x4</td><td>0.0753</td><td>0.017</td><td>4.531</td><td>0.000</td><td>0.043</td><td>0.108</td><td></td></tr> </tbody> </table>								coef	std err	z	P> z	[0.025	0.975]		const	0.1303	0.009	14.749	0.000	0.113	0.148		x1	-0.0865	0.011	-8.050	0.000	-0.108	-0.065		x2	-0.0186	0.002	-11.715	0.000	-0.022	-0.016		x3	0.1677	0.019	8.612	0.000	0.130	0.206		x4	0.0753	0.017	4.531	0.000	0.043	0.108		1
	coef	std err	z	P> z	[0.025	0.975]																																																		
const	0.1303	0.009	14.749	0.000	0.113	0.148																																																		
x1	-0.0865	0.011	-8.050	0.000	-0.108	-0.065																																																		
x2	-0.0186	0.002	-11.715	0.000	-0.022	-0.016																																																		
x3	0.1677	0.019	8.612	0.000	0.130	0.206																																																		
x4	0.0753	0.017	4.531	0.000	0.043	0.108																																																		

For further understanding of the regression output we decided to generate a correlation matrix for correlation between the explanatory variables. The *pandas* package (McKinney & others, 2010) generated this for us and the result can be seen in Table 3-8. The highest correlation was seen between dose and dose squared, and dose and PAR. For the other variables the correlations were moderate.

Table 3-8. Correlation matrix between the explanatory variables used in the Poisson regression. D represents dose.

Explanatory variables	D	D^2	PAR	Peak Distance
D	1	0.94	0.56	-0.40
D^2	0.94	1	0.35	-0.34
PAR	0.56	0.35	1	-0.43
Peak Distance	-0.40	-0.34	-0.43	1

Observed and predicted survival was plotted for 1 x 1 mm² quadrats with three explanatory variables (D , D^2 and peak distance) and is shown in Figure 3-22. Triangles represent the survival predicted by the Poisson regression, while the points represent the observed survival. Because of difficulty interpreting the plot, we visualized the data differently (Figure 3-23). The irradiation configurations were plotted separately, and the doses were binned together in dose categories with 0.5 Gy separation (0,0.5,1,1.5, ...etc.). Mean SC was found within each dose category and represented the observed survival. The process was repeated for predicted SC and the result can be seen in Figure 3-23. The trend was that the observed SC followed the predicted SC, but larger variations were observed for dotted GRID. Vertical error bars represented the standard deviation of the mean SC within a dose category, while horizontal error bars represented the standard deviation between the doses in each dose category. There were fewer datapoints for OPEN field because there was no dose gradient, thereby fewer dose categories.

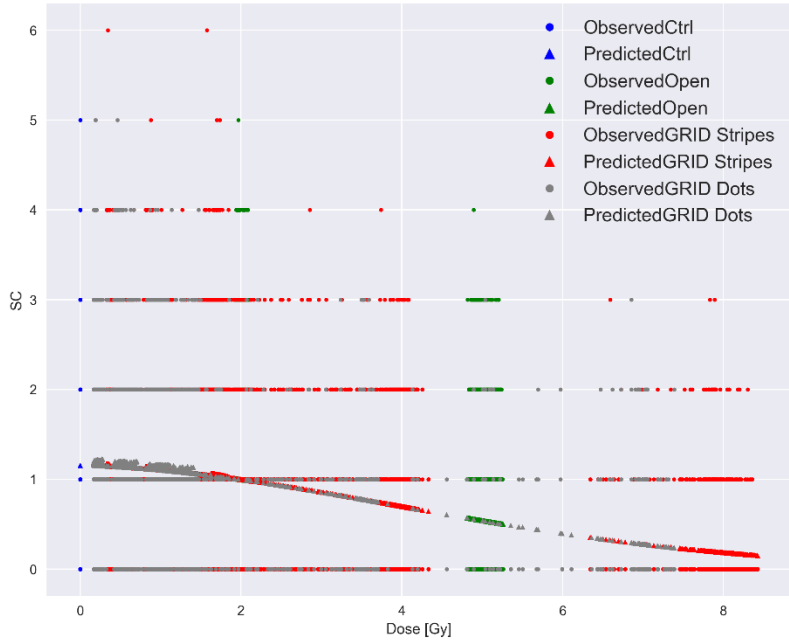


Figure 3-22. Observed survival vs survival predicted by a trained Poisson regression model for $1 \times 1 \text{ mm}^2$ quadrat size and 3 explanatory variables (D , D^2 and peak distance). All survival data was fed to the model, but we plotted each irradiation configuration separately. SC stands for surviving colonies.

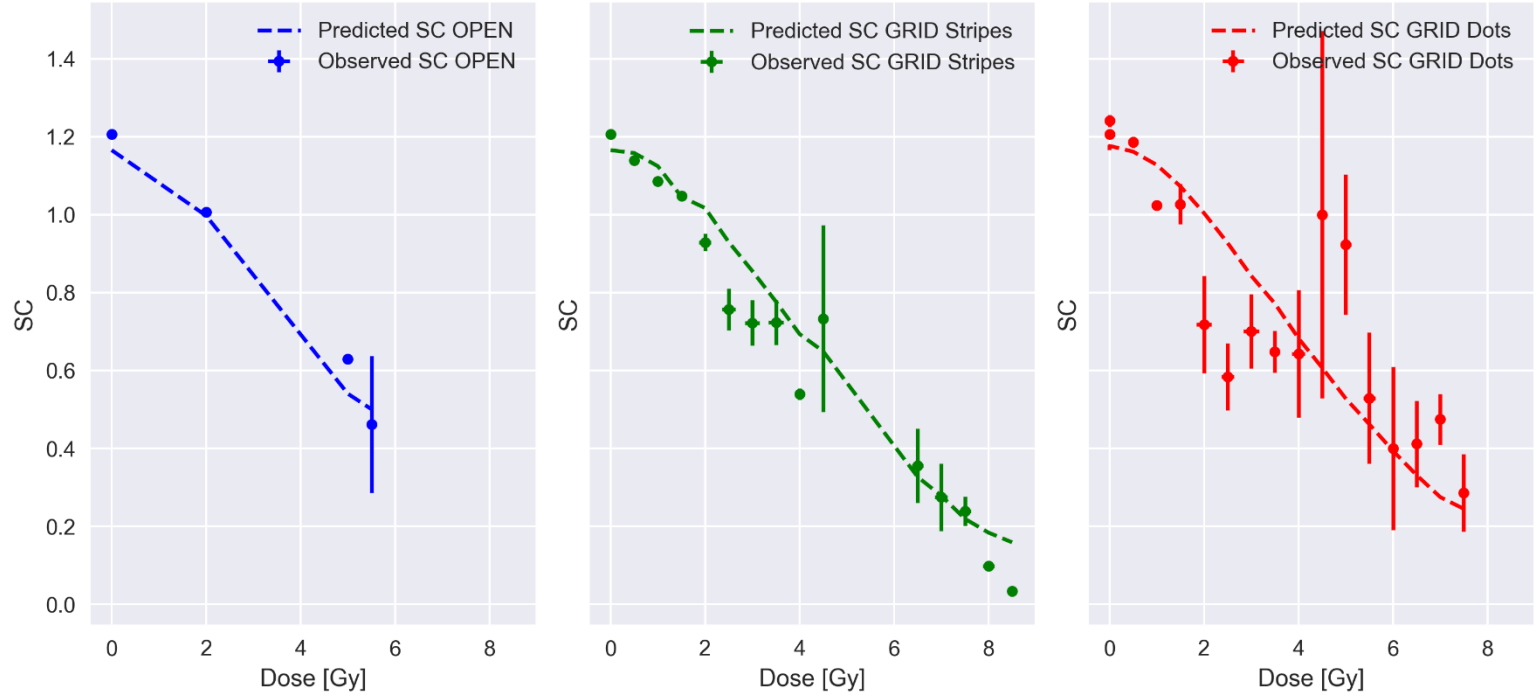


Figure 3-23. SC for OPEN, GRID stripes and GRID dots. For easier visualization of the data presented in Figure 3-22 the doses were separated into dose categories with 0.5 Gy separation (0, 0.5, 1, 1.5 etc.). The mean SC was found within each dose category with standard error (vertical error bars). The standard deviation of each dose category are the horizontal error bars. Because peak distance was used as the third explanatory variable, it was not possible to generate a regression line for the predicted SC by interpolating. We therefore had to bin doses and find mean SC the same way as for the observed data.

Figure 3-24 was generated as a comparison to the survival profiles generated from the band analysis shown in Figure 3-19. We chose to compare the peak and valley survival of cells irradiated with 5 Gy nominally, as these results exhibited the least amount of noise and gave the narrowest confidence band for the predicted survival. The plot compares observed peak and valley survival to predicted survival found by inserting the quadrat doses for a 5 Gy striped GRID irradiated dose map into the Poisson regression model fitted with OPEN field data. From the plot we observed the same tendency as shown in Figure 3-19 with mostly the same survival in valley regions and a decreased survival in the peak regions.

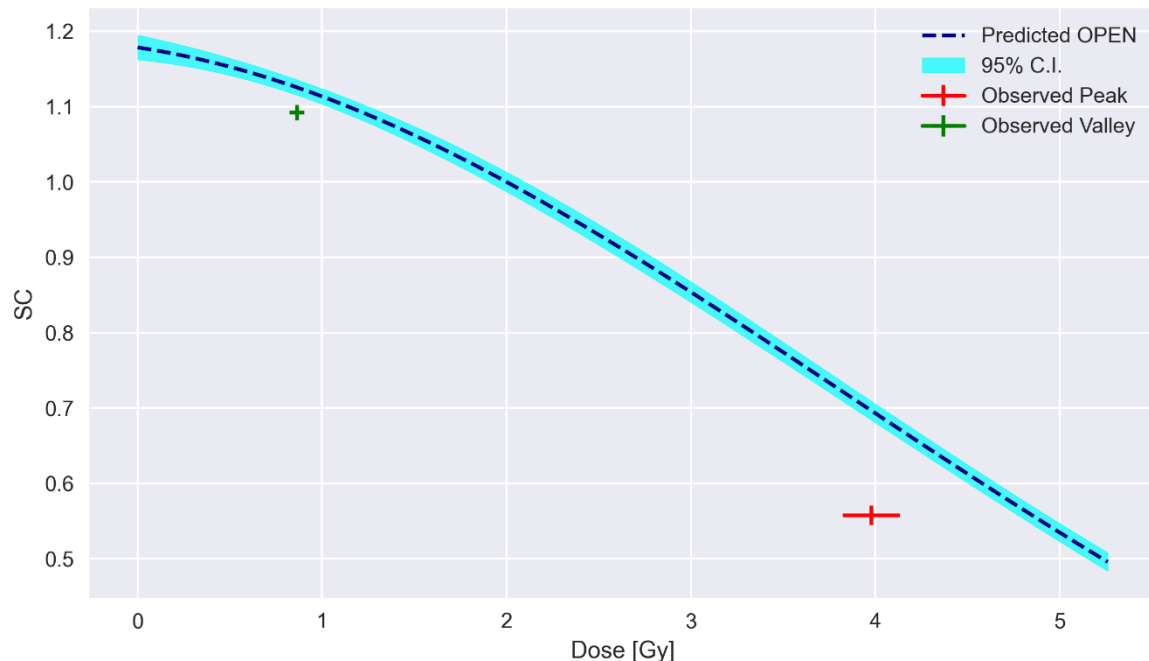


Figure 3-24. Poisson regression line generated using the coefficients found in Table 3-6. Observed survival was found by separating the quadrats into either the peak or valley category, before finding the mean survival of said category. The vertical error bar represents the standard deviation of the mean SC, and the horizontal error bar represents the standard deviation in doses within peak or valley.

3.3.2.3 Model evaluation

AIC scores were found for increasing number of explanatory variables. The first two variables were always dose and dose squared, but the third variable could either be PAR or peak distance. For four variables both PAR and peak distance was used. Figure 3-25 shows the AIC scores for $1 \times 1 \text{ mm}^2$ quadrats. For this quadrat size, the optimal model resulting in the lowest overall AIC score was three explanatory variables with peak distance being the third one.

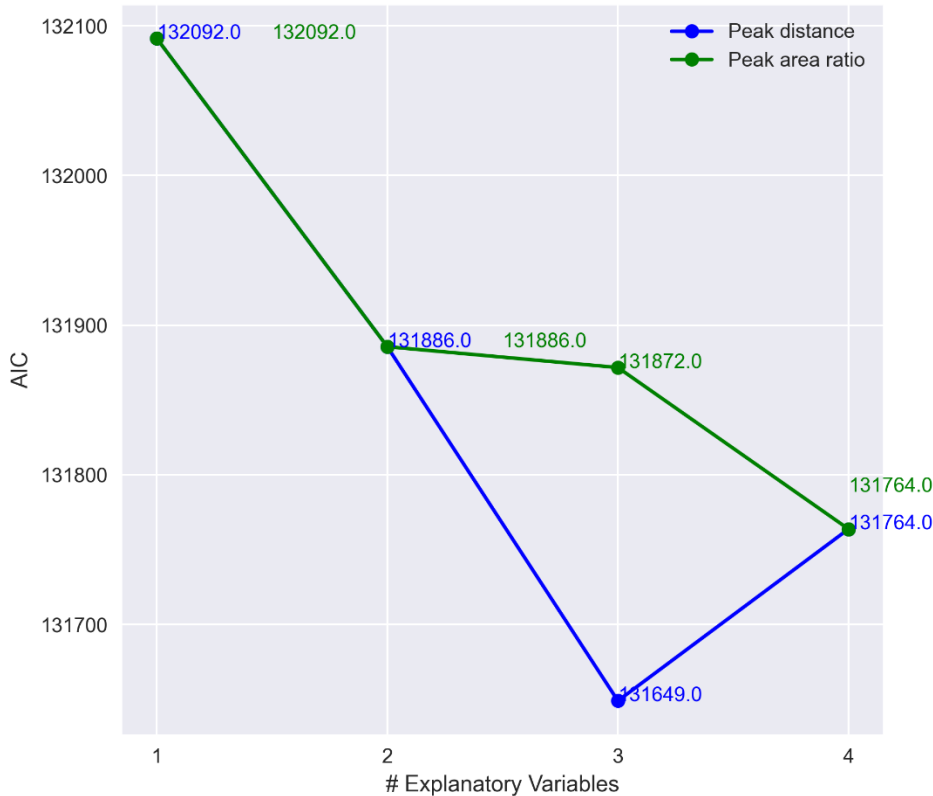


Figure 3-25. AIC score for increasing model complexity for $1 \times 1 \text{ mm}^2$ quadrats. The first and second explanatory variables were always dose and dose squared. The plot compares adding peak distance or PAR as the third explanatory variable to predict SC in the Poisson regression. For four explanatory variables, both PAR and peak distance were used.

MSE was found comparing the raw observed and predicted data from Figure 3-22 for individual irradiation configurations. An ANOVA test was performed between the different groups. This showed that there was a significant difference between the squared errors of OPEN and GRID dots ($p\text{-value} \approx 2 \cdot 10^{-8}$) and between striped and dotted GRID ($p\text{-value} \approx 1 \cdot 10^{-6}$), but no significant difference between OPEN and striped GRID ($p\text{-value} \approx 0.23$). We were also interested in comparing the MSE of the train and test data. Both MSE comparisons can be found in Figure 3-26. All irradiation configurations yielded similar MSE values, with GRID dots and Control being slightly higher. The difference between train and test was negligible.

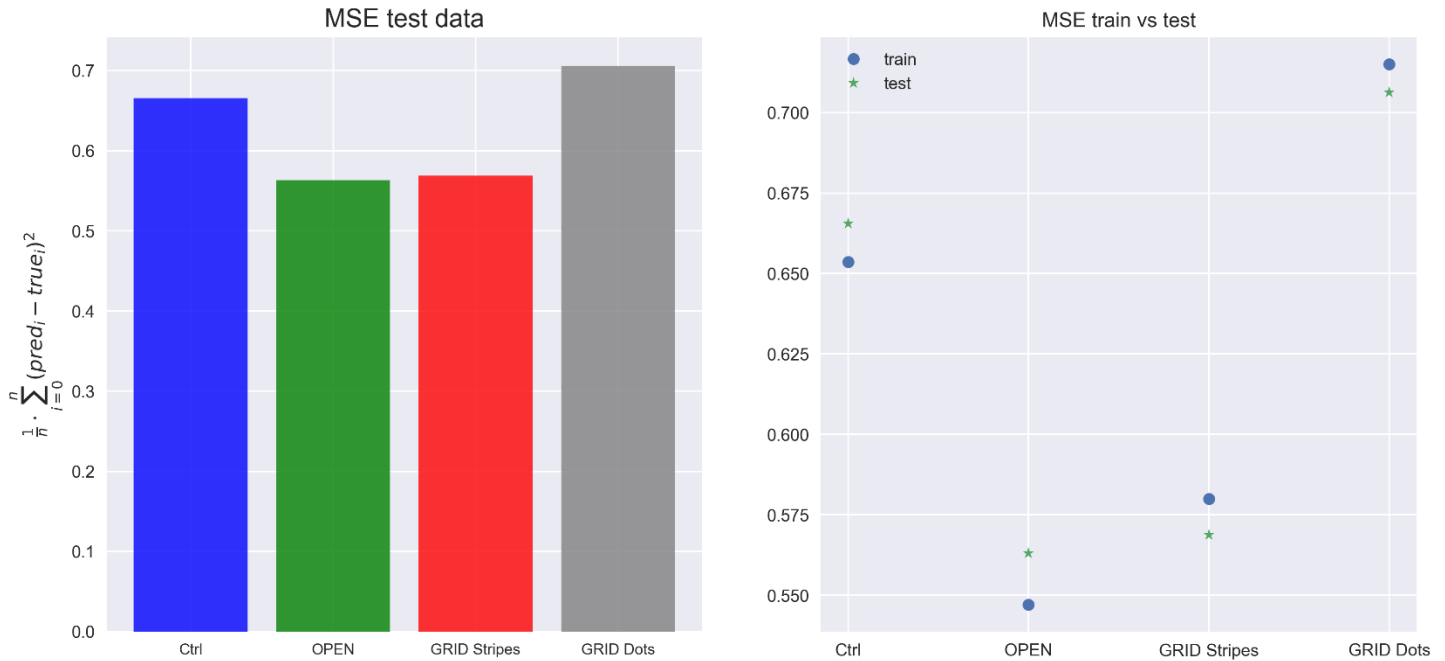


Figure 3-26. Prediction performance of test data measuring MSE (left) and comparing train and test MSE (right) for all irradiation configurations for $1 \times 1 \text{ mm}^2$ quadrats with dose, dose squared and peak distance as explanatory variables 3 regressors.

4 Discussion

4.1 X-ray Dosimetry

The first ionization chamber dosimetry performed for striped GRID resulted in a mean R^2 of 0.9976 ± 0.0001 , proving a strong linear relationship between short exposure times and low doses. A ramp-up time of approximately 3 s was found for the X-ray unit in question, with a dose rate of $\dot{D} = 0.60 \pm 0.01 \text{ Gy/min}$ (short exposure times). The dose rate obtained from 60 s measurements (longer exposure time) resulting in $\dot{D} = 0.59 \pm 0.02 \text{ Gy/min}$. Thus, both dose rates were within one standard deviation, indicating a stable beam over all exposure times used in this experiment. The dose rate obtained from the 60 second measurements from the second round of ionization chamber dosimetry for dotted GRID was $\dot{D} = 0.60 \pm 0.02 \text{ Gy/min}$, which was also within one standard error of the dose rate from the first calibration. This showed that the X-ray machine gave consistent results over the time period when the calibrations were performed.

A cause for concern, however, was the difference in the dosimetry protocol between the cell experiments and the Gafchromic™ film dosimetry. From the exposure times found in Magnus Børsting's thesis we saw a systematic decrease in time necessary to achieve 0.2, 2, 5 and 10 Gy. Two possible explanations for the reduction could be: different conditions during irradiation, such as temperature and air pressure. Observing the exposure times in Table 7-2 we see a reduction in exposure time between the first and the second calibration performed at different time points, which support this theory. Or the reduction could be caused by not accounting for the height difference between the sensitive volume of the ionization chamber and the bottom of the cell flask, causing an overestimation of dose received by the cells. The exposure times seen in Magnus Børstings' results were smaller than both our calibrations. Future experiments should be performed where the same dosimetry protocol is employed for cell experiments AND Gafchromic™ film dosimetry.

4.2 Gafchromic™ film dosimetry

Cutting the EBT3 films using a paper cutter was sufficient when the films were cut in rectangular shapes. Once the films were cut to match the shape of the cell flask, it resulted in positional shifts of the films inside the cell flask, thereby shifting the grid pattern shown in the film response. For striped GRID the consequences were not too severe because the stripes covered transverse bands of the flask and the shift only impacted a small part of the total peak area. But for dotted GRID the shifts caused some films to have peaks that fell outside or on the films' edges (Figure 2-11), forcing cropping of the colony maps, thereby removing valuable survival data. A solution would be to order precut films or to cut them ourselves using a laser cutter. This would increase the similarity between the films, making the films fit better inside the cell flasks, thereby reducing required transformation to match them. It would center the GRID pattern, keeping it further away from the damaged edges of the films, where dose measurements were imprecise (see 2.1.2.3).

For field sizes (area of radiation field at a specified SDD) between $10 \times 10 \text{ mm}^2$ and $100 \times 100 \text{ mm}^2$, an ROI of $4 \times 4 \text{ mm}^2$ has been recommended (Gholizadeh Sendani et al., 2018). We found that the optimal ROI size for RED channel was $3 \times 3 \text{ mm}^2$, resulting in lowest MSE (0.0121) when fitting equation 2-6. However, comparing the total MSE for $4 \times 4 \text{ mm}^2$ and $2 \times 2 \text{ mm}^2$ we saw that the RPD was approximately 0.5% and 1%, respectively, which was low enough to use either one. Thus, the MSE is not highly sensitive to ROI sizes between 2-4 mm. In hindsight we

figured it would have been better to use $4 \times 4 \text{ mm}^2$ to capture more of the variation within each film.

Choosing the right color channel had a bigger impact on the fit. The sensitivity of the BLUE channel was much lower compared to RED channel, as seen in Figure 3-4 and Figure 3-5 In Figure 3-5 we also observe that some of the films irradiated with low doses (0.1,0.2 and 0.5 Gy) have a netOD of zero. This means that the BLUE channel intensity was higher than the average control intensity (see 2.1.2.3), and the data were not usable. The data were also split into high and low response decreasing the available data for fitting, thereby increasing the uncertainty of the fitting parameters (Table 7-3), making it even more important to choose a color channel with sufficient sensitivity.

Another possibility is to perform multichannel dosimetry. Micke et al., 2011 showed that including the intensity of all channels removed disturbances in the scanned images due to film inhomogeneity and artefacts generated by the scanner. Multichannel dosimetry utilizes otherwise abandoned data in single channel dosimetry and is a possibility for future work.

As mentioned in 2.1.2, we tried to eliminate the possibility of getting a split response from erroneous scanning by increasing the difference between the sides of the films during the second calibration. However, this did not remove the split response. A potential reason for the split response could be variation in dose received by the films, caused by different positioning in the radiation field. As mentioned in 2.1.1 all positions were irradiated at once, and looking at Table 7-1 we saw an increase in output going from position A and B to C and D. However, the measured RPD of mean output of positions A and B, compared to positions C and D was only around 0.8%.

The split response was also observed in the control films. As they were not irradiated, the split response cannot be explained by the different positioning in the radiation field.

This indicates a split response within a film batch, as well as between batches. For future work, it would be advisable to perform our dosimetry on two separate batches, and record which sheet each film originated from. In the dose profiles generated for OPEN field and striped GRID in Figure 3-12 we can qualitatively observe a match between the high and low response fitted dose profiles. For dotted GRID, where no clear separation of high and low response was observed in the second calibration, we used two different approaches. First, we fitted all data, ignoring any

split response. The resulting GRID dose profiles showed a clear separation in high and low response. Using the fitting parameters from the first calibration and assuming only two possible responses for the film batch in question, we achieved a better match of the profiles seen in Figure 3-10, proving the need for separate fitting of high and low response films.

Estimated dose for OPEN field was 4.98(4.93,5.03). Assuming 5 Gy being the true dose, the relative systematic error was 0.4%. Additionally, the results from the Monte Carlo simulations of striped GRID showed a good match between predicted relative dose and observed dose, further supporting our dosimetry. Peak striped and dotted GRID dose was about 81% and 68% of the OPEN field dose, which is likely due to scattered photons from the X-ray source or air above the flask being attenuated by the GRID collimator openings. These scattered photons would normally contribute to the dose for OPEN field, and the smaller the collimator opening the smaller the GRID to OPEN dose ratio. We also obtained a nonzero dose in valley areas (typically 9-17 % of OPEN field dose), which may be caused by some photon transmission through the GRID tungsten. Still, the attenuation coefficient μ for 200 keV photons is 15.1 cm^{-1} ($\mu/\rho_W \cdot \rho_W$) (*NIST: X-Ray Mass Attenuation Coefficients - Tungsten*, n.d.), giving 0.05% transmission through 5 mm tungsten. However, more divergent scattered photons with a nonzero incident angle may also reach the EBT3 film in the valley areas as illustrated in Figure 4-1. The distance between the grid block and the cells was approximately 2.5 cm, giving the photons space to diverge after passing the grid openings and possibly increase the valley dose. The nonzero valley dose was in line with previous studies (R. S. Asur et al., 2012; Gholami et al., 2016). No simulations were performed for dotted GRID. However, the reduction in dose compared to striped GRID seen in Figure 4-2 can be explained by the GRID pattern. The dotted GRID pattern had a smaller peak area, which reduced the fluence of photons through the openings of the GRID, thereby reducing both the peak and valley dose received by the EBT3 film.

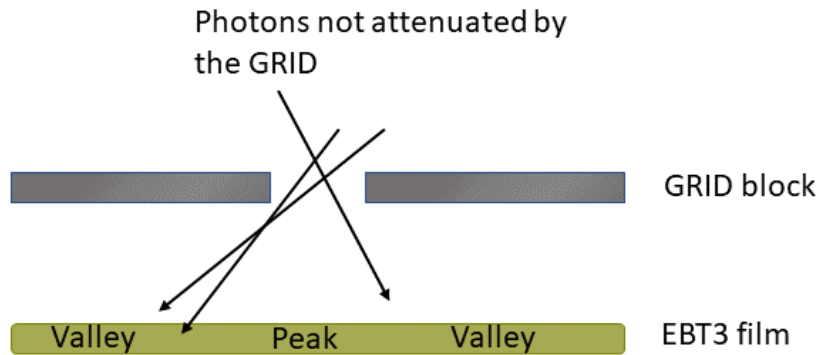


Figure 4-1. Figure illustrating why there is a nonzero dose in the shielded areas of the EBT3 dosimetry films underneath the GRID block. Divergent photons are not attenuated by the GRID and deposit their energy in the shielded areas.

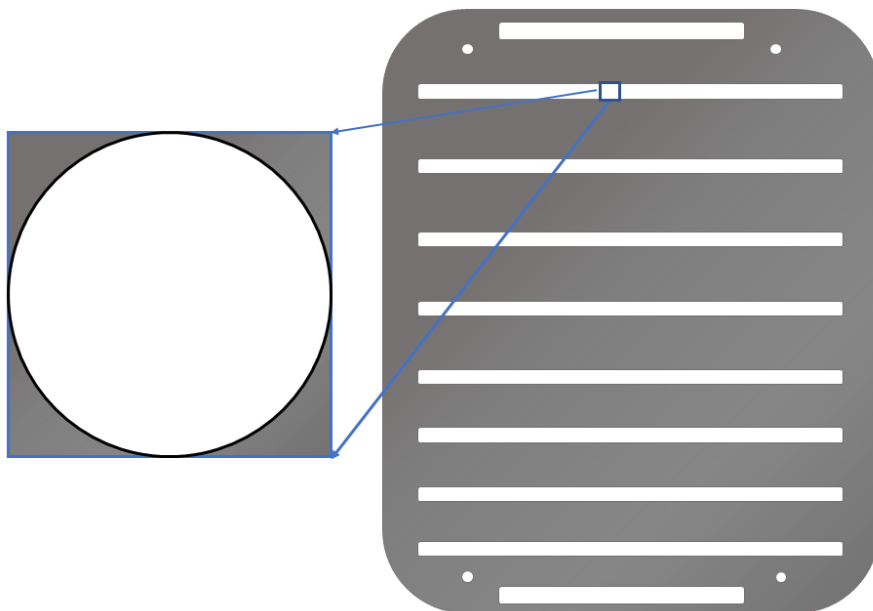


Figure 4-2. Striped GRID block. We observe that exchanging the continuous stripes (5 mm opening) for circles (5 mm diameter), results in a smaller opening, which will reduce the overall dose levels for dotted GRID further compared to striped GRID

4.3 Cell Survival

Data from the cell experiments was chosen based on the plating efficiency and how close the survival levels in the control flasks were between the experiments. We observed a low PE (around 5%) for some of the experiments, and these were not included in the current cell survival analysis. The flasks from the experiment with the lowest PE were studied by Magnus Børsting under the microscope (Magnus Børsting, 2020, section 4.2.1), and the low PE was confirmed. It was speculated that seeding 30 000 cells resulted in a high confluence inhibiting cells from dividing further. Another possibility was systematic undercounting by the segmentation

algorithm. The data included had a not very high PE (8 – 10 %) but was deemed to have sufficient quality and consistency. Both the stained (upper row) and segmented (lower row) cell flasks in Figure 7-5 were inspected by Associated Prof. Nina Edin (experienced in cell counting), as well as delineated data from the segmentation. Her assessment was that the algorithm did not successfully separate all the BLOBs into individual colonies. This implies that the cell count is underestimated in specifically in regions with low to no dose. Incidentally, the segmentation algorithm has been validated for low colony density (Arous et al., 2022), so we expect a higher accuracy in the peak regions. A possible explanation for the underestimation of high colony density was that the resolution of the scanned cell flasks was too low. A Gaussian filter was applied to the PCA images to suppress noise. The slight smoothing might wash away small intensity variations that constituted the difference between two cell colonies. Increasing the resolution might mitigate the merging of cell colonies and should be tested in future experiments, as well as comparing the algorithm with manually counted data. Different number of cells seeded in the flask should also be tested, preferably with lower cell density, with the intent of retaining highest possible segmentation accuracy, while still seeing the effects of the dose gradient.

4.4 1D survival analysis

α and β found from OPEN field irradiated cell flasks was 0.06 ± 0.04 and 0.011 ± 0.008 , respectively. Neither had p-values below 0.05, indicating no significant correlation between our survival and the dose (and dose squared). The resulting α/β ratio from the OPEN field irradiated cell flasks was 6 ± 5 Gy. A high uncertainty in both estimated parameters (Table 3-4) lead to a high uncertainty seen in the α/β ratio, likely caused by the amount of data being relatively low with only 8 datapoints per dose. It also did not help that the 10 Gy data were unusable because of unsuccessful segmentation leaving only three dose points for the analysis 0, 2 and 5 Gy.

In future experiments one should include more doses and try to include doses representative of received doses in peak and valley. (Hilde Solesvik Skeie, 2021) reported in her master thesis an α/β -ratio of 12.9 ± 0.05 Gy using the same irradiation setup. It should be noted that the uncertainty was worryingly low and based on her estimated uncertainties for α and β , with error propagation we calculated an uncertainty of ± 4 Gy, which puts our result within one standard deviation of the 13 Gy α/β ratio. However, further analysis and improvements to the segmentation algorithm should be performed.

The survival analysis using bands of 1 mm width resulted in the plots seen in Figure 3-19. For 5 Gy the predicted survival was higher than the observed survival in peak areas, and mostly the same in valley areas. As mentioned in the previous section, we believed that the segmentation algorithm underestimated number of viable colonies. Intuitively one might think that low doses result in a higher degree of underestimation because there are more colonies and more BLOBs to classify. However, the predicted and observed survival in peak area was based on the same dose, and the difference cannot necessarily be explained by segmentation error. Another explanation was possible bystander effects and communication between the cells in the peak areas, leading to increased cytotoxicity. Based on the number of cells seeded we estimated the average distance between the cells to be approximately 0.2 mm (see section 7.10). A previous study used inverted microscopy to find the diameter of an A549 cell of about 14.93 μm (Jiang et al., 2010). This implied that the cells were not close enough to communicate through gap junction, and soluble factors released into the medium are more likely contributors. In future work it would be necessary to perform cell experiments where survival of GRID irradiated cells was compared to OPEN field irradiated cells but including doses representative of peak and valley.

We also observed an increase in RPD from 2 to 5 Gy nominal dose, which could indicate an increase in bystander effect for larger doses. However, the survival data for 2 Gy GRID was noisy and hard to interpret. In a review article by (R. Asur et al., 2015), it was shown results with higher survival in peak areas, and lower survival in valley areas. It should be noted that most of these SFRT experiments used different experimental setups, utilizing 6 MV photons with 50/50 peak valley area and different cell lines (Mackonis et al., 2007; Suchowerska et al., 2005; Trainor et al., 2012).

Results from (Peng et al., 2017) indicated a cell survival dependency on GRID configuration, where 2.5 mm openings in the striped grid resulted in significant difference in survival for the NCI-H460 cancer cell lines compared to OPEN field, but the significance was lost when using GRID with 5 mm openings after being given an average dose of 3.5 Gy. This coincides with our results as overall survival was reduced for 5 Gy. Still, Peng et al's analysis is different from ours and it is not shown whether the decreased survival in their work was in the peak or valley region.

4.5 2D survival analysis

A dotted GRID configuration is not well suited for band analysis. Therefore, we analyzed survival in 2D by summing up colonies within quadrats of different sizes, before using Poisson regression to fit the data. To evaluate which quadrat size was best suited for the Poisson regression, we calculated different criteria values. The data showed that for most doses and quadrat sizes the null hypothesis could not be rejected, i.e., there was no statistically significant difference between the theoretical Poisson distribution and our observed data. We only rejected the null hypothesis for peak survival 10 Gy of 2×2 and $3 \times 3 \text{ mm}^2$. This can be explained by the associated histograms, which exhibited elongated tails (compared to expected) and outliers. The optimal quadrat size was $1 \times 1 \text{ mm}^2$, which did not display the smallest RPD but had a low number of zero colony quadrats and retained more variance in dose. Also, decreasing quadrat size makes the nearest peak distance a more realistic explanatory variable. As mentioned, nearest peak distance was defined as the distance from the center of the quadrat to the nearest peak. For a larger quadrat, this distance becomes less representative of colonies located further from the center.

The 2D analysis for OPEN field with $1 \times 1 \text{ mm}^2$ quadrats resulted in α and β of 0.06 ± 0.01 and 0.014 ± 0.002 , respectively. These results were comparative to the 1D OPEN field regression seen in Table 3-4. However, with the Poisson regression, the uncertainties were lower and both dose and dose squared had $p < 0.05$, likely caused by the increase in datapoints when dividing the cell flasks into quadrats. However, we still observe a low α/β -ratio compared to previous findings (Hilde Solesvik Skeie, 2021). It may be that the potential systematic underestimation in colony count for zero to low doses by the segmentation algorithm impacted our results. In fact, shifting the low dose count to higher values would imply a straighter fit line to the data (i.e., less curvature) with a higher α and thus higher β . Despite this, it was positive that both the Poisson regression and the regular fitting of the LQ model showed similar results internally.

The regression plot in Figure 3-22 for OPEN, GRID stripes and GRID dots for $1 \times 1 \text{ mm}^2$ was difficult to interpret, but a slight decrease in survival was observed for doses above 4 Gy. This effect was much easier to observe for a $4 \times 4 \text{ mm}^2$ quadrat size

Figure 7-8), however this result was put into the appendix because of the results from the Poisson evaluation indicating $1 \times 1 \text{ mm}^2$ being the optimal. We also wanted to make the model independent of grid configuration, and increasing quadrat size would compromise this goal, as discussed in 2.4.3.1.

To improve interpretability of Figure 3-22 we binned the doses into dose categories and found the mean survival within these for observed and predicted survival represented in Figure 3-23. We observed a closer fit for OPEN field with an increasing deviation from the prediction line when striped and dotted GRID were introduced. We will get further into this in the MSE discussion. We also observed increasing vertical error bars. Because these represented the standard error, that were affected by the number of datapoints within a specific dose category. OPEN field had fewer dose categories with more datapoints in each. This explained the larger vertical error bars for GRID irradiated cell flasks, and even larger error bars for quadrats positioned between peak and valley. The regression output for $1 \times 1 \text{ mm}^2$ quadrats in Table 3-7 showed that all proposed combinations of the 4 explanatory variables dose, dose squared, peak distance and PAR yielded significant coefficients, indicating that the additional variables explain some kind of GRID effect on survival. Additionally, the χ^2 test showed **no** evidence of the data **not** following the estimated model ($p>0.05$).

Dose and dose squared showed an expected high correlation. Nevertheless, this should not be problematic. As mentioned, α and β represents the mode 1 and mode 2 DSBs (1.7.5), respectively. They are therefore not meant to explain survival separately. There was a relatively high correlation between PAR and dose (0.56). However, it did not affect its significance, which could indicate that PAR might hold additional explanatory power that describe how spatial fractionation affect the survival. Peak distance showed a moderate negative correlation with the other explanatory variables, -0.4, -0.35 and -0.43 with dose, dose squared and PAR, respectively. This was expected, as dose decrease with distance away from the peak areas, and a larger PAR results in lower peak distances.

AIC scores in Figure 3-25 evaluated the inclusion of additional variables in the model. For $1 \times 1 \text{ mm}^2$ it was better to include peak distance as the third variable and discard PAR. But when including PAR as the third variable, including all variables gave the lowest AIC. This could indicate that peak distance better explains survival of the cells. Peak distance had the lowest correlation which might explain why it adds more explanatory power to the model compared to

PAR. However, the result flipped when using a 4 x 4 mm² quadrat (see Appendix Figure 7-9) making PAR the optimal variable. This supported our theory about peak distance being less accurate for larger quadrat sizes.

An interesting observation was that, when introduced as the third explanatory variable, peak distance was not significant for quadrat sizes above 1 x 1 mm². In Appendix Table 7-5 we see that peak distance has a p-value of 0.98 and a coefficient of 0.0004, but when PAR was included the p-value dropped to 0.004 and the coefficient increased to 0.0544 (136 times larger). A possible explanation was that the moderate correlation between peak distance and PAR (-0.43) resulted in a scenario where peak distance both explained its own effect on survival, as well as a portion of PAR's effect on survival. But when PAR was introduced only the true effect of peak distance remained, making PAR a confounding variable. The correlation between peak distance and PAR remained mostly the same for 1- and 4-mm quadrat sizes (-0.43 and -0.44, Table 3-8 and Table 7-6), but the number of datapoints were very different as 1 mm quadrats resulted in 16 times more quadrats. A larger sample size increases precision, thereby reducing the p-value (Thiese et al., 2016). Additionally, multicollinearity is known to have a larger effect on smaller sample sizes (Sari et al., 2018) and might explain how the p-value of peak distance could become so high for 4 x 4 mm² quadrats.

The comparison between predicted survival from the Poisson regression fitted for OPEN field data and observed striped GRID data were represented in Figure 3-24. The plot showed a similar trend compared to Figure 3-19 with an equal survival in valley and lower survival in peak compared to the same dose with OPEN field irradiation. Again, one may discuss whether the result was caused by poor segmentation or bystander effect (see 4.4). However, it was more important that the 2D quadrat analysis was in accordance with the 1D band analysis. And as shown in the regression result for OPEN field we get a comparative result when dividing the data into quadrats rather than analyzing the colony map as a whole, which is not possible for GRID irradiated cells receiving heterogeneous dose. A downside of the model however was that the number of colonies counted in the control flasks of each experiment included in the analysis needed to be more or less equal to include them in the Poisson regression. A traditional LQ model can include data from different experiments if they are normalized with plating efficiency, but because the Poisson regression demand whole numbered count data, this was not possible. One option could be to include a categorical explanatory variable that represented a number

between 0 and n, for n number of experiments. This would then estimate a zero-dose colony count for each separate experiment.

The MSE between predicted and observed SC for the test data were represented for every irradiation configuration in Figure 3-26. Overall, the model performed similarly for all irradiation configurations indicating that we were successful in making the model suitable for all irradiation configurations, though with significant differences between the MSE of OPEN and dotted GRID and between striped and dotted GRID (not including control). The model performed best for OPEN field survival data, which confirmed what we observed in Figure 3-23. Compared to the control data, this made sense because the model predicted the same survival for all control flasks. In this case, dose and peak distance were zero leaving only the intercept. The only source of variation in the MSE was the varying number of SC, which was higher in the case of OPEN field. This is because, when irradiating with an OPEN field the variation in SC is lower, resulting in a smaller MSE. This was not the case for when comparing the MSE of OPEN field and dotted GRID. The larger deviation from the prediction line seen in Figure 3-23 indicated that there might be an added effect from dotted GRID irradiation not sufficiently explained by dose, PAR and peak distance. It would therefore be of interest to develop our explanatory variables further. Peak distance could be exchanged with a diffusion variable, explaining diffusion of the soluble factors into the growth medium of the cells. It would also be interesting to explore the possibility of adding a bystander factor. This factor could be decided by performing bystander effect experiments where medium of irradiated cells is transferred to non-irradiated cells (Liu et al., 2006). Another reason for the higher MSE could simply be a combination of two things: the error caused by separating the flasks into quadrats not small enough to suit the dotted GRID pattern, and the lower amount of dotted GRID irradiated survival data compared to striped GRID.

5 Conclusion

Radiotherapy has two goals: Eradicate cancer cells, and spare healthy cells. Spatially fractionated radiotherapy, if fully utilized, has the potential of doing both. High dose areas kill cancer cells, while low dose areas allow for sparing of tissues situated near the cancer. In addition, effects such as the bystander effect might enhance the cancer killing in the low dose areas, resulting in the same tumor control exhibited by traditional conformal radiotherapy. The aim of this thesis

was to develop a new methodology for A549 cell survival analysis *in vitro* and further expand the knowledge on how spatially fractionation of the radiation field affects the survival of cells. Gafchromic™ EBT3 film dosimetry has been established for said cells with a successful outcome. OPEN field irradiated films exhibited the expected response of about 5 Gy with a relative systematic error of 0.4%, while response of the striped GRID irradiated films was confirmed with FLUKA Monte Carlo simulated data.

Poisson regression was utilized to estimate survival of cells irradiated with OPEN field, striped or dotted GRID in 2D. Colony maps generated from segmented cell flasks were divided into quadrats, with optimal size being 1 x 1 mm², and the number of colonies within were found. The Poisson regression was subsequently trained using the quadrat survival data. In addition to dose and dose squared, new explanatory variables were explored to explain the effect of spatial fractionation. PAR measured the area fraction of cells positioned within the peak regions. Peak distance measured the distance from a quadrat to the nearest peak. Both variables yielded significant coefficients (p-value < 0.05), but using peak distance as the third variable resulted in the lowest AIC score, supporting the need for further development of PAR and peak distance.

1D survival profiles were generated to compare observed survival of GRID irradiated cells with predicted survival from an LQ model fitted to OPEN field survival data. A similar plot was generated for 2D survival data, using the Poisson regression also fitted to OPEN field survival data with dose and dose squared as explanatory variables. Although no decisive conclusions could be drawn about the causation, we saw for both 1D band analysis and 2D Poisson regression, that survival decreased in high dose areas compared to survival predicted from homogeneously irradiated cells.

We have showed that 2D survival analysis of GRID irradiated cells is possible, and proposed a basic methodology. However, improvements of the proposed methodology is greatly encouraged.

6 References

- A549 Cell Subculture Protocol – A549 Cell Line: Cell Culture and Transfection Protocol. (n.d.). Retrieved April 5, 2022, from <https://www.a549.com/cell-subculture-protocol/>
- Adenosine triphosphate / Definition, Structure, Function, & Facts / Britannica. (2020, March 12). <https://www.britannica.com/science/adenosine-triphosphate>
- Aksnes, I. (2020, November 8). History of X-rays—125 years in the making (pt 2). *Excillum*. <https://www.excillum.com/history-of-x-rays-x-ray-tubes/>
- Alberts, B., Johnson, A., Lewis, J., Raff, M., Roberts, K., & Walter, P. (2014). *Molecular Biology of the Cell* (6th ed.). Garland Science.
- Aldelaijan, S., & Devic, S. (2018). Comparison of dose response functions for EBT3 model GafChromic™ film dosimetry system. *Physica Medica*, 49, 112–118. <https://doi.org/10.1016/j.ejmp.2018.05.014>
- Alin, A. (2010). Multicollinearity. *WIREs Computational Statistics*, 2(3), 370–374. <https://doi.org/10.1002/wics.84>
- Alm Carlsson, G. (2001). *Bragg-Gray Dosimetry: Theory of Burch*. Linköping University Electronic Press. <http://urn.kb.se/resolve?urn=urn:nbn:se:liu:diva-57834>
- Alm Carlsson, G. (2002). *Spencer-Attix Cavity Theory*. Linköping University Electronic Press. <http://urn.kb.se/resolve?urn=urn:nbn:se:liu:diva-57893>
- Amiri, S., Ali, P. J. M., Mohammed, S., Hanus, R., Abdulkareem, L., Alanezi, A. A., Eftekhari-Zadeh, E., Roshani, G. H., Nazemi, E., & Kalmoun, E. M. (2021). Proposing a Nondestructive and Intelligent System for Simultaneous Determining Flow Regime and Void Fraction Percentage of Gas–Liquid Two Phase Flows Using Polychromatic X-Ray Transmission Spectra. *Journal of Nondestructive Evaluation*, 40(2), 47. <https://doi.org/10.1007/s10921-021-00782-w>
- Andreо, P. (2015). Dose to ‘water-like’ media or dose to tissue in MV photons radiotherapy treatment planning: Still a matter of debate. *Physics in Medicine and Biology*, 60(1), 309–337. <https://doi.org/10.1088/0031-9155/60/1/309>
- Andreо, P., Burns, D. T., Nahum, A. E., Seuntjens, J., & Attix, F. H. (2017). Chemical Dosimeters. In *Fundamentals of Ionizing Radiation Dosimetry* (1st ed., pp. 562–562). John Wiley & Sons, Incorporated.
- Anne Marit Rykkeliid. (2017). *Method for in vitro Cell Irradiation with Low Energy Protons* [Master thesis]. University of Oslo.
- Apoptosis / cytology / Britannica. (2013, September 27). <https://www.britannica.com/science/apoptosis>
- Arous, D., Schrunner, S., Hanson, I., Frederike Jeppesen Edin, N., & Malinen, E. (2022). Principal component-based image segmentation: A new approach to outline in vitro cell colonies. *Computer Methods in Biomechanics and Biomedical Engineering: Imaging & Visualization*, 0(0), 1–13. <https://doi.org/10.1080/21681163.2022.2035822>

- Ashburner, J., & Friston, K. (2007). CHAPTER 4—Rigid Body Registration. In K. Friston, J. Ashburner, S. Kiebel, T. Nichols, & W. Penny (Eds.), *Statistical Parametric Mapping* (pp. 49–62). Academic Press. <https://doi.org/10.1016/B978-012372560-8/50004-8>
- Asur, R., Butterworth, K. T., Penagaricano, J. A., Prise, K. M., & Griffin, R. J. (2015). High dose bystander effects in spatially fractionated radiation therapy. *Cancer Letters*, 356(1), 52–57. <https://doi.org/10.1016/j.canlet.2013.10.032>
- Asur, R. S., Sharma, S., Chang, C.-W., Penagaricano, J., Kommuru, I. M., Moros, E. G., Corry, P. M., & Griffin, R. J. (2012). Spatially Fractionated Radiation Induces Cytotoxicity and Changes in Gene Expression in Bystander and Radiation Adjacent Murine Carcinoma Cells. *Radiation Research*, 177(6), 751–765.
- Attix, F. H. (1986). *Introduction to Radiological Physics and Radiation Dosimetry*. John Wiley & Sons.
- Attix, F. H. (2008). *Introduction to Radiological Physics and Radiation Dosimetry*. John Wiley & Sons.
- AvgPool2d—PyTorch 1.11.0 documentation*. (n.d.). Retrieved April 28, 2022, from <https://pytorch.org/docs/stable/generated/torch.nn.AvgPool2d.html>
- Battistoni, G., Boehlen, T., Cerutti, F., Chin, P. W., Esposito, L. S., Fassò, A., Ferrari, A., Lechner, A., Empl, A., Mairani, A., Mereghetti, A., Ortega, P. G., Ranft, J., Roesler, S., Sala, P. R., Vlachoudis, V., & Smirnov, G. (2015). Overview of the FLUKA code. *Annals of Nuclear Energy*, 82, 10–18. <https://doi.org/10.1016/j.anucene.2014.11.007>
- Billena, C., & Khan, A. J. (2019). A Current Review of Spatial Fractionation: Back to the Future? *International Journal of Radiation Oncology*Biology*Physics*, 104(1), 177–187. <https://doi.org/10.1016/j.ijrobp.2019.01.073>
- Bingham, N. H., & Fry, J. M. (2010). *Regression*. Springer London. <https://doi.org/10.1007/978-1-84882-969-5>
- Biomolecule / Definition, Structure, Functions, Examples, & Facts / Britannica*. (2020, March 18). <https://www.britannica.com/science/biomolecule>
- Bjørg Vårli Håland. (2020). *2D dosimetry and radiobiological modelling in GRID therapy*. University of Oslo.
- Blyth, B. J., & Sykes, P. J. (2011). Radiation-induced bystander effects: What are they, and how relevant are they to human radiation exposures? *Radiation Research*, 176(2), 139–157. <https://doi.org/10.1667/rr2548.1>
- Böhnen, T. T., Cerutti, F., Chin, M. P. W., Fassò, A., Ferrari, A., Ortega, P. G., Mairani, A., Sala, P. R., Smirnov, G., & Vlachoudis, V. (2014). The FLUKA Code: Developments and Challenges for High Energy and Medical Applications. *Nuclear Data Sheets*, 120, 211–214. <https://doi.org/10.1016/j.nds.2014.07.049>
- Borca, V. C., Pasquino, M., Russo, G., Grosso, P., Cante, D., Sciacero, P., Girelli, G., Porta, M. R. L., & Tofani, S. (2013). Dosimetric characterization and use of GAFCHROMIC EBT3 film for IMRT dose verification. *Journal of Applied Clinical Medical Physics*, 14(2), 158–171. <https://doi.org/10.1120/jacmp.v14i2.4111>

- Burnham, K. P., & Anderson, D. R. (1998). Information Theory and Log-Likelihood Models: A Basis for Model Selection and Inference. In K. P. Burnham & D. R. Anderson (Eds.), *Model Selection and Inference: A Practical Information-Theoretic Approach* (pp. 32–74). Springer. https://doi.org/10.1007/978-1-4757-2917-7_2
- Cameron, A. C., & Trivedi, P. K. (Eds.). (2013a). Introduction. In *Regression Analysis of Count Data* (2nd ed., pp. 1–20). Cambridge University Press. <https://doi.org/10.1017/CBO9781139013567.004>
- Cameron, A. C., & Trivedi, P. K. (Eds.). (2013b). Model Specification and Estimation. In *Regression Analysis of Count Data* (2nd ed., pp. 21–68). Cambridge University Press. <https://doi.org/10.1017/CBO9781139013567.005>
- Cavazzuti, M. (2013). *Optimization Methods*. Springer Berlin Heidelberg. <https://doi.org/10.1007/978-3-642-31187-1>
- Centromere / biology / Britannica*. (2012, May 24). <https://www.britannica.com/science/centromere>
- Chadwick, K. H., & Leenhouts, H. P. (1973). A molecular theory of cell survival. *Physics in Medicine and Biology*, 18(1), 78–87. <https://doi.org/10.1088/0031-9155/18/1/007>
- Chen, P. (2011). Hessian Matrix vs. Gauss–Newton Hessian Matrix. *SIAM Journal on Numerical Analysis*, 49(4), 1417–1435. <https://doi.org/10.1137/100799988>
- Collinearity / statistics / Britannica*. (2013, December 24). <https://www.britannica.com/topic/collinearity-statistics>
- Cooper, G. M. (2000a). DNA Repair. *The Cell: A Molecular Approach*. 2nd Edition. <https://www.ncbi.nlm.nih.gov/books/NBK9900/>
- Cooper, G. M. (2000b). DNA Replication. *The Cell: A Molecular Approach*. 2nd Edition. <https://www.ncbi.nlm.nih.gov/books/NBK9940/>
- Denekamp, J., & Daşu, A. (1999). Inducible repair and the two forms of tumour hypoxia—Time for a paradigm shift. *Acta Oncologica (Stockholm, Sweden)*, 38(7), 903–918. <https://doi.org/10.1080/028418699432590>
- Devic, S., Seuntjens, J., Hegyi, G., Podgorsak, E. B., Soares, C. G., Kirov, A. S., Ali, I., Williamson, J. F., & Elizondo, A. (2004). Dosimetric properties of improved GafChromic films for seven different digitizers. *Medical Physics*, 31(9), 2392–2401. <https://doi.org/10.1118/1.1776691>
- Devic, S., Tomic, N., & Lewis, D. (2016). Reference radiochromic film dosimetry: Review of technical aspects. *Physica Medica*, 32(4), 541–556. <https://doi.org/10.1016/j.ejmp.2016.02.008>
- Epithelium / anatomy / Britannica*. (2009, April 1). <https://www.britannica.com/science/epithelium>
- Franken, N. A. P., Rodermond, H. M., Stap, J., Haveman, J., & van Bree, C. (2006). Clonogenic assay of cells in vitro. *Nature Protocols*, 1(5), 2315–2319. <https://doi.org/10.1038/nprot.2006.339>

- GafChromic. (n.d.). *1GafChromic®EBT2 and EBT3 Films for Ball Cube II Phantom*. Retrieved March 31, 2022, from <https://hobbydocbox.com/Photography/67018394-Gafchromic-ebt2-and-ebt3-films-for-ball-cube-ii-phantom.html>
- Galvin, J. M., Smith, A. R., & Lally, B. (1993). Characterization of a multileaf collimator system. *International Journal of Radiation Oncology*Biology*Physics*, 25(2), 181–192. [https://doi.org/10.1016/0360-3016\(93\)90339-W](https://doi.org/10.1016/0360-3016(93)90339-W)
- Gavin, H. P. (2020). *The Levenberg-Marquardt algorithm for nonlinear least squares curve-fitting problems*. 19.
- Ghasemi, Z., Tahmasebi-Birgani, M.-J., Ghafari Novin, A., Motlagh, P. E., Teimoori, A., Ghadiri, A., Pourghadamayari, H., Sarli, A., & Khanbabaei, H. (2020). Fractionated radiation promotes proliferation and radioresistance in bystander A549 cells but not in bystander HT29 cells. *Life Sciences*, 257, 118087. <https://doi.org/10.1016/j.lfs.2020.118087>
- Gholami, S., Nedaie, H. A., Longo, F., Ay, M. R., Wright, S., & Meigooni, A. S. (2016). Is grid therapy useful for all tumors and every grid block design? *Journal of Applied Clinical Medical Physics*, 17(2), 206–219. <https://doi.org/10.1120/jacmp.v17i2.6015>
- Gholizadeh Sendani, N., Karimian, A., Ferreira, C., & Alaei, P. (2018). Technical Note: Impact of region of interest size and location in Gafchromic film dosimetry. *Medical Physics*, 45(5), 2329–2336. <https://doi.org/10.1002/mp.12885>
- Ghosh, S., Ghosh, A., & Krishna, M. (2015). Role of ATM in bystander signaling between human monocytes and lung adenocarcinoma cells. *Mutation Research/Genetic Toxicology and Environmental Mutagenesis*, 794, 39–45. <https://doi.org/10.1016/j.mrgentox.2015.10.003>
- Gianfaldoni, S., Gianfaldoni, R., Wollina, U., Lotti, J., Tchernev, G., & Lotti, T. (2017). An Overview on Radiotherapy: From Its History to Its Current Applications in Dermatology. *Open Access Macedonian Journal of Medical Sciences*, 5(4), 521–525. <https://doi.org/10.3889/oamjms.2017.122>
- Giard, D. J., Aaronson, S. A., Todaro, G. J., Arnstein, P., Kersey, J. H., Dosik, H., & Parks, W. P. (1973). In vitro cultivation of human tumors: Establishment of cell lines derived from a series of solid tumors. *Journal of the National Cancer Institute*, 51(5), 1417–1423. <https://doi.org/10.1093/jnci/51.5.1417>
- Girard, F., Bouchard, H., & Lacroix, F. (2012). Reference dosimetry using radiochromic film. *Journal of Applied Clinical Medical Physics*, 13(6), 339–353. <https://doi.org/10.1120/jacmp.v13i6.3994>
- Giridhar, P., & Rath, G. K. (2020). Clinical Significance of Cell Survival Curves. In S. Mallick, G. K. Rath, & R. Benson (Eds.), *Practical Radiation Oncology* (pp. 171–175). Springer. https://doi.org/10.1007/978-981-15-0073-2_27
- Goel, A. (2021, September 19). *Filament circuit / Radiology Reference Article / Radiopaedia.org*. Radiopaedia. <https://doi.org/10.53347/rID-29738>

- Grass, G. D., Krishna, N., & Kim, S. (2016). The immune mechanisms of abscopal effect in radiation therapy. *Current Problems in Cancer*, 40(1), 10–24.
<https://doi.org/10.1016/j.currproblcancer.2015.10.003>
- Grieken, R. van, & Markowicz, A. (1993). *Handbook of X-ray spectrometry: Methods and techniques*. Marcel Dekker.
- Griliches, Z., & Ringstad, V. (1970). Error-in-the-Variables Bias in Nonlinear Contexts. *Econometrica*, 38(2), 368–370. <https://doi.org/10.2307/1913020>
- Grote, S. J., & Revell, S. H. (1972). CORRELATION OF CHROMOSOME DAMAGE AND COLONY-FORMING ABILITY IN SYRIAN HAMSTER CELLS IN CULTURE IRRADIATED IN G. *Curr. Top. Radiat. Res. Quart.* 7: No. 3, 303-9(Jun 1972).
<https://www.osti.gov/biblio/4599614>
- Guido van Rossum & and the Python development team. (2020). *Python Tutorial Release 3.8.1*
Guido van Rossum and the Python development team.
- Hall, E. J., & Giaccia, A. J. (2012). *Radiobiology for the radiologist* (7th ed). Wolters Kluwer Lippincott Williams & Wilkins.
- Han, D. (2013). *Comparison of Commonly Used Image Interpolation Methods*. 1556–1559.
<https://doi.org/10.2991/iccsee.2013.391>
- Haralick, R. M., Shanmugam, K., & Dinstein, I. (1973). Textural Features for Image Classification. *IEEE Transactions on Systems, Man, and Cybernetics, SMC-3*(6), 610–621. <https://doi.org/10.1109/TSMC.1973.4309314>
- Harding, S. M., Benci, J. L., Irianto, J., Discher, D. E., Minn, A. J., & Greenberg, R. A. (2017). Mitotic progression following DNA damage enables pattern recognition within micronuclei. *Nature*, 548(7668), 466–470. <https://doi.org/10.1038/nature23470>
- Heales, J. C., Harrett, A., & Blake, S. (1998). Timer error and beam quality variation during “ramp-up” of a superficial X-ray therapy unit. *The British Journal of Radiology*, 71(852), 1306–1309. <https://doi.org/10.1259/bjr.71.852.10319006>
- Heiberger, R. M., & Holland, B. (2015). Introductory Inference. In R. M. Heiberger & B. Holland, *Statistical Analysis and Data Display* (pp. 123–165). Springer New York.
https://doi.org/10.1007/978-1-4939-2122-5_5
- High Accuracy Electrometers for Low Current/High Resistance Applications / Tektronix*. (n.d.). Retrieved March 28, 2022, from <https://www.tek.com/en/documents/brochure/high-accuracy-electrometers-low-current-high-resistance-applications>
- Hilde Solesvik Skeie. (2021). *The relative biological effectiveness of low energy protons for human lung carcinoma cells* [Master Thesis]. University of Oslo.
- Hu, W., Xu, S., Yao, B., Hong, M., Wu, X., Pei, H., Chang, L., Ding, N., Gao, X., Ye, C., Wang, J., Hei, T. K., & Zhou, G. (2014). MiR-663 inhibits radiation-induced bystander effects by targeting TGFB1 in a feedback mode. *RNA Biology*, 11(9), 1189–1198.
<https://doi.org/10.4161/rna.34345>
- Iyer, R., & Lehnert, B. E. (2002). Low dose, low-LET ionizing radiation-induced radioadaptation and associated early responses in unirradiated cells. *Mutation Research/Fundamental and*

- Molecular Mechanisms of Mutagenesis*, 503(1), 1–9. [https://doi.org/10.1016/S0027-5107\(02\)00068-4](https://doi.org/10.1016/S0027-5107(02)00068-4)
- Jabbari, K. (2011). Review of Fast Monte Carlo Codes for Dose Calculation in Radiation Therapy Treatment Planning. *Journal of Medical Signals and Sensors*, 1(1), 73–86.
- James, G., Witten, D., Hastie, T., & Tibshirani, R. (Eds.). (2013). *An introduction to statistical learning: With applications in R*. Springer.
- Jeffers, J. R., Parganas, E., Lee, Y., Yang, C., Wang, J., Brennan, J., MacLean, K. H., Han, J., Chittenden, T., Ihle, J. N., McKinnon, P. J., Cleveland, J. L., & Zambetti, G. P. (2003). Puma is an essential mediator of p53-dependent and -independent apoptotic pathways. *Cancer Cell*, 4(4), 321–328. [https://doi.org/10.1016/S1535-6108\(03\)00244-7](https://doi.org/10.1016/S1535-6108(03)00244-7)
- Jiang, R., Shen, H., & Piao, Y.-J. (2010). The morphometrical analysis on the ultrastructure of A549 cells. *Romanian Journal of Morphology and Embryology = Revue Roumaine De Morphologie Et Embryologie*, 51(4), 663–667.
- Jolliffe, I. T. (2002). *Principal component analysis* (2nd ed). Springer.
- Kanagavelu, S., Gupta, S., Wu, X., Philip, S., Wattenberg, M. M., Hodge, J. W., Couto, M. D., Chung, K. D., & Ahmed, M. M. (2014). In Vivo Effects of Lattice Radiation Therapy on Local and Distant Lung Cancer: Potential Role of Immunomodulation. *Radiation Research*, 182(2), 149–162. <https://doi.org/10.1667/RR3819.1>
- Kellerer, A. M., & Rossi, H. H. (1971). RBE and the primary mechanism of radiation action. *Radiation Research*, 47(1), 15–34.
- Khan, A. ul M., Mikut, R., & Reischl, M. (2016). A New Feedback-Based Method for Parameter Adaptation in Image Processing Routines. *PLOS ONE*, 11(10), e0165180. <https://doi.org/10.1371/journal.pone.0165180>
- Kirkup, L. (2012). *Data Analysis for Physical Scientists: Featuring Excel®* (2nd ed.). Cambridge University Press. <https://doi.org/10.1017/CBO9781139005258>
- Koturbash, I., Loree, J., Kutanzi, K., Koganow, C., Pogribny, I., & Kovalchuk, O. (2008). In Vivo Bystander Effect: Cranial X-Irradiation Leads to Elevated DNA Damage, Altered Cellular Proliferation and Apoptosis, and Increased p53 Levels in Shielded Spleen. *International Journal of Radiation Oncology*Biology*Physics*, 70(2), 554–562. <https://doi.org/10.1016/j.ijrobp.2007.09.039>
- Lewis, D., & Chan, M. F. (2015). Correcting lateral response artifacts from flatbed scanners for radiochromic film dosimetry. *Medical Physics*, 42(1), 416–429. <https://doi.org/10.1111/1.4903758>
- Liu, Z., Mothersill, C. E., McNeill, F. E., Lyng, F. M., Byun, S. H., Seymour, C. B., & Prestwich, W. V. (2006). A dose threshold for a medium transfer bystander effect for a human skin cell line. *Radiation Research*, 166(1 Pt 1), 19–23. <https://doi.org/10.1667/RR3580.1>
- Lloyd, S. (1982). Least squares quantization in PCM. *IEEE Transactions on Information Theory*, 28(2), 129–137. <https://doi.org/10.1109/TIT.1982.1056489>

- LPPool2d—PyTorch 1.11.0 documentation.* (n.d.). Retrieved April 28, 2022, from
<https://pytorch.org/docs/stable/generated/torch.nn.LPPool2d.html>
- Luce, A., Courtin, A., Levalois, C., Altmeyer-Morel, S., Romeo, P.-H., Chevillard, S., & Lebeau, J. (2009). Death receptor pathways mediate targeted and non-targeted effects of ionizing radiations in breast cancer cells. *Carcinogenesis*, 30(3), 432–439.
<https://doi.org/10.1093/carcin/bgp008>
- Mackonis, E. C., Suchowerska, N., Zhang, M., Ebert, M., McKenzie, D. R., & Jackson, M. (2007). Cellular response to modulated radiation fields. *Physics in Medicine and Biology*, 52(18), 5469–5482. <https://doi.org/10.1088/0031-9155/52/18/001>
- Magnus Børsting. (2020). *GRID irradiation and bystander effects in lung cancer cells* [MasterThesis, University of Oslo].
<https://www.duo.uio.no/bitstream/handle/10852/81244/1/Magnus-B-rsting---masteroppgave.pdf>
- Mandal Ananya. (2019, February 26). *What are Cytokines?* <https://www.news-medical.net/health/What-are-Cytokines.aspx>
- Mao, X., Boyd, L. K., Yáñez-Muñoz, R. J., Chaplin, T., Xue, L., Lin, D., Shan, L., Berney, D. M., Young, B. D., & Lu, Y.-J. (2011). Chromosome rearrangement associated inactivation of tumour suppressor genes in prostate cancer. *American Journal of Cancer Research*, 1(5), 604–617.
- Mao, Z., Bozzella, M., Seluanov, A., & Gorbunova, V. (2008). Comparison of nonhomologous end joining and homologous recombination in human cells. *DNA Repair*, 7(10), 1765–1771. <https://doi.org/10.1016/j.dnarep.2008.06.018>
- Mason, K. A., Losos, J. B., & Duncan, T. (2020). *Biology* (Twelfth edition). McGraw-Hill Education.
- Matson, S. W., Bean, D. W., & George, J. W. (1994). DNA helicases: Enzymes with essential roles in all aspects of DNA metabolism. *BioEssays: News and Reviews in Molecular, Cellular and Developmental Biology*, 16(1), 13–22.
<https://doi.org/10.1002/bies.950160103>
- McKinney, W. & others. (2010). Data structures for statistical computing in python. *Proceedings of the 9th Python in Science Conference*, 445, 51–56.
- McLaughlin, W. L., & Chalkley, L. (1965). Measurement of Radiation Dose Distributions with Photochromic Materials. *Radiology*, 84(1), 124–125. <https://doi.org/10.1148/84.1.124>
- McLaughlin, W. L., Puhl, J. M., Al-Sheikhly, M., Christou, C. A., Miller, A., Kovács, A., Wojnarovits, L., & Lewis, D. F. (1996). Novel Radiochromic Films for Clinical Dosimetry. *Radiation Protection Dosimetry*, 66(1–4), 263–268.
<https://doi.org/10.1093/oxfordjournals.rpd.a031731>
- McMahon, S. J. (2018). The linear quadratic model: Usage, interpretation and challenges. *Physics in Medicine & Biology*, 64(1), 01TR01. <https://doi.org/10.1088/1361-6560/aaf26a>

- Mean free path / physics / Britannica.* (2007, February 12).
<https://www.britannica.com/science/mean-free-path>
- Mesnil, M., Piccoli, C., Tiraby, G., Willecke, K., & Yamasaki, H. (1996). Bystander killing of cancer cells by herpes simplex virus thymidine kinase gene is mediated by connexins. *Proceedings of the National Academy of Sciences of the United States of America*, 93(5), 1831–1835.
- Micke, A., Lewis, D. F., & Yu, X. (2011). Multichannel film dosimetry with nonuniformity correction. *Medical Physics*, 38(5), 2523–2534. <https://doi.org/10.1118/1.3576105>
- Mitchel, R. E. J. (2004). The Bystander Effect: Recent Developments and Implications for Understanding the Dose Response. *Nonlinearity in Biology, Toxicology, Medicine*, 2(3), 173–183. <https://doi.org/10.1080/15401420490507512>
- Mohiuddin, M., Fujita, M., Regine, W. F., Meggooni, A. S., Ibbott, G. S., & Ahmed, M. M. (1999). High-dose spatially-fractionated radiation (GRID): A new paradigm in the management of advanced cancers. *International Journal of Radiation Oncology*Biology*Physics*, 45(3), 721–727. [https://doi.org/10.1016/S0360-3016\(99\)00170-4](https://doi.org/10.1016/S0360-3016(99)00170-4)
- Monomer / Definition & Facts / Britannica.* (2022, March 5).
<https://www.britannica.com/science/monomer>
- Morgenroth, K., & Ebsen, M. (2008). CHAPTER 8—Anatomy. In P. J. Papadakos, B. Lachmann, & L. Visser-Isles (Eds.), *Mechanical Ventilation* (pp. 69–85). W.B. Saunders. <https://doi.org/10.1016/B978-0-7216-0186-1.50012-0>
- Mothersill, C., & Seymour, C. (1997). Medium from irradiated human epithelial cells but not human fibroblasts reduces the clonogenic survival of unirradiated cells. *International Journal of Radiation Biology*, 71(4), 421–427. <https://doi.org/10.1080/095530097144030>
- Murphy, N. L., Philip, R., Wozniak, M., Lee, B. H., Donnelly, E. D., & Zhang, H. (2020). A simple dosimetric approach to spatially fractionated GRID radiation therapy using the multileaf collimator for treatment of breast cancers in the prone position. *Journal of Applied Clinical Medical Physics*, 21(11), 105–114. <https://doi.org/10.1002/acm2.13040>
- N. Reynaert et.al. (2006). *Monte Carlo Treatment Planning An Introduction* (No. 16). Netherlands Commission on Radiation Dosimetry.
- Nadrljanski, M. M. (2021a, June 7). *Anode (x-ray tube) / Radiology Reference Article / Radiopaedia.org.* Radiopaedia. <https://doi.org/10.53347/rID-8178>
- Nadrljanski, M. M. (2021b, September 18). *Cathode (x-ray tube) / Radiology Reference Article / Radiopaedia.org.* Radiopaedia. <https://doi.org/10.53347/rID-8180>
- Nagasawa, H., & Little, J. B. (1992). Induction of sister chromatid exchanges by extremely low doses of alpha-particles. *Cancer Research*, 52(22), 6394–6396.
- Najafi, M., Fardid, R., Hadadi, G., & Fardid, M. (2014). The Mechanisms of Radiation-Induced Bystander Effect. *Journal of Biomedical Physics & Engineering*, 4(4), 163–172.

- Nambiar, M., Kari, V., & Raghavan, S. C. (2008). Chromosomal translocations in cancer. *Biochimica et Biophysica Acta (BBA) - Reviews on Cancer*, 1786(2), 139–152. <https://doi.org/10.1016/j.bbcan.2008.07.005>
- Narayanan, P. K., Goodwin, E. H., & Lehnert, B. E. (1997). Alpha particles initiate biological production of superoxide anions and hydrogen peroxide in human cells. *Cancer Research*, 57(18), 3963–3971.
- Niclas Börlin. (2007, November 22). *Nonlinear Optimization Least Squares Problems—The Gauss-Newton method*.
- Niroomand-Rad, A., Blackwell, C. R., Coursey, B. M., Gall, K. P., Galvin, J. M., McLaughlin, W. L., Meigooni, A. S., Nath, R., Rodgers, J. E., & Soares, C. G. (1998). Radiochromic film dosimetry: Recommendations of AAPM Radiation Therapy Committee Task Group 55. *Medical Physics*, 25(11), 2093–2115. <https://doi.org/10.1118/1.598407>
- NIST: X-Ray Mass Attenuation Coefficients—Tungsten*. (n.d.). Retrieved June 28, 2022, from <https://physics.nist.gov/PhysRefData/XrayMassCoef/ElemTab/z74.html>
- Nomiya, T. (2013). Discussions on target theory: Past and present. *Journal of Radiation Research*, 54(6), 1161–1163. <https://doi.org/10.1093/jrr/rrt075>
- Nucleotide / biochemistry / Britannica*. (2008, July 17). <https://www.britannica.com/science/nucleotide>
- O'Connor-Cox, E., Mochaba, F. M., Lodolo, E., Majara, M., & Axcell, B. (1997). Methylene blue staining: Use at your own risk. *Master Brew Assoc Am Tech Q*, 34, 306–312.
- Paelinck, L., Neve, W. D., & Wagter, C. D. (2006). Precautions and strategies in using a commercial flatbed scanner for radiochromic film dosimetry. *Physics in Medicine and Biology*, 52(1), 231–242. <https://doi.org/10.1088/0031-9155/52/1/015>
- P.Andreo, A.E. Nahum, K.Hohlfeld, & H.Svensson. (1996). *Review of Data and Methods Recommended in the International Code of Practice, IAEA Technical Reports Series No. 277, Absorbed Dose Determination in Photon and Electron Beams*. INTERNATIONAL ATOMIC ENERGY AGENCY. <https://www.iaea.org/publications/5546/review-of-data-and-methods-recommended-in-the-international-code-of-practice-iaea-technical-reports-series-no-277-absorbed-dose-determination-in-photon-and-electron-beams>
- Panzacchi, S., Gnudi, F., Mandrioli, D., Montella, R., Strollo, V., Merrick, B. A., Belpoggi, F., & Tibaldi, E. (2019). Effects of short and long-term alcohol-based fixation on Sprague-Dawley rat tissue morphology, protein and nucleic acid preservation. *Acta Histochemica*, 121(6), 750–760. <https://doi.org/10.1016/j.acthis.2019.05.011>
- Pardee, A. B. (1974). A Restriction Point for Control of Normal Animal Cell Proliferation. *Proceedings of the National Academy of Sciences of the United States of America*, 71(4), 1286–1290.
- Park, S., Kang, S.-K., Cheong, K.-H., Hwang, T., Kim, H., Han, T., Lee, M.-Y., Kim, K., Bae, H., Su Kim, H., Han Kim, J., Jae Oh, S., & Suh, J.-S. (2012). Variations in dose distribution and optical properties of GafchromicTM EBT2 film according to scanning mode. *Medical Physics*, 39(5), 2524–2535. <https://doi.org/10.1118/1.3700731>

- Pedregosa, F., Varoquaux, G., Gramfort, A., Michel, V., Thirion, B., Grisel, O., Blondel, M., Prettenhofer, P., Weiss, R., Dubourg, V., Vanderplas, J., Passos, A., Cournapeau, D., Brucher, M., Perrot, M., & Duchesnay, E. (2011). Scikit-learn: Machine Learning in Python. *Journal of Machine Learning Research*, 12, 2825–2830.
- Peng, V., Suchowerska, N., Rogers, L., Claridge Mackonis, E., Oakes, S., & McKenzie, D. R. (2017). Grid therapy using high definition multileaf collimators: Realizing benefits of the bystander effect. *Acta Oncologica*, 56(8), 1048–1059.
<https://doi.org/10.1080/0284186X.2017.1299939>
- Perumean-Chaney, S. E., Morgan, C., McDowall, D., & Aban, I. (2013). Zero-inflated and overdispersed: What's one to do? *Journal of Statistical Computation and Simulation*, 83(9), 1671–1683. <https://doi.org/10.1080/00949655.2012.668550>
- Philip Mayes, Alan Nahum, & Jean-Claude Rosenwald. (2007). *Handbook of Radiotherapy Physics*. Taylor & Francis group.
- Photon Dose Distributions / Oncology Medical Physics*. (n.d.). Retrieved March 23, 2022, from <https://oncologymedicalphysics.com/photon-dose-distributions/>
- Podgorsak, E. B. (2016). *Radiation Physics for Medical Physicists*. Springer International Publishing. <https://doi.org/10.1007/978-3-319-25382-4>
- Preim, B., & Botha, C. (2014). Chapter 4—Image Analysis for Medical Visualization. In B. Preim & C. Botha (Eds.), *Visual Computing for Medicine (Second Edition)* (pp. 111–175). Morgan Kaufmann. <https://doi.org/10.1016/B978-0-12-415873-3.00004-3>
- Puck, T. T., & Marcus, P. I. (1956). Action of x-rays on mammalian cells. *The Journal of Experimental Medicine*, 103(5), 653–666. <https://doi.org/10.1084/jem.103.5.653>
- RADIATION BIOLOGY: A HANDBOOK FOR TEACHERS AND STUDENTS*. (2010). IAEA.
- Rahman, Md. A., Sultana, N., Ayman, U., Bhakta, S., Afrose, M., Afrin, M., & Haque, Z. (2022). Alcoholic fixation over formalin fixation: A new, safer option for morphologic and molecular analysis of tissues. *Saudi Journal of Biological Sciences*, 29(1), 175–182. <https://doi.org/10.1016/j.sjbs.2021.08.075>
- Recommendation ITU-R BT.601-7*. (2011). International telecommunication Union.
https://www.itu.int/dms_pubrec/itu-r/rec/bt/R-REC-BT.601-7-201103-I!!PDF-E.pdf
- Risk Factors: Age - NCI* (nciglobal,ncienterprise). (2015, April 29). [CgvArticle].
<https://www.cancer.gov/about-cancer/causes-prevention/risk/age>
- Samuel, T., Weber, H. O., & Funk, J. O. (2002). Linking DNA Damage to Cell Cycle Checkpoints. *Cell Cycle*, 1(3), 161–167. <https://doi.org/10.4161/cc.1.3.118>
- Sandy McDowell. (2019, January 25). *Understanding Cancer Death Rates*.
<https://www.cancer.org/latest-news/understanding-cancer-death-rates.html>
- Sari, B. G., Lúcio, A. D., Olivoto, T., Kryscun, D. K., Tischler, A. L., & Drebes, L. (2018). Interference of sample size on multicollinearity diagnosis in path analysis. *Pesquisa Agropecuária Brasileira*, 53, 769–773. <https://doi.org/10.1590/S0100-204X2018000600014>

- Saxena, A., Rathi, S. K., & Verma, A. S. (2011). *Continuous Slowing Down Approximation (CSDA) ranges of electrons for biomedical materials*. 4.
- Seabold, S., & Perktold, J. (2010). statsmodels: Econometric and statistical modeling with python. *9th Python in Science Conference*.
- Seuntjens, J. P., Strydom, W., & Shortt, K. R. (2005). Chapter 2 DOSIMETRIC PRINCIPLES, QUANTITIES AND UNITS. In *Radiation oncology physics: A handbook for teachers and students*. International Atomic Energy Agency.
- Shareef, M. M., Cui, N., Burikhanov, R., Gupta, S., Satishkumar, S., Shajahan, S., Mohiuddin, M., Rangnekar, V. M., & Ahmed, M. M. (2007). Role of Tumor Necrosis Factor- α and TRAIL in High-Dose Radiation-Induced Bystander Signaling in Lung Adenocarcinoma. *Cancer Research*, 67(24), 11811–11820. <https://doi.org/10.1158/0008-5472.CAN-07-0722>
- Shortt, K. R., Bielajew, A. F., Ross, C. K., Stewart, K. J., Burke, J. T., & Corsten, M. J. (2002). The effect of wall thickness on the response of a spherical ionization chamber. *Physics in Medicine and Biology*, 47(10), 1721–1731. <https://doi.org/10.1088/0031-9155/47/10/308>
- Silverman, B. W. (1998). *Density estimation for statistics and data analysis*. Chapman & Hall/CRC.
- Soleymanifard, S., & Bahreyni, M. T. T. (2012). Comparing the level of bystander effect in a couple of tumor and normal cell lines. *Journal of Medical Physics / Association of Medical Physicists of India*, 37(2), 102–106. <https://doi.org/10.4103/0971-6203.94745>
- Stevens, M. A., Turner, J. R., Hugtenburg, R. P., & Butler, P. H. (1996). High-resolution dosimetry using radiochromic film and a document scanner. *Physics in Medicine and Biology*, 41(11), 2357–2365. <https://doi.org/10.1088/0031-9155/41/11/008>
- Strang, G. (2006). *Linear algebra and its applications* (4th ed). Thomson, Brooks/Cole.
- Studzinski, G. P., & Danilenko, M. (2005). CHAPTER 92—Differentiation and the Cell Cycle. In D. Feldman (Ed.), *Vitamin D (Second Edition)* (pp. 1635–1661). Academic Press. <https://doi.org/10.1016/B978-012252687-9/50096-6>
- Suchowerska, N., Ebert, M. A., Zhang, M., & Jackson, M. (2005). In vitro response of tumour cells to non-uniform irradiation. *Physics in Medicine and Biology*, 50(13), 3041–3051. <https://doi.org/10.1088/0031-9155/50/13/005>
- Thermionic emission / physics / Britannica*. (2021, March 23). <https://www.britannica.com/science/thermionic-emission>
- Thevenaz, P., Ruttimann, U. E., & Unser, M. (1998). A pyramid approach to subpixel registration based on intensity. *IEEE Transactions on Image Processing*, 7(1), 27–41. <https://doi.org/10.1109/83.650848>
- Thiese, M. S., Ronna, B., & Ott, U. (2016). P value interpretations and considerations. *Journal of Thoracic Disease*, 8(9), E928–E931. <https://doi.org/10.21037/jtd.2016.08.16>
- Trainor, C., Butterworth, K. T., McGarry, C. K., McMahon, S. J., O'Sullivan, J. M., Hounsell, A. R., & Prise, K. M. (2012). DNA Damage Responses following Exposure to Modulated

- Radiation Fields. *PLOS ONE*, 7(8), e43326.
<https://doi.org/10.1371/journal.pone.0043326>
- Transcription / Definition, Steps, & Biology / Britannica*. (2019, September 26).
<https://www.britannica.com/science/transcription-genetics>
- van Leeuwen, C. M., Oei, A. L., Crezee, J., Bel, A., Franken, N. A. P., Stalpers, L. J. A., & Kok, H. P. (2018). The alfa and beta of tumours: A review of parameters of the linear-quadratic model, derived from clinical radiotherapy studies. *Radiation Oncology*, 13(1), 96. <https://doi.org/10.1186/s13014-018-1040-z>
- Virtanen, P., Gommers, R., Oliphant, T. E., Haberland, M., Reddy, T., Cournapeau, D., Burovski, E., Peterson, P., Weckesser, W., Bright, J., van der Walt, S. J., Brett, M., Wilson, J., Millman, K. J., Mayorov, N., Nelson, A. R. J., Jones, E., Kern, R., Larson, E., ... SciPy 1.0 Contributors. (2020). SciPy 1.0: Fundamental Algorithms for Scientific Computing in Python. *Nature Methods*, 17, 261–272. <https://doi.org/10.1038/s41592-019-0686-2>
- Waldestrand, E., Hole, E. O., Sagstuen, E., & Malinen, E. (2010). The energy dependence of lithium formate and alanine EPR dosimeters for medium energy x rays. *Medical Physics*, 37(7Part1), 3569–3575. <https://doi.org/10.1118/1.3432567>
- Wang, J. Z., Huang, Z., Lo, S. S., Yuh, W. T. C., & Mayr, N. A. (2010). A generalized linear-quadratic model for radiosurgery, stereotactic body radiation therapy, and high-dose rate brachytherapy. *Science Translational Medicine*, 2(39), 39ra48.
<https://doi.org/10.1126/scitranslmed.3000864>
- Weinstein, I. B. (2002). Addiction to Oncogenes—The Achilles Heel of Cancer. *Science*, 297(5578), 63–64. <https://doi.org/10.1126/science.1073096>
- Weisstein, E. W. (n.d.). *Square Line Picking* [Text]. Wolfram Research, Inc. Retrieved May 25, 2022, from <https://mathworld.wolfram.com/>
- Wu, X., Ahmed, M. M., Wright, J., Gupta, S., & Pollack, A. (2010). On Modern Technical Approaches of Three-Dimensional High-Dose Lattice Radiotherapy (LRT). *Cureus*, 2(3). <https://doi.org/10.7759/cureus.9>
- Yan, L., Xu, Y., Chen, X., Xie, X., Liang, B., & Dai, J. (2019). A new homogeneity index definition for evaluation of radiotherapy plans. *Journal of Applied Clinical Medical Physics*, 20(11), 50–56. <https://doi.org/10.1002/acm2.12739>
- Yan, W., Khan, M. K., Wu, X., Simone, C. B., Fan, J., Gressen, E., Zhang, X., Limoli, C. L., Bahig, H., Tubin, S., & Mourad, W. F. (2019). Spatially fractionated radiation therapy: History, present and the future. *Clinical and Translational Radiation Oncology*, 20, 30–38. <https://doi.org/10.1016/j.ctro.2019.10.004>
- Yang, S., Xu, J., Shao, W., Geng, C., Li, J., Guo, F., Miao, H., Shen, W., Ye, T., Liu, Y., Xu, H., & Zhang, X. (2015). Radiation-Induced Bystander Effects in A549 Cells Exposed to 6 MV X-rays. *Cell Biochemistry and Biophysics*, 72(3), 877–882.
<https://doi.org/10.1007/s12013-015-0555-2>

- Yung, Y., Walker, J. L., Roberts, J. M., & Assoian, R. K. (2007). A Skp2 autoinduction loop and restriction point control. *The Journal of Cell Biology*, 178(5), 741–747.
<https://doi.org/10.1083/jcb.200703034>
- Zhang, D., Zhou, T., He, F., Rong, Y., Lee, S. H., Wu, S., & Zuo, L. (2016). Reactive oxygen species formation and bystander effects in gradient irradiation on human breast cancer cells. *Oncotarget*, 7(27), 41622–41636. <https://doi.org/10.18632/oncotarget.9517>

7 Appendix

7.1 Compton Scattering

Here we derive the photon energy scattered after interaction with a free electron at rest. We will use the four-momentum vector $\vec{P} = [p^0, p^1, p^2, p^3]$, which consist of a time component p^0 and three space components $[p^0, p^1, p^2, p^3] = \vec{p} = [p_x, p_y, p_z]$.

First, we use conservation of energy.

$$E = E'$$

$$E_\gamma + E_e = E'_\gamma + E'_e$$

The energy of the incident photon is $h\nu$. Because of the assumption of an electron at rest, we only have rest energy $m_e c^2$. The energy of the photon after the interaction is simply $h\nu'$, and the energy of the electron after the interaction is unknown. We end up with this equation

$$h\nu + m_e c^2 = h\nu' + E'_e \quad 7-1$$

Finding E'_e requires that we introduce conservation of momentum. We need to find the components of the four-momentum vector for the photon and the electron. We will use equation 7-1 as a basis for our calculations. For the incident photon, the time component become $p_\gamma^0 = \frac{E_\gamma}{c} = \frac{h\nu}{c}$. We only have momentum in the x-direction. Using the relation

$$E^2 = (pc)^2 + (m_0 c^2)^2, \quad 7-2$$

and the fact that the photon is massless, we get $p_\gamma^1 = \frac{E}{c} = \frac{h\nu}{c}$.

The electron at rest does not have momentum, but it does have rest energy. The time component become $p_e^0 = \frac{E_e}{c} = \frac{m_e c^2}{c} = m_e c$. Where m_e is the rest mass of the electron.

We use trigonometry to find the spatial components of the momentum for the electron and photon after the interaction. Combining all the results, we get four four-momentum vectors

$$\overrightarrow{P_\gamma} = \begin{bmatrix} h\nu \\ \frac{c}{c} \\ h\nu \\ 0 \end{bmatrix}, \overrightarrow{P'_\gamma} = \begin{bmatrix} h\nu' \\ \frac{c}{c} \\ \frac{h\nu'}{c} \cdot \cos\phi \\ \frac{h\nu'}{c} \cdot \sin\phi \end{bmatrix}, \overrightarrow{P_e} = \begin{bmatrix} m_e c \\ 0 \\ 0 \end{bmatrix}, \overrightarrow{P'_e} = \begin{bmatrix} \frac{E'_e}{c} \\ p'_e \cdot \cos\theta \\ p'_e \cdot \sin\theta \end{bmatrix}$$

With all the components in place, we use conservation of momentum.

$$P = P'$$

$$P_\gamma + P_e = P'_\gamma + P'_e$$

First, we separate the γ and e , then we square both sides of the equation. For simplicity, we remove the vector sign above our four-vectors. We get this equation

$$\mathbf{P}_\gamma^2 - 2\mathbf{P}_\gamma\mathbf{P}'_\gamma + \mathbf{P}'_\gamma^2 = \mathbf{P}_e^2 - 2\mathbf{P}_e\mathbf{P}'_e + \mathbf{P}'_e^2. \quad 7-4$$

The product of two four-vectors is $\mathbf{X} \cdot \mathbf{Y} = x_0 y^0 - (\vec{x} \cdot \vec{y})$, we see that \mathbf{P}_γ^2 becomes 0. And \mathbf{P}_e^2 becomes $m_e^2 c^2$.

We use the dot product to find $\mathbf{P}_\gamma\mathbf{P}'_\gamma$, $\mathbf{P}_e\mathbf{P}'_e$, \mathbf{P}'_γ^2 , and \mathbf{P}'_e^2 .

$$\begin{aligned} \mathbf{P}_\gamma\mathbf{P}'_\gamma &= p_\gamma^0 \cdot p'^0_\gamma - (p_\gamma^1 \cdot p'^1_\gamma + p_\gamma^2 \cdot p'^2_\gamma) \\ &= \frac{h\nu}{c} \cdot \frac{h\nu'}{c} - \frac{h\nu}{c} \cdot \frac{h\nu'}{c} \cos\phi + 0 \\ &= \frac{h\nu}{c} \frac{h\nu'}{c} (1 - \cos\phi) \end{aligned}$$

$$\begin{aligned} \mathbf{P}_e\mathbf{P}'_e &= p_e^0 \cdot p'^0_e - (p_e^1 \cdot p'^1_e + p_e^2 \cdot p'^2_e) \\ &= m_e c \cdot \frac{E'_e}{c} - (p'_e \cos\theta \cdot 0 + p_e \sin\theta \cdot 0) \\ &= m_e c \cdot \frac{E'_e}{c} \end{aligned}$$

$$\begin{aligned}
\mathbf{P}'^2 &= p'_\gamma^0 \cdot p'_\gamma^0 - (p'_\gamma^1 \cdot p'_\gamma^1 + p'_\gamma^2 \cdot p'_\gamma^2) \\
&= \left(\frac{hv'}{c}\right)^2 - \left(\frac{hv'}{c}\right)^2 (\cos^2 \phi + \sin^2 \phi) \\
&= 0 \\
\mathbf{P}'^2 &= \left(\frac{E'_e}{c}\right)^2 - (p'_e^2 \cos^2 \theta + p'_e^2 \sin^2 \theta) = \left(\frac{E'_e}{c}\right)^2 - p'_e^2
\end{aligned}$$

If we use equation 7-2, we can exchange $\left(\frac{E'_e}{c}\right)^2$ with $p'_e^2 + m_e^2 c^2$. We get

$$\mathbf{P}'^2 = m_e c^2.$$

Finally, we put all our calculations together and rewrite equation 7-4 to get

$$-2 \frac{hv}{c} \cdot \frac{hv}{c} (1 - \cos \phi) = -2m_e E'_e + 2m_e^2 c^2,$$

solving for E'_e we get

$$E'_e = \frac{hv hv'}{m_e c^2} (1 - \cos \phi) + m_e c^2$$

Inserting this expression into equation 7-1 and solving for photon energy after the interaction we get

$$\begin{aligned}
h\nu + m_e c^2 &= h\nu' + \frac{hv hv'}{m_e c^2} (1 - \cos \phi) + m_e c^2 & 7-5 \\
h\nu' &= \frac{h\nu}{1 + \frac{hv}{(m_e c^2)(1 - \cos \phi)}}
\end{aligned}$$

Which is the expression for the energy of the photon after the interaction, with scattering angle ϕ .

7.2 Mean free path

Here we derive the mean free path of a photon.

Assume that you have incoming photons hitting a slab of material with infinitesimal area dA and width dx (see Figure 7-1). The total probability of N photons hitting the slab, with an interaction probability of σ is

$$P = \frac{N\sigma}{dA} = n\sigma dx \quad 7-6$$

Where n is atoms per unit volume

$$n = \frac{N}{dV} = \frac{N}{dAdx} .$$

The probability of **not** interacting is $1 - P$, then number of photons after the slab $N(x + dx)$ becomes

$$N(x + dx) = N(x)(1 - P) = N(x) - N(x)P .$$

Rearranging and inserting our expression for P we get

$$N(x + dx) - N(x) = -N(x) n\sigma dx .$$

If we divide by dx and let dx approach 0, we get

$$\lim_{dx \rightarrow 0} \frac{N(x + dx) - N(x)}{dx} = \frac{dN}{dx} = -N(x) n\sigma dx .$$

Solving the differential equation, we get

$$N(x) = N_0 e^{-n\sigma x} \rightarrow \frac{N(x)}{N_0} = e^{-n\sigma x} = 1 - P = Q,$$

where N_0 is the number of photons entering the slab. Now we have the fraction of photons that doesn't interact in the slab. If we multiply Q with P , we get a binomial looking probability density function, which describes the probability of an interaction happening somewhere between x and dx

$$PQ = n\mu e^{-n\sigma x} dx.$$

Integrating over possible pathlength from 0 to ∞ we get an expected pathlength of

$$\langle x \rangle = \int_0^\infty x \cdot n\mu e^{-n\sigma x} dx .$$

Solving the integral using partial integration we get

$$\langle x \rangle = n\sigma \left[-\frac{x}{n\sigma} e^{-n\sigma x} - \frac{1}{(n\sigma)^2} e^{-n\sigma x} \Big|_0^\infty \right]$$

Using L'Hôpital's rule we see that

$$\lim_{x \rightarrow \infty} xe^{-n\sigma x} = 0 .$$

For the second term we get $1/(n\sigma)^2$. This results in a mean free path of

$$\langle x \rangle = \frac{1}{n\sigma}$$

We know that n is atoms per unit volume, and from 1.1.1 that σ has the unit cm^2 . Multiplying them, we get the attenuation coefficient μ , resulting in the expression

$$\langle x \rangle = \frac{1}{\mu}$$

7-7

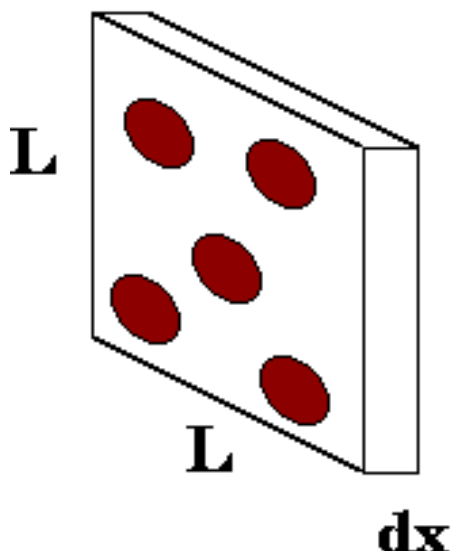


Figure 7-1. A thin slab of material with atoms that might interact with an incoming photon ("Mean Free Path," 2021)

7.3 Nearest Peak Code

```
d85 = np.max(dose_map)*0.85
isodose = ax.contour(y, x, dose_map, levels = [d85], colors = "blue")
lines = []
#getting coordinates from isodose lines
for line in isodose.collections[0].get_paths():
    if line.vertices.shape[0] > 500: #less than hundred points is not a dose
peak edge
        lines.append(line.vertices)
odd_i = 1
#looping over the center of each quadrat
for i in range(kernel_size//2, pooled_dose.shape[0]*kernel_size,
kernel_size):
    odd_j = 1
    for j in range(kernel_size//2,pooled_dose.shape[1]*kernel_size,
kernel_size):
        min_d = 1e6 #Large distance not possible to surpass
        #centre of the kernel
        centre = [i + kernel_size//2-kernel_size//2, j + kernel_size//2-
kernel_size//2] # [x-axis, y-axis]
        for line in lines: #getting information
            x = line[:,1] #as vertices is (column, row) we need to get index
1
            y = line[:,0]
            d = np.sqrt((x -centre[0])**2 + (y-centre[1])**2)
            tmp = np.min(d)
            if tmp < min_d:
                min_d = tmp
                idx_tmp = np.argwhere(d == min_d)
            #if the quadrat is located within a peak, then the distance is 0
            if dose_map[i,j] > d85: #assumes only 5 Gy irradiated films
                if kernel_size%2 == 0:
                    dist[i//kernel_size, j//kernel_size] = 0
                else:
                    dist[i - kernel_size//2*odd_i,j - kernel_size//2*odd_j] = 0
            else:
                if kernel_size % 2 == 0:
                    dist[i//kernel_size, j//kernel_size] = min_d
                else:
                    dist[i - kernel_size//2*odd_i,j - kernel_size//2*odd_j] = \
min_d
            odd_j += 2
    odd_i += 2
```

7.4 Reference conditions of FC65-G ionization chamber

KALIBRERINGSBEVIS

Calibration Certificate

2016/267-4



Statens strålevern
Norwegian Radiation Protection Authority

2. Informasjon om kalibreringen

2.1 Kalibreringstype

Kalibrering av ionisasjonskammer for størrelsen kerma i luft i enheten Gy i strålefelt fra en ^{60}Co -kilde. Kammer med volum 0,1 til 1 cm³ kan dekkes av denne kalibreringen.

Kalibreringen er utført i henhold til Technical Reports Series No. TRS-398, IAEA, 2000.

2.2 Kalibreringsbetingelser

2.2.1 Stråling

En ^{60}Co -kilde plassert i Gammabeam X200 gir gammastråling når den føres til en åpning med kollimator.

2.2.2 Klimatiske forhold

Temperatur:	19 °C til 22 °C
Lufttrykk:	97 kPa til 102 kPa
Luftfuktighet:	30 % til 80 %

2.2.3 Geometrisk forhold

Referansevilkår for 10 cm X 10 cm strålefelt:

Gammabeams kollimator definerte størrelsen til 10 cm X 10 cm i 1000 mm avstand fra fokus. Ionisasjonskammerets referansepunkt var på kammeraksen i senter av luftkaviteten. Kammeraksen ble plassert vertikalt på strålefeltaksen 1000 mm fra fokus, med referansepunktet midt i strålefeltet. Eventuelle merker på kammeret ble vendt mot kilden. Kammerets tilhørende build-up hette var på under kalibreringen.

2.2.4 Korreksjon av lekkasjestrom, rekombinasjon, polaritetseffekt og luftfuktighet

I_c korrigeres for lekkasjestrom.

I_c er ikke korrigert for rekombinasjonen som antas neglisjerbar, dvs. $k_{i,Q_0} = 1,000$.

Korreksjon for polaritetseffekt ved ^{60}Co er ikke utført.

Luftfuktigheten ved kalibrering kan variere innenfor 20 – 70 %. I_c er ikke korrigert for luftfuktighet.

7.5 X-ray dosimetry

Table 7-1. Output values recorded for an ionization chamber in nC from a calibration of the radiation field used to irradiate dosimetry films and A549 cells. Two calibrations were performed one for striped and dotted GRID, respectively. The chamber was irradiated in four positions and three or four repeated measurements were performed.

Ion chamber output [nC]		Stripes			
Position	A	B	C	D	
Exposure Times [s]					
5	[0.46,0.49,0.45]	[0.45,0.47,0.39]	[0.48,0.46,0.4]	[0.41,0.37,0.41]	
10	[1.52,1.56,1.45]	[1.4,1.39,1.32]	[1.4,1.59,1.54]	[1.57,1.51,1.54]	
15	[2.5,2.38,2.47]	[2.46,2.42,2.44]	[2.61,2.48,2.57]	[2.5,2.6,2.53]	
20	[3.45,3.49,3.58]	[3.44,3.58,3.39]	[3.55,3.56,3.5]	[3.75,3.55,3.68]	
60	[11.74,11.89,11.71]	[11.71,11.62,11.78]	[12.14,12.06,12.08]	[12.26,12.21,12.13]	
Dots					
	A	B	C	D	
5	[0.47,0.52,0.44,0.5]	[0.37,0.38,0.41,0.4]	[0.55,0.4,0.39,0.36]	[0.44,0.38,0.45,0.35]	
10	[1.56,1.52,1.44,1.41]	[1.37,1.36,1.51,1.42]	[1.54,1.48,1.48,1.44]	[1.57,1.35,1.41,1.39]	
15	[2.62,2.39,2.55,2.48]	[2.45,2.35,2.48,2.4]	[2.43,2.54,2.56,2.55]	[2.48,2.48,2.56,2.54]	
20	[3.47,3.56,3.6,3.55]	[3.52,3.49,3.54,3.53]	[3.6,3.55,3.62,3.51]	[3.53,3.55,3.53,3.6]	
60	[11.75,11.69,11.79,1 1.82]	[11.74,11.7,11.62,11.73]	[12.1,11.98,12.03,12.02]	[12.11.96,12.03,11.99]	

Table 7-2. The outputs from an ionization chamber for 5, 10 15 and 20 s exposure times were converted to dose following equation 2-2. Exposure times were estimated for low doses (0.1 to 0.5 Gy) from a linear regression model fitted to the output values. For doses above 0.5 Gy 60 second measurements were performed to get a dose-rate, that was used to obtain exposure times.

Dose [Gy]	0.1	0.2	0.5	1	2	5	10
Exposure Time							
Stripes	13.1s ± 0.2	23.4s ± 0.4	54s ± 1	1 m 43 s ± 3 s	3 m 27 s ± 7 s	8 m 39 s ± 18 s	17 m 19 s ± 36 s
Dots	13.0s ± 0.2	23.1s ± 0.3	53.3s ± 0.7	1 m 40 s ± 2 s	3 m 21 s ± 5 s	8 m 22 s ± 15 s	16 m 45 s ± 28 s

7.5.1 Gafchromic™ film fitting

Table 7-3. A model relating netOD of irradiated calibration films was fitted for each separate color channel using non linear regression. The resulting fitting parameters are represented here. Because of a split response in film intensity each film was put into a high or low response category, before fitting each category separately.

Color channel	BLUE	GREEN	GREY
Fitting parameters			
a (high, low)	19 ± 2 37 ± 9	8.9 ± 0.2 11 ± 1	8.6 ± 0.3 10 ± 2
b (high, low)	87 ± 8 59 ± 51	40 ± 1 39 ± 6	67 ± 3 61 ± 10
n (high, low)	1.8 ± 0.1 1.8 ± 0.9	2.60 ± 0.06 2.4 ± 0.3	2.59 ± 0.06 2.3 ± 0.3

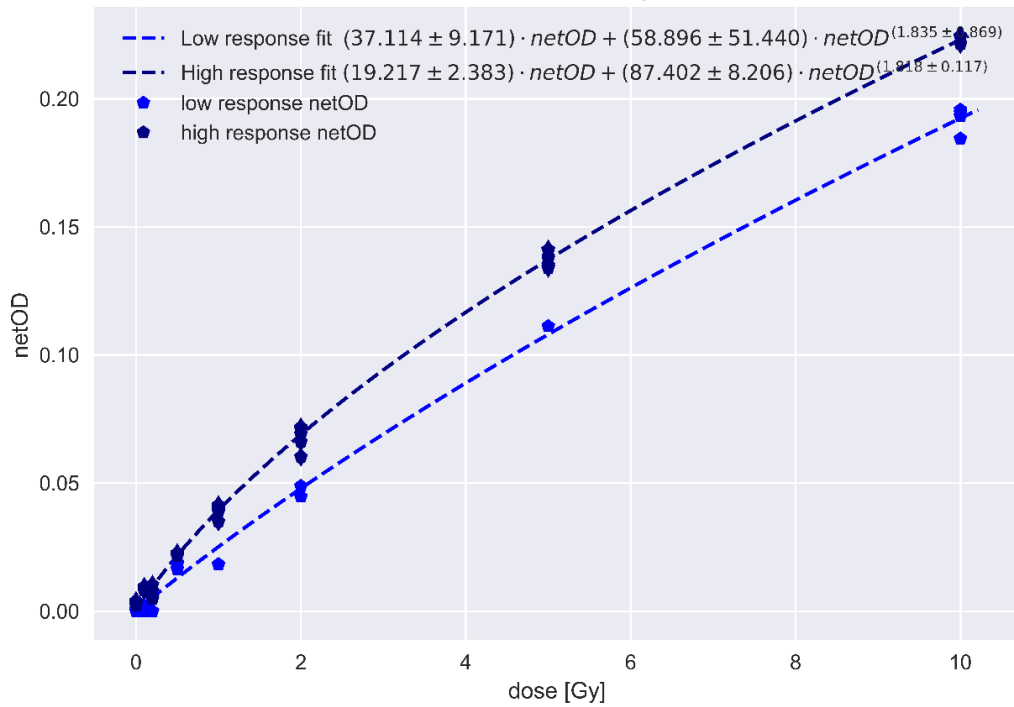


Figure 7-2. The resulting fit for high and low responding dosimetry films for BLUE channel netOD values. This fit was not used for further dosimetry.

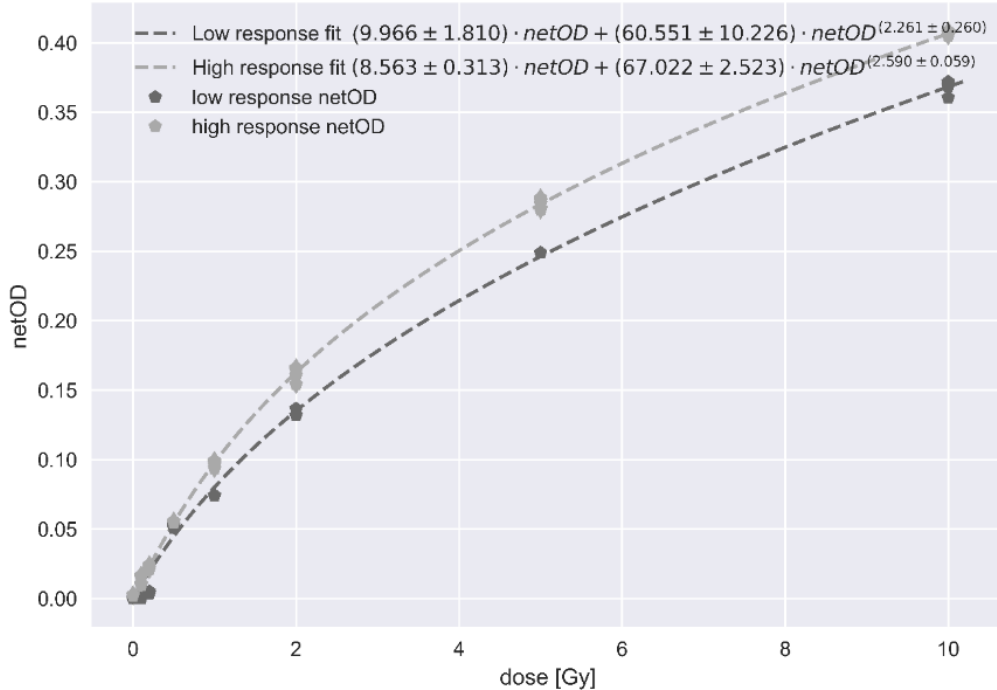


Figure 7-3. The resulting fit for high and low responding dosimetry films for GREY channel netOD values. This fit was not used for further dosimetry.

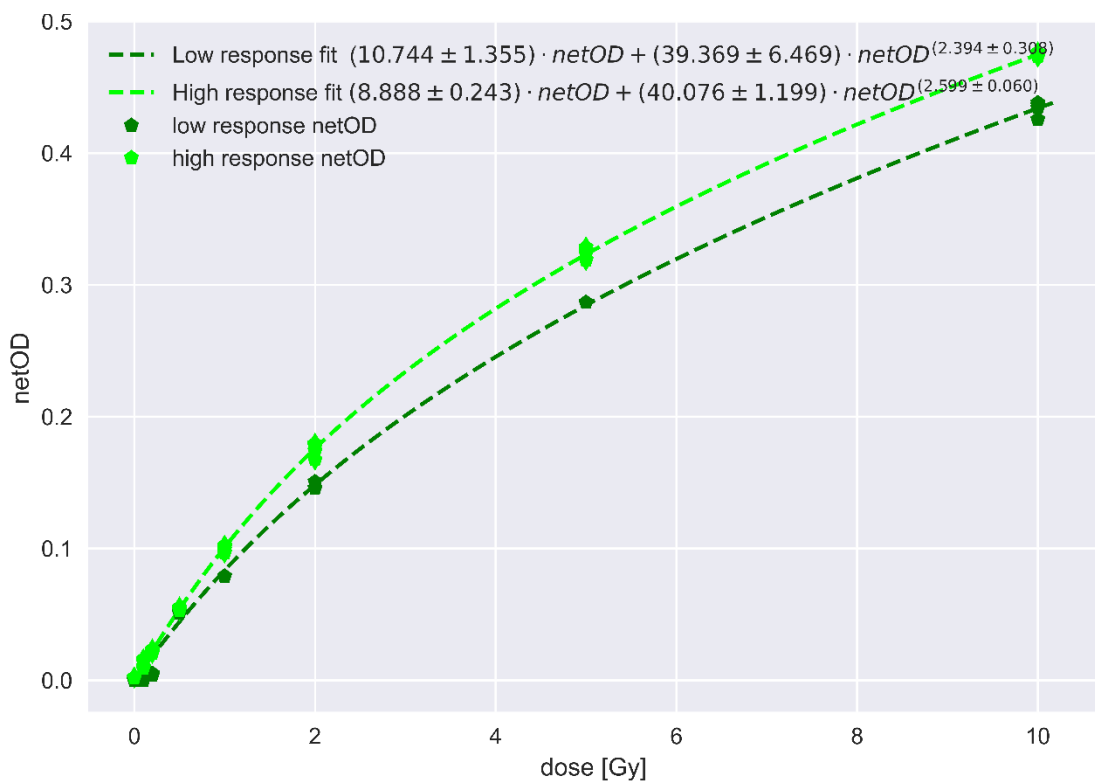


Figure 7-4. The resulting fit for high and low responding dosimetry films for the GREEN channel netOD values. This fit was not used for further dosimetry.

7.5.2 Random initialization of the nonlinear regression

Table 7-4. To test robustness of the nonlinear regression algorithm, that uses initial guesses of the estimated parameters to iteratively find the optimal parameters by randomly selecting a set of starting points from a standard normal distribution. The only criterium was that the initial guess of n was positive.

Initial guess of unknown parameters of the model $D = a \cdot netOD + b \cdot netOD^n$			Estimated parameters [a,b,n]	
a	b	n	Low response	High response
-2.505	-0.994	0.207	[7.238, 50.375, 2.625]	[6.205, 50.815, 2.954]
1.333	-1.283	0.711	[77223.095, -77194.254, 1.0]	[100403.926, -100379.48, 1.0]
-0.39	-1.349	1.001	[7.238, 50.375, 2.625]	[6.205, 50.815, 2.954]
0.176	0.17	0.715	[7.238, 50.375, 2.625]	[6.205, 50.815, 2.954]
-0.3	-0.358	0.114	[7.238, 50.374, 2.625]	[6.205, 50.815, 2.954]
-0.551	-0.035	0.535	[7.238, 50.375, 2.625]	[6.205, 50.815, 2.954]
1.387	-1.142	0.445	[7.238, 50.375, 2.625]	[6.205, 50.815, 2.954]
-0.328	-0.096	0.88	[7.238, 50.374, 2.625]	[6.205, 50.815, 2.954]

-0.428	0.308	0.468	[7.238, 50.375, 2.625]	[6.205, 50.815, 2.954]
-1.604	-1.323	0.271	[7.238, 50.374, 2.625]	[6.205, 50.815, 2.954]

7.6 Cell Segmentation

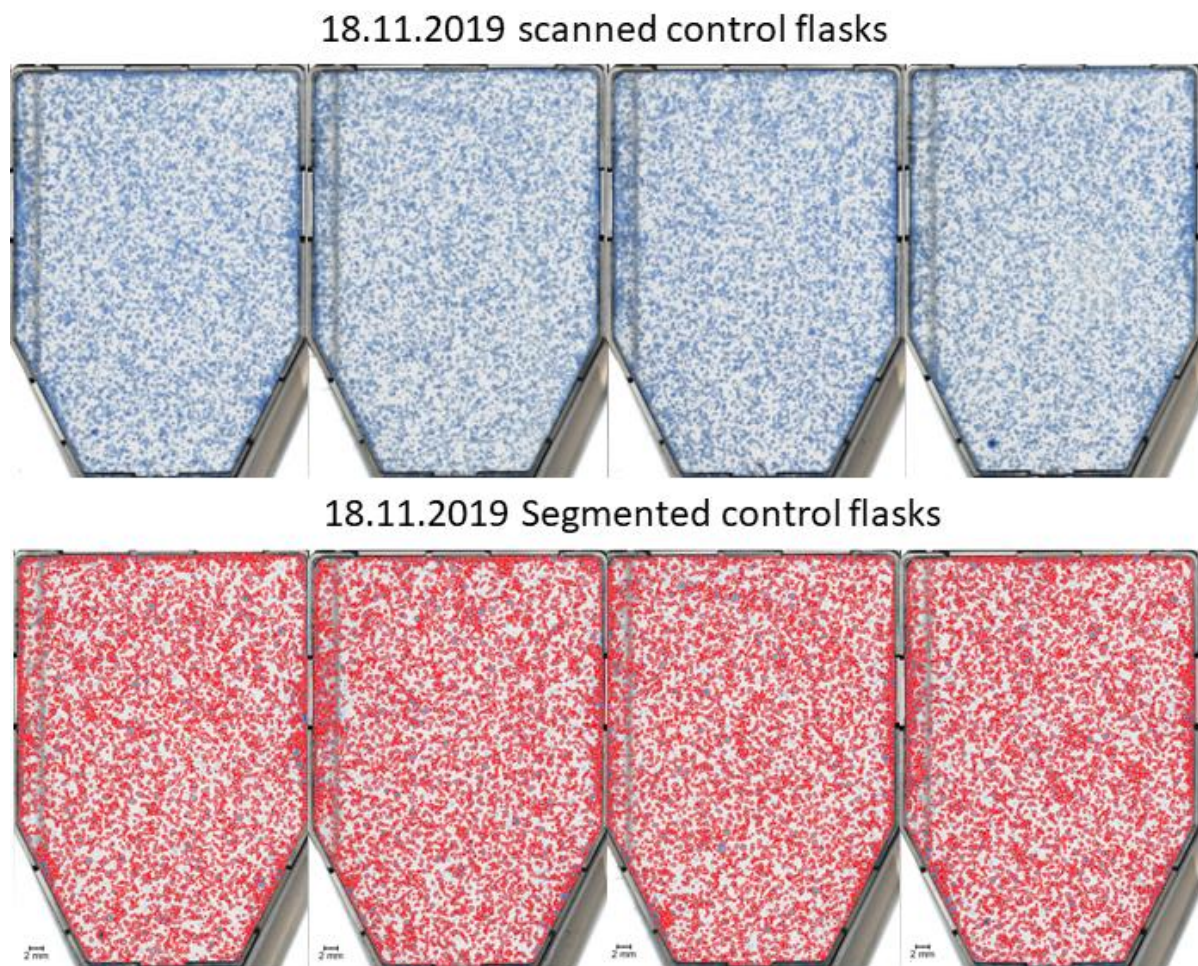


Figure 7-5. Stained control flasks (top) and segmented control flask (bottom). The flasks were analyzed to qualitatively evaluate the performance of the segmentation algorithm.

7.7 Cell flask registration

Dose map registered to segmented cell flasks for 2, 5 og 10 Gy stripes and dots with quadrat size of 0.5 (top) and 4 (bottom) mm.

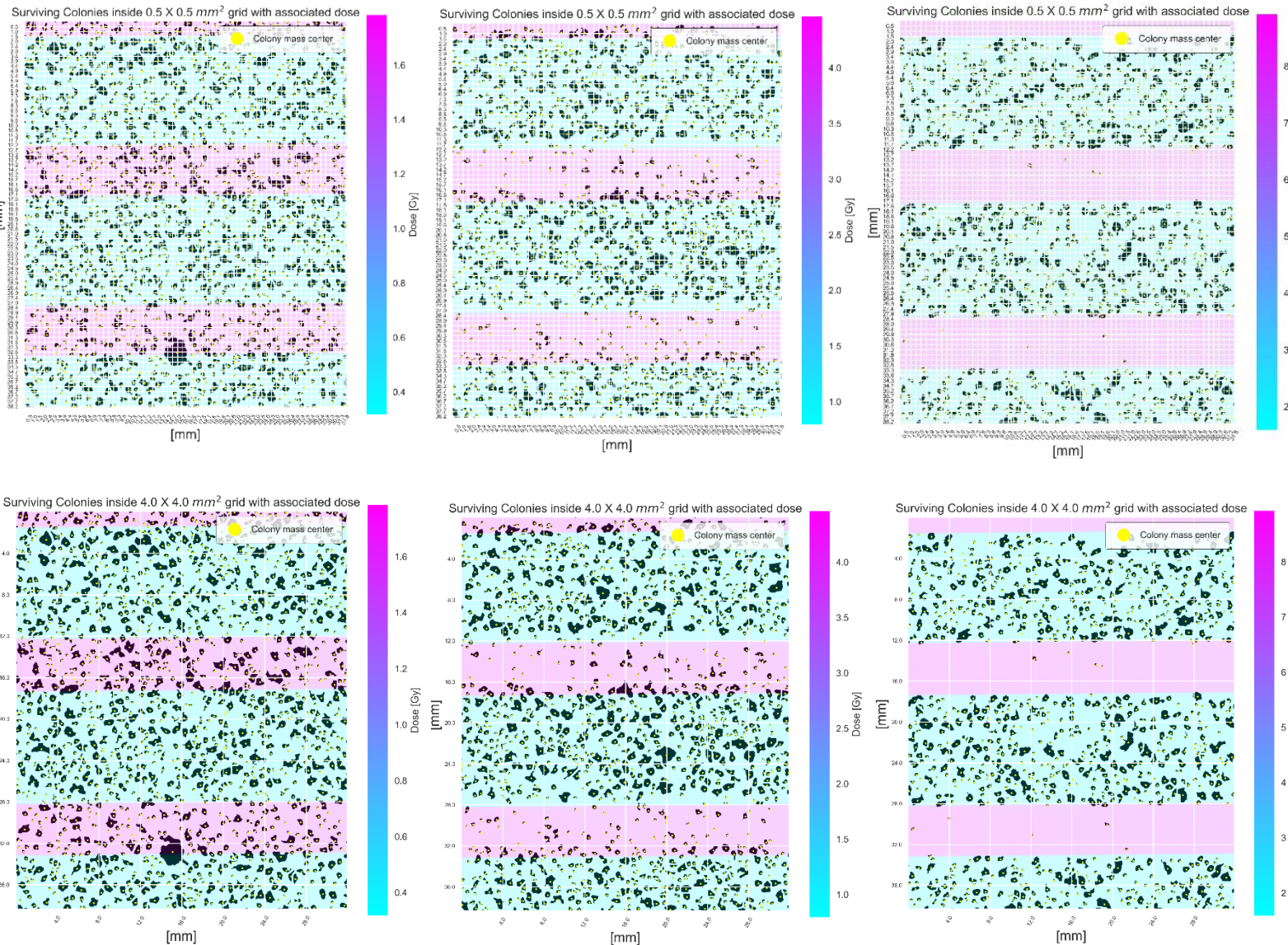


Figure 7-6. Colony maps generated from scanned and segmented cell flasks irradiated using a dotted GRID configuration and registered to their respective dose map. These colony maps were used in 2D survival analysis by dividing them into quadrats. Here we see an example of $0.5 \times 0.5 \text{ mm}^2$ (upper row) and $4 \times 4 \text{ mm}^2$ (lower row) quadrats with increasing dose to the right (2, 5, 10 Gy).

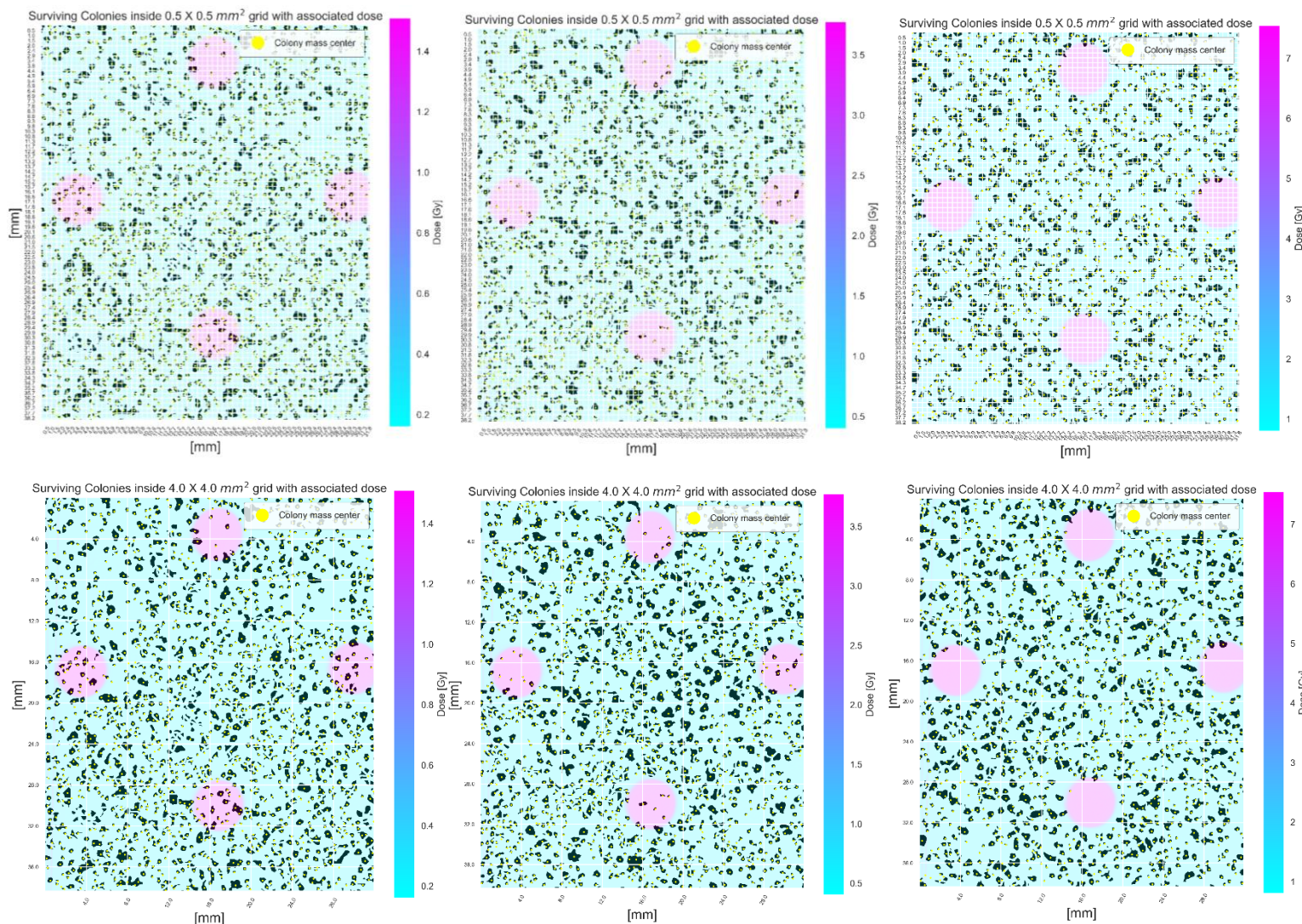
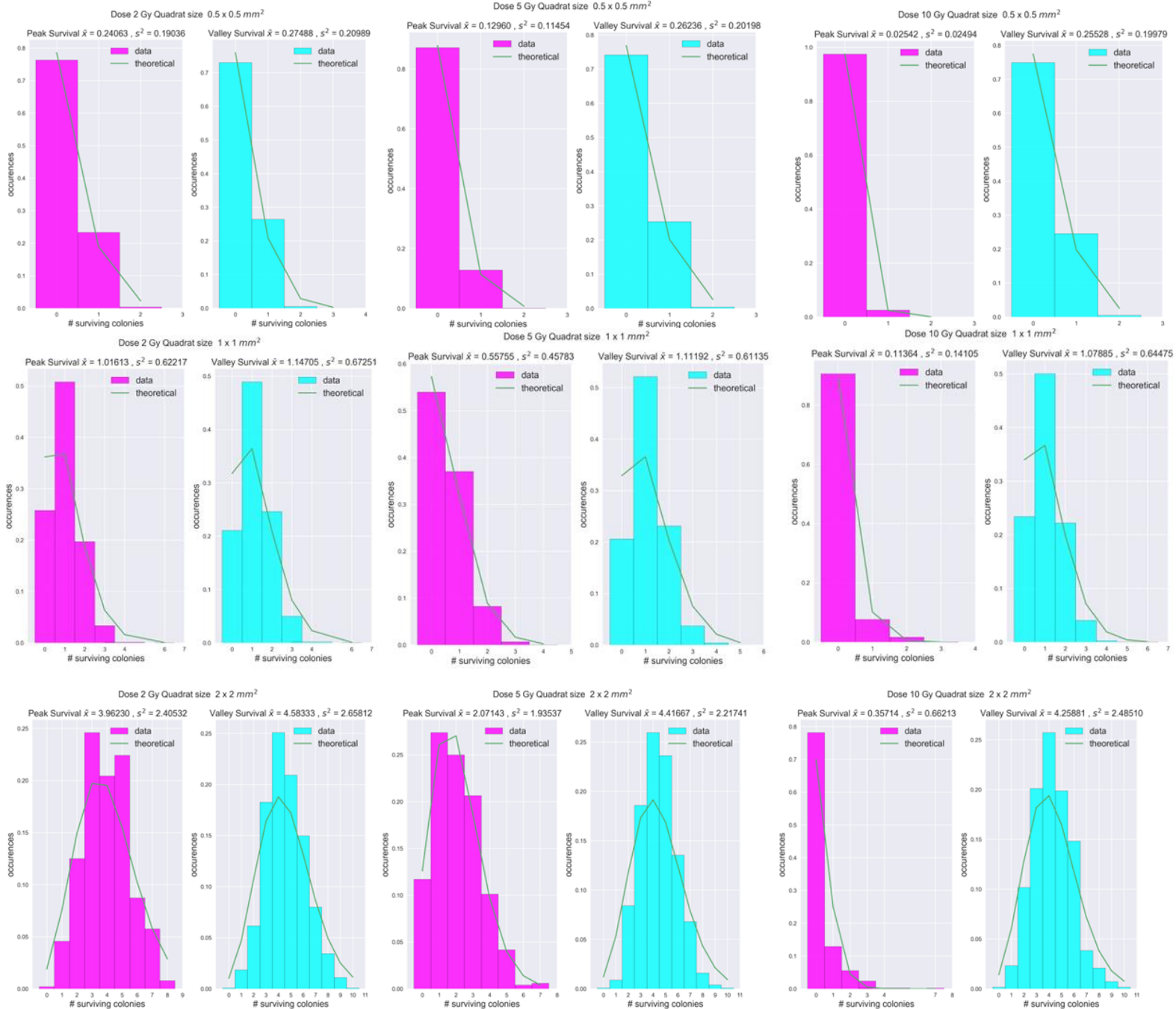
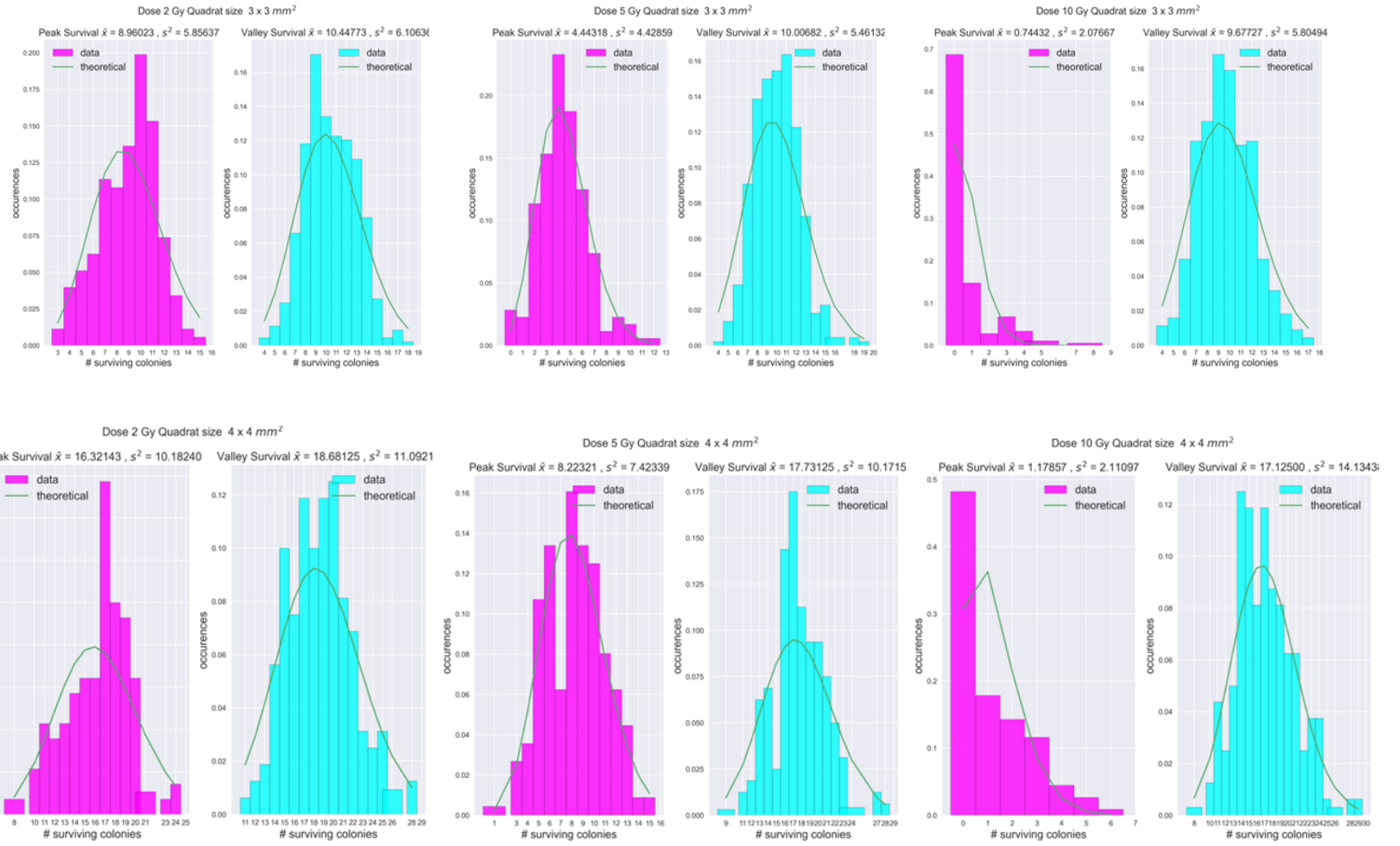


Figure 7-7. Colony maps generated from scanned and segmented cell flasks irradiated using a dotted GRID configuration and registered to their respective dose map. These colony maps were used in 2D survival analysis by dividing them into quadrats. Here we see an example of $0.5 \times 0.5 \text{ mm}^2$ (upper row) and $4 \times 4 \text{ mm}^2$ (lower row) quadrats with increasing dose to the right (2, 5, 10 Gy).

7.8 Poisson evaluation

Histograms generated from survival data of striped GRID irradiated cell flasks. Each datapoint is the number of colonies found within a quadrat put into peak (doses above 70% max) or valley (doses below 115% min). A theoretical distribution was generated from the mean of the observed data. Plots are arranged with increasing dose to the right and increasing quadrat size downward.





7.9 4 x 4 mm² 2D analysis results

2D analysis results for 4 x 4 mm² quadrat sizes.

Table 7-5., Poisson regression output for 4 x 4 mm² with increasing number of explanatory variables. The fitting parameters are const, x1, x2, x3 and x4. Const is the intercept, x1 and x2 is dose and dose squared, respectively. x3 is either peak distance or PAR when number of explanatory variables are 3. x4 is peak distance when all explanatory variables are included. The p-value of the coefficients show if there is a significant correlation between the explanatory variable and the independent variable. The p-value in the right column was calculated from the χ^2 output gathered from the regression result, indicating a goodness of fit between the observed data and the model.

Number of explanatory variables	Poisson regression output 4 x 4 mm ² quadrat size						χ^2 (p-value)
2	coef	std err	z	P> z	[0.025	0.975]	0.885
	const	2.9347	0.008	376.755	0.000	2.919	2.950
	x1	-0.0315	0.008	-3.754	0.000	-0.048	-0.015
	x2	-0.0264	0.002	-17.278	0.000	-0.029	-0.023
3 (peak dist)	coef	std err	z	P> z	[0.025	0.975]	0.982
	const	2.9295	0.009	315.360	0.000	2.911	2.948
	x1	-0.0263	0.008	-3.103	0.002	-0.043	-0.010
	x2	-0.0266	0.002	-17.313	0.000	-0.030	-0.024
	x3	0.0004	0.018	0.025	0.980	-0.035	0.036
3 (peak area)	coef	std err	z	P> z	[0.025	0.975]	0.990
	const	2.9282	0.008	373.434	0.000	2.913	2.944
	x1	-0.0750	0.011	-6.705	0.000	-0.097	-0.053
	x2	-0.0217	0.002	-12.348	0.000	-0.025	-0.018
	x3	0.1331	0.019	6.878	0.000	0.095	0.171
4	coef	std err	z	P> z	[0.025	0.975]	0.956
	const	2.9152	0.010	306.425	0.000	2.897	2.934
	x1	-0.0703	0.011	-6.275	0.000	-0.092	-0.048
	x2	-0.0223	0.002	-12.642	0.000	-0.026	-0.019
	x3	0.1355	0.020	6.679	0.000	0.096	0.175
	x4	0.0544	0.019	2.894	0.004	0.018	0.091



Figure 7-8. Observed survival vs survival predicted by a trained Poisson regression model for $4 \times 4 \text{ mm}^2$ quadrat size and 4 explanatory variables (D , D^2 , PAR and peak distance). All survival data were fed to the model, but we plotted each irradiation configuration separately. SC stands for surviving colonies.

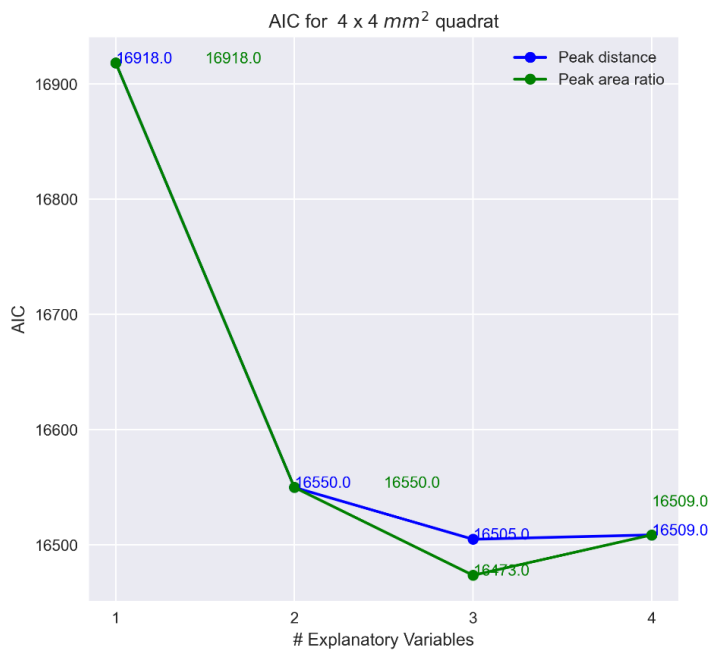


Figure 7-9. AIC score for increasing model complexity. The first and second explanatory variables were always dose and dose squared. The plot compares adding peak distance or PAR as the third explanatory variable to predict SC in the Poisson regression. When four variables were added to the model, we had both peak distance and PAR, and the score was therefore equal.

Table 7-6. Correlation matrix between the explanatory variables used in the Poisson regression. D represents dose

Explanatory variables	D	D^2	PAR	Peak Distance
D	1	0.94	0.60	-0.37
D^2	0.94	1	0.40	-0.32
PAR	0.60	0.40	1	-0.44
Peak Distance	-0.37	-0.32	-0.44	1

7.10 Average distance

The average distance between the 30 000 cells in the T25 cell flask (25 cm^2) was done using a result from the mathematical concept of square line picking (Weisstein, n.d.), which states that picking two points randomly placed inside a unit square the average distance between them will be 0.52. Assuming uniformly distributed cells, we have a cell density of 12 cells per mm^2 . We want to know, how large the square needs to be to have 2 cells within the square.

Solving the equation

$$12 \frac{\text{cells}}{\text{mm}^2} \cdot x = 2 \frac{\text{cells}}{\text{mm}^2}.$$

We get $x = \frac{1}{6}$. Which means that we need to reduce the $1 \times 1 \text{ mm}^2$ square by $1/6$, thus a square of size $\frac{1}{\sqrt{6}}$ is expected to contain 2 cells on average with an average distance between those points of

$$0.52 \cdot \frac{1}{\sqrt{6}} = 0.2123 \approx 0.2 \text{ mm}.$$